On the Effect of Nanofillers on the Environmental Stress Cracking Resistance of Glassy Polymers

----

von der Fakultät für Maschinenbau und Verfahrenstechnik

der Technischen Universität Kaiserslautern

genehmigte Dissertation

zur Erlangung des Grades

Doktor-Ingenieur

vorgelegt von:

M.Eng. Jiraporn Nomai

Fachgutachter:

Professor Dr.-Ing. Alois K. Schlarb

Professor Dr.-Ing. Volker Altstädt

Technische Universität Kaiserslautern - 2019

Acknowledgement

Kaiserslautern, May 2019   Jiraporn Nomai

Kurzfassung

Polycarbonat- (PC), Polystyrol- (PS) und Polymethylmethacrylat (PMMA)-Nanokomposite mit verschiedenen Partikelgehalten und –größen wurden auf einem Doppelschneckenextruder compoundiert und anschließend spritzgegossen. Die Zugabe einer geringen Menge von SiO_2-Nanopartikeln führte zu einer Verringerung der Transparenz, verbesserte jedoch die Zugeigenschaften, die Zähigkeit sowie die thermischen Eigenschaften der Werkstoffe. Dies war insbesondere bei Verwendung der kleinsten untersuchten Nanopartikel der Fall, welche nicht nur die mechanischen Eigenschaften der Nanokomposite verbesserten, sondern auch deren optische Qualität erhalten konnten. Interessanterweise führte die Zugabe der SiO_2-Nanopartikel zu einer erheblichen Steigerung der Spannungsrissbeständigkeit der Werkstoffe in sämtlichen untersuchten Medien, wobei der Effekt wiederum insbesondere bei den kleineren Nanopartikeln besonders ausgeprägt war. Die Steigerung der Spannungsrissbeständigkeit war in milden Medien und an der Luft besonders ausgeprägt, da die auftretenden Deformationsvorgänge durch die Anwesenheit der Nanopartikel stark verändert wurden. Ein Vergleich der verschiedenen Werkstoffe führte zu folgender Rangfolge hinsichtlich der Verbesserung der Spannungsrissbeständigkeit: $PMMA/SiO_2$ < PS/SiO_2 < niedermolekulares PC/SiO_2 < hochmolekulares PC/SiO_2. In den meisten Fällen zeigten die Nanokomposite mit 1 Vol.-% SiO_2-Nanopartikeln die größte Verbesserung der Spannungsrissbeständigkeit. Eine Korrelation des kritischen Spannungsintensitätsfaktors mit dem Hansen-Löslichkeitsparameter und dem Molvolumen des Mediums zeigt eine gute Übereinstimmung für verschiedene Flüssigkeiten und erlaubt somit eine Abschätzung des Spannungsrissrisikos in diversen Medien auch ohne aufwendige Versuche. Darüber hinaus wurden beschleunigte Spannungsrissversuche in aggressiven Medien und/oder bei erhöhter Temperatur sowie ein Superpositionsansatz für die Vorhersage langsamer Rissvorgänge entwickelt. Mit diesen Methoden können die Prüfzeiten und –kosten für Spannungsrissversuche deutlich reduziert werden. Zusätzlich kann durch geeignete Modellbildung und Simulation von Diffusionsprozessen in Verbindung mit einem bruchmechanischen Modell ein schnelles Werkstoffscreening erfolgen, welches dazu beiträgt, das Risiko spannungsrissbedingten Bauteilversagens zu vermindern.

Abstract

Polycarbonate (PC), polystyrene (PS) and poly(methyl methacrylate) (PMMA) nanocomposites containing different amounts and sizes of nano-SiO_2 particles were prepared using a twin-screw extruder followed by injection molding. Adding a small amount of nano-SiO_2 caused a reduction in material transparency but improved the tensile, toughness, and thermal properties of the polymer nanocomposites due to an adequate level of nano-SiO_2 particle distribution within the polymer matrix. This was particularly in the case with the smaller sized nano-SiO_2, which not only significantly improved mechanical properties but also preserved optical properties of the nanocomposites. Interestingly, the incorporation of nano-SiO_2 greatly enhanced the ESC resistance of the materials in all investigated fluids, particularly for smaller sizes nano-SiO_2. The enhancement in ESC resistance was more effective in mild agents and air, where the quality of the deformation process was vastly altered with the presence of nano-SiO_2. For a comparison of different materials, the ESC resistance improved in the following order: $PMMA/SiO_2$ < PS/SiO_2 < low molecular weight PC/SiO_2 < high molecular weight PC/SiO_2. In most cases, nanocomposites with 1 vol.% of nano-SiO_2 exhibited the largest improvement in ESC resistance. The correlation of the critical stress intensity factor with the Hansen solubility parameter and molar volume of the agent shows a very good agreement for different fluids, thus allowing to predict the risk of stress cracking in different fluids without performing extensive tests. Moreover, an accelerated ESC-testing in aggressive agent and/or elevated temperature as well as a modified superposition approach have been developed for predicting the slow crack growth behavior, allowing to minimize the test time and the great expense for stress-cracking tests. Additionally, the modeling and simulation of diffusion processes linked to the structural fracture model can be applied for quick screening and mitigating the risk of ESC failures in plastic products.

Table of Contents

List of Abbreviations and Symbols

Abbreviations

CNT	Carbon nanotube
CT	Compact tension
ESC	Environmental stress cracking
H	Haze
HNTs	Halloysite nanotubes
L	Light transmittance
LDPE	Low-density polyethylene
MMT	Montmorillonite
n-SiC	Nanosilicon carbide
PC	Polycarbonate
PE	Polyethylene
PET	Poly(ethylene terephthalate)
PLA	Poly(lactic acid)
PMMA	Poly(methyl methacrylate)
PP	Polypropylene
PS	Polystyrene
PSF	Polysulfone
PVC	Polyvinylchloride
PVP	Polyvinylpyrrolidone
SEM	Scanning electron microscope
SiO_2	Silicon dioxide
soln	Solution
S/V	Surface area to volume ratio

v/v %		Volume/volume percent
vol.%		Volume percent
WLF		Williams–Landel–Ferry
wt.%		Weight percent

Symbols

A	[mm^2]	Area
a	[mm]	Crack length
a_0	[mm]	Pre-crack length
A_c	[mm^2]	Surface area of cylindrical/platelet filler
A_s	[mm^2]	Surface area of spherical filler
A_{el}	[J]	Elastic energy component
A_{pl}	[J]	Plastic energy component
A_R	[J]	Crack propagation energy component
A_{tot}	[J]	Total deformation energy
a_T	[–]	Shift factor
$a(t)$	[mm]	Crack length as a function of time
C	[g/cm^3 or %]	Concentration of diffusing
C_p	[J/kg·K]	Specific heat capacity
D	[m^2/s]	Diffusion coefficient
da/dt	[mm/s]	Macro-crack propagation rate
E	[MPa]	Elastic modulus
E_a	[kJ/mol]	Activation energy
E_D	[J]	Dispersion interactions
E_H	[J]	Hydrogen-bonding interactions
E_P	[J]	Permanent dipole-permanent dipole interactions
F_{max}	[N]	Maximal force
G_c	[J/m^2]	Critical strain energy release rate

J	[g/cm^3·s]	Rate of mass transfer
k	[W/m·K]	Thermal conductivity
K_I	[MPam$^{1/2}$]	Stress intensity factor
K_{Ic}	[MPam$^{1/2}$]	Critical stress intensity factor
K_{Ith}	[MPam$^{1/2}$]	Threshold stress intensity factor
L	[m]	Length
M	[g]	Mass
M_w	[g/mol]	Molecular weight
MWD	[−]	Molecular weight distribution
q	[W/m^2]	Heat flux
r	[mm]	Radius
R	[J/K·mol]	Ideal gas constant
t	[mm]	Thickness
t	[s]	Time
T	[°C]	Temperature
T_g	[°C]	Glass transition temperature
T_{ref}	[°C]	Reference temperature
U_s	[J]	Elastic strain energy
U_γ	[J]	Surface energy
V	[cm^3/mol]	Molar volume
V_c	[mm^3]	Volume of cylindrical/platelet filler
v_f	[vol.%]	Volume fraction of filler
V_s	[mm^3]	Volume of spherical filler
W	[g]	Weight
w	[mm]	Width
Y	[-]	Geometry factor
θ	[°]	Contact angle

α	[m^2/s]	Thermal diffusivity
α	[mm/°C]	Coefficient of thermal expansion
ρ	[kg/m^3]	Density
β	[mm/%]	Coefficient of expansion due to liquid absorption
δ_a	[MPa$^{1/2}$]	Solubility parameters of the solvent/ESC agent
δ_D	[MPa$^{1/2}$]	Dispersion solubility parameter
δ_H	[MPa$^{1/2}$]	Hydrogen-bonding solubility parameter
δ_P	[MPa$^{1/2}$]	Polar solubility parameter
δ_p	[MPa$^{1/2}$]	Solubility parameters of the polymer
δ_{total}	[MPa$^{1/2}$]	Total solubility parameter
ε_{max}	[%]	Maximum strain
σ	[MPa]	Stress
σ_m	[MPa]	Maximum stress
σ_{ys}	[MPa]	Yield strength
ν	[−]	Poisson's ratio
γ_l	[mJ/m^2]	Surface free energy of a measuring liquid
γ_s	[mJ/m^2]	Surface free energy of a solid
γ_{sl}	[mJ/m^2]	Surface free energy of a solid-liquid interface
Φ	[−]	Incident light beam

1 Introduction

1.1 Background

Polymer nanocomposites have attracted increasing interest due to their superior properties and unique design possibilities [1,2]. Polymer nanocomposites are defined as multiphase materials containing a dispersion of nanofillers within the polymer matrix. Generally, nanofillers are in the order of nanometers at least in one dimension, and are classified into three types based on their geometry: one dimensional (1D rod-like), two dimensional (2D platelet-like) and three dimensional (3D spherical) materials [3,4]. Important factors for determining the reinforcing efficiency of nanofillers include their characteristics (e.g., size and geometry), their dispersion/distribution qualities, and their compatibility with the polymer matrix. An increase in the available surface area and degree of filler-matrix interactions ensures efficient stress transfer across the nanocomposite components. This situation ultimately contributes to an improvement in not only stiffness and strength but also in toughness of the material, which can enhance the function of desired materials for a wide range of applications.

However, there are several applications, in which contamination with a fluid/chemical agent is unavoidable during service (e.g., medical, automotive, and coating applications). Under the combined influence of an aggressive fluid (stress-cracking agent) and applied stress, polymeric-based materials may undergo a phenomenon known as environmental stress cracking (ESC). This phenomenon is responsible for the majority of lifetime shortening of plastic-based products and accounts for about 25–30% of all product failures in service [5–7]. Up to 90% of these failures occur in amorphous polymers, such as polyvinylchloride (PVC), polystyrene (PS), polymethylmethacrylate (PMMA), and polycarbonate (PC) [5,8]. Environmental stress cracking failure mechanisms in polymers involve a physical process via molecular interactions between the polymer and a stress-cracking agent. The stress-cracking agent diffuses slowly into the polymer structure under mechanical stress and interferes with the intermolecular forces bonding of the polymer chains. This phenomenon promotes macroscopic brittle-crack formation throughout the molecular disentanglement and accelerates premature brittle failure of polymeric materials during service [5,6]. The consequences of ESC failure can be an important issue for many applications and particular risk when the product is used for crucial applications, such as in medical care [7].

Environmental stress cracking behavior in polymers has attracted significant attention and has been intensively addressed for several years. However, very few studies have investigated the ESC behavior of polymer nanocomposites [6,8–13]. In fact, the incorporation of nanofillers into polymers can result in two opposing effects on ESC behavior. First, the enormous internal interfaces between the filler and the plastic matrix can support the absorption of the agent, thereby reducing the ESC resistance of the polymer. On the other side, nanoparticles can increase the length of crack propagation path and influence the new structural arrangements on the molecular scale, thereby promoting effective energy dissipation during the fracture process and even increasing ESC resistance. Therefore, it is of great interest to investigate whether the ESC resistance of a polymer can be improved via the incorporation of nanofillers. The ability to improve and predict the ESC behavior of polymeric materials in different fluid environments can enhance product performance and consequently reduce product failure during service.

1.2   Objective of the Study

The primary objectives of this work are:

- To investigate the effects of nano-SiO_2 content and size on the dispersion quality of the nanofiller as well as the optical, mechanical, and thermal properties of the amorphous polymer (PC, PS, PMMA)-based nanocomposites.

- To evaluate the effects of nanofiller content and size on the ESC behavior of polymer nanocomposites in different stress cracking agents using a fracture mechanical test method with optical crack detection.

- To investigate the effects of the intrinsic properties of polymers (e.g., molecular weight) and external environmental parameters (e.g., molecular size and solubility parameter of the agents, temperature) on the ESC behavior of polymer nanocomposites.

- To gain a deep understanding of the relation among the type of fluid, filler characteristics and stress cracking resistance, and finally to suggest a model for describing the dependence of ESC behavior based on these parameters.

- To propose a modified superposition approach to construct a master curve of crack propagation model from the short-term tests at different temperatures for reducing of testing times of long-duration ESC tests.

2 State of the Art

2.1 Polymer Nanocomposites

In polymer industries, polymer nanocomposites have become a dominant area of current research and development due to their remarkable enhancement of material performance for a wide range of applications [1,2]. Polymer nanocomposites are defined as multiphase materials containing a dispersion of nanofillers (at least one of the filler dimensions is in the nanometer range) within the polymer matrix [3]. As opposed to conventional composites, the higher surface area to volume ratio (S/V) of the nanofillers leads to a higher degree of potential interactions (i.e., van der Waals, hydrogen bonds, etc.) between the polymer and the nanofiller. This results in more efficient reinforcement and ultimately contributes to an improvement in the properties of the modified materials [4,14–17]. Generally, nanofillers can be classified into three categories based on their geometries; one dimensional (1D cylindrical), two dimensional (2D platelet) and three dimensional (3D spherical) materials (Figure 2.1) [3,4].

Figure 2.1: Types of nanofillers according to their geometries: (a) spherical, (b) rod-like, and (c) platelet-like nanofillers (adapted from reference [18]).

One of the most significant factors for determining the reinforcing efficiency of nanofillers is their characteristics (i.e., size and geometry) that are directly related to S/V and the quality of the filler-matrix interfacial region. Concerning the geometry effect, the total S/V of nanocomposites filled with spherical particles and cylindrical/platelet fillers are simply demonstrated in equation 2.1 and 2.2, respectively [14]:

Spherical filler system:

$$\frac{A_{s,total}}{V_{s,total}} = \frac{4\pi r^2 v_f}{\frac{4}{3}\pi r^3} = \frac{3v_f}{r} \tag{2.1}$$

where $A_{s,total}$ = Total surface area of spherical filler

$V_{s,total}$ = Total volume of spherical filler

r = Radius of particle size

v_f = Volume fraction of filler

Cylindrical/platelet fillers system:

$$\frac{A_c}{V_c} = \frac{2\pi r^2 + 2\pi r L}{\pi r^2 L} = \frac{2}{r} + \frac{2}{L} \qquad (2.2)$$

where $A_{c,total}$ = Total surface area of cylindrical/platelet filler

$V_{c,total}$ = Total volume of cylindrical/platelet filler

r = Radius of filler

L = Length of filler

v_f = Volume fraction of filler

At a constant filler volume, the total S/V of nanocomposites filled with spherical particles relative to cylindrical fillers can be scaled using equation 2.3:

$$\frac{S/V_s}{S/V_c} = \frac{3}{2(1 + \frac{r}{L})} \qquad (2.3)$$

This relationship indicates that the S/V of the platelet filler system ($r > L$) has the highest surface to volume ratio, thus providing the maximum reinforcing effect on the nanocomposite properties. In the case of cylindrical filler, the surface to volume ratio depends on the filler length. Short rods ($L < 2r$) have higher S/V than a spherical particle and vice versa. However, alignment of platelet and cylindrical fillers in the polymer matrix normally occurs during processing, making an anisotropic property in the nanocomposites that is the properties in the perpendicular direction to the applied force is significantly reduced [14,19]. This property of nanocomposites can be advantageous or disadvantageous, depending on the final applications.

In this work, attention is given to spherical particle-filled thermoplastics. As is clearly seen from equation 2.1, reducing the particle size leads to an increase of available surface area, which ensures high levels of interfacial interaction between the matrix and the nanofiller. The greater interactions at the interfacial area can control new structural arrangements of macromolecules and is responsible for more efficient stress transfer across the nanocomposite components [8,14]. This ultimately contributes to an improvement in the

desired properties, such as strength, stiffness, toughness, creep stability, and thermal properties of the modified materials [4,14–17].

Besides the characteristics of the nanoparticles, the quality of nanoparticles dispersion in the polymer matrix and their compatibility also plays a significant role in the reinforcement efficiency. In fact, most nanoparticles tend to agglomerate during processing because their large surface area creates a high potential attraction among particles. Therefore, the ultimate properties of the nanocomposite also primarily depend on the processing methods and conditions, which can effectively disperse the agglomeration of loosely combined coherent particles. Generally, three different ways of processing, *in situ* polymerization, solvent processing, and melt processing, are commonly used to obtain good nanoparticle dispersion quality.

In *in situ* polymerization, nanoparticles are dispersed in the monomer, which is then polymerized. The *in situ* polymerization method is particularly useful for preparing carbon nanotube (CNT) composites, which are normally difficult to make by melt processing due to their thermal instability. This technique also allows the grafting of polymer molecules onto tube walls, resulting in a high dispersion quality in several polymer matrices such as polyethylene (PE) [20,21], PMMA [22–24], PS [24], and polyvinylpyrrolidone (PVP) [23].

Solution mixing or solvent casting is another method of producing nanocomposites and is especially common in scientific research. In this method, a polymer is dissolved in an appropriate solvent. Then, nanoparticles are added to the lower viscosity polymer solution and are dispersed by ultrasonication or mechanical stirring, providing better dispersion of nanoparticles in the polymeric matrix [19]. However, the environmental impact of the removal of the organic solvent after casting must be considered.

The melt mixing method is one of the most economical and environmentally friendly methods and is the best choice for producing nanocomposites in the polymer industries. In this method, the agglomeration can be dispersed as the cohesive forces of the agglomerates are exceeded by the maximum separating forces induced by the polymer melt during processing [25,26]. Currently, a two-step melt compounding process has proved to be an effective and practical method for nanoparticle deagglomeration. In the two-step extrusion process, a masterbatch with high nanofiller content is first prepared and then diluted to the desired nanoparticle content using the same processing conditions. In fact, the degree of nanoparticle dispersion in melt compounding depends largely on

the matrix viscosity, mixing time, average shear rate, and average strain rate [26]. There-fore, applying the most suitable processing parameters is a key challenge to obtain high-performance materials for unique design opportunities.

2.1.1 Amorphous Polymer-based Nanocomposites

Thermoplastic-based nanocomposites have attracted great attention in both scientific research and industry, mainly due to their advantages in terms of cost-efficient manufac-turing processes, thermomechanical properties, environmental compatibility, and recy-clability [27,28]. Among the thermoplastic-based matrices used in the preparation of nanocomposites, amorphous polymers, such as PC, PMMA, and PS, have become attractive materials for large-scale industrial applications, due to their unique properties, including high strength, good flexibility, high glass transition temperature, excellent dimensional stability and optical transparency [29–31]. Therefore, most of the literature cited in the review deals with amorphous polymer-based nanocomposites.

As previously mentioned, if the nanofiller properties and the processing parameters are well chosen, polymer-based nanocomposites are potentially high-performance materials that exhibit superior property combinations. For example, Lee et al. [32] indicated that the addition of a small amount of nano-alumina to PC increased the tensile strength and hardness by approximately 51% and 85%, respectively. Moreover, they also pointed out that injection processing parameters such as injection pressure and holding pressure are effective parameters for adjusting the hardness and tensile strength of PC. Jing et al. [33] also proved that properties of PC nanocomposites are controlled by both the morphology and compatibility of the halloysite nanotubes (HNTs) with the PC matrix. Both N-(2-ami-noethyl)-3-aminopropyltrimethoxysilane (AEAPS) and n-octadecyltrimethoxysilane (OTMS) modified PC nanocomposites showed an improvement of compatibility between PC and HNTs. However, the OTMS modifier, which has longer alkyl tails, showed a stronger affinity for the PC matrix than the AEAPS modifier, and therefore significantly improved the thermal stability and mechanical properties of PC. In addition to improving the mechanical and thermal properties, Vahabi et al. [34] also reported that the incorpo-ration of polyhedral oligomeric silsesquioxane (POSS) and resorcinol bis(diphenyl phos-phate) (RDP) nanoparticles significant reduce the flammability of PC without affecting its transparency. The synergistic action of POSS and RDP was due to an appropriate filler dispersion quality. Greco et al. [28], also indicated an improvement in Young's modulus and dielectric properties of amorphous polyethylene terephthalate (PET) by the adding

different types of graphite nanoparticles including unmodified graphite, graphene nano-platelets and graphite intercalation compounds. The degree of nanofiller dispersion was particularly relevant for the dielectric properties of the nanocomposites, whereas no direct correlation existed with the mechanical properties. Moreover, a successful improvement in material properties by incorporating nanofiller was also found in PS and PMMA. Siengchin [35] proved that the stiffness, tensile strength, and creep stability of PS/alumina nanocomposites was significantly higher than that of microcomposites due to the better dispersion state of the nano-alumina particles in the PS matrix. Jang et al. [36] were able to prepare exfoliated and intercalated graphite oxide/PMMA nanocomposites. The enhancement of thermal, mechanical, and rheological properties indicate that graphite oxide efficiently reinforced the PMMA matrix. The effect of nanofiller content was investigated by Brostow et al. [37]. They indicated the incorporation of montmorillonite (MMT) to PMMA provided an increase in wear resistance at an appropriate nano-MMT content (1 wt%). Beyond the optimum point, a dramatic increase in wear was observed because of clay agglomeration and increased brittleness. Moreover, the influence of nanofiller geometries was also confirmed by Hasan et al. [38]; the glass transition temperature (T_g) and mechanical properties of PMMA nanocomposites are higher with reinforcement using alumina whiskers rather than spherical alumina nanoparticles due to the higher surface to volume ratio.

2.1.2 Amorphous Polymer/Silica (SiO_2) Nanocomposites

Among nanofillers used for reinforcing amorphous polymers, particular attention has been drawn by nano-silicon dioxide (SiO_2) due to its optical transparency and commercial availability with different surface treatments and porosity. Silica nanoparticle is an oxide of silicon that intrinsically contain hydroxyl groups ($-OH$) on their surface, which results in a greatly enhanced hydrophilic character [39]. These hydroxyl groups can also form a strong hydrogen bond among particles, leading to the temporary formation of a three-dimensional lattice structure that is very difficult to disperse [40], as shown in Figure 2.2. Therefore, surface treatments by organosilanes are normally applied to SiO_2 nanoparticles for minimizing their hydrophilic nature and improving their compatibility with the hydrophobic polymer matrix [39,41].

(a) Hydrophilic surface
(high interaction)

(b) Hydrophobic surface
(low interaction)
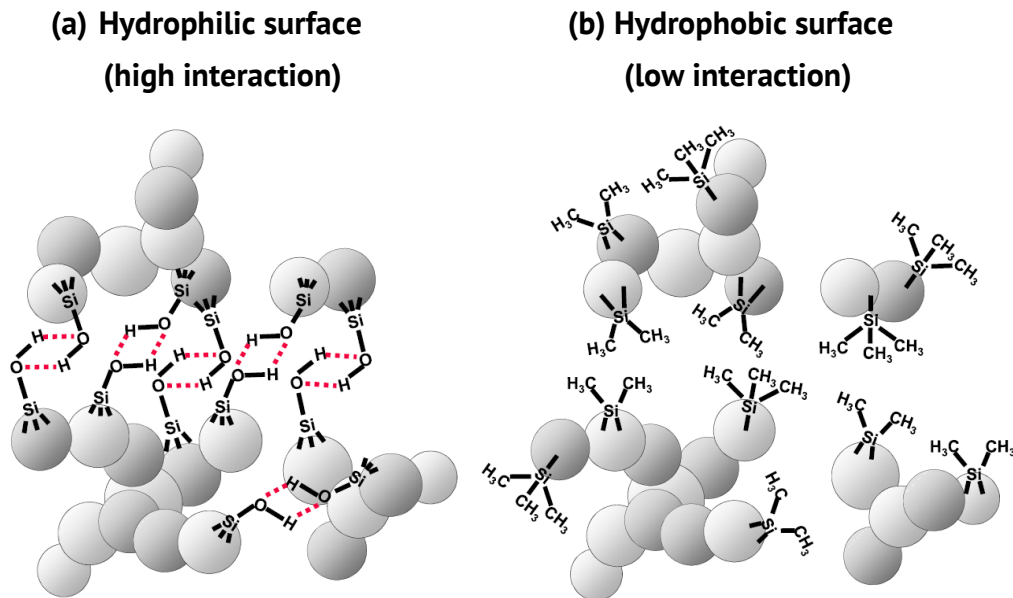
Figure 2.2: (a) schematic illustration of aggregate formation between hydrophilic silica nanoparticles and (b) surface treated silica nanoparticles (adapted from technical information of particle supplier, Evonik Industries AG, Germany).

Luyt et al. [41] confirmed that organically modified hydrophobic silica has better interfacial interaction with PC than hydrophilic silica, which results in significant improvements in scratch resistance, impact properties, and hardness due to more effective energy dissipation at the filler-matrix interface. Zhou et al. [42] also indicated that hydrophobic surface-modified nanosilica provided an enhancement in stiffness and fracture toughness for PC composites at low particle contents. However, transparency of the PC nanocomposites decreased with an increase in nanosilica content due to increasing light loss and thermal degradation of the PC matrix during the compounding process. Stojanoviʹc et al. [31] showed that well dispersed silica nanoparticles in PMMA matrix led to optimal particle-matrix bonding in nanocomposites and resulted in optimally improved mechanical and optical properties at 5 wt.% nanosilica particles. Eslami et al. [39] also reported the influence of nano-SiO_2 on the optical and mechanical properties of transparent acrylic based polyurethane for coating applications. They found that the adhesion strength of the coating was increased by the incorporation of nano-SiO_2 particles with respect to the nanocomposite transparency. Apart from mechanical and optical properties, Yadav et al. [30] indicated that the formation of interfacial interaction between nanosilica and PC matrix allowed an enhanced thermal stability, lowered interaction parameter as well as reduced free energy of mixing. Motaung et al. [1] also showed that the incorporation of nanosilica into PC, slightly increased the thermal stability of PC with increasing nanosilica

content up to 5 wt.%. Moreover, the improvement of thermal stability with the incorporation of nanosilica was also found in recycled PS [43]. This indicates that the degree of filler-matrix interaction also plays a significant role in the thermal properties of polymer nanocomposites. For amorphous polymers, an appropriate filler-matrix interaction tends to increase the glass transition temperature of the polymer resulting in an increase in the material usage temperature range [44,45].

Since a broad range of amorphous-based material properties can be attained by the incorporation of nanofiller, they have become attractive materials for large-scale industrial applications [1,30]. However, there are several applications where contamination with a fluid/chemical agent is unavoidable during service, such as medical, automotive, and coating products. Under the combined influence of an aggressive fluid (stress-cracking agent) and mechanical stress, polymeric-based materials may undergo a phenomenon known as environmental stress cracking (ESC), especially in amorphous based polymers. Therefore, the fundamental understanding and the improvement of the ESC resistance of polymeric materials is a great challenge in both academia and industry.

2.2 Environmental Stress Cracking of Polymers

Environmental stress cracking (ESC) is defined as the premature initiation of cracking and the embrittlement of plastic due to the simultaneous effects of mechanical stresses and aggressive fluids (known as stress cracking agents). In this case, the stress to failure of the plastic material is much lower than the normal failure limit [5,6,8,46]. Consequently, ESC is a serious threat in the plastic industry since it is the main cause of shortening the lifetime of plastic-based products during service. It is responsible for approximately 25–30% of all serious premature failures of plastic-based components, and almost 90% of these failures occur in amorphous (glassy) polymers [5].

2.2.1 Mechanisms of Environmental Stress Cracking

ESC failure mechanisms in polymers involve a physical process via molecular interactions between the polymer and a stress-cracking agent. Stress cracking agents do not cause any chemical degradation of the polymer but, instead, they diffuse slowly into the polymer interface under mechanical stress and cause additional hydrostatic pressure due to swelling. At this moment, a local lower density area is created, a so-called "craze", which is enclosed via highly drawn fibrils directed in the stress direction. In the craze area, a

high surface to volume ratio of fibrils favors diffusion of the stress-cracking agent into the polymer structure and interferes with the intermolecular forces bonding the polymer chains. This process accelerates the molecular disentanglement and leads to the break-down of the fibrils. Accordingly, a crack starts to propagate in the materials (see Figure 2.3) [5–8,46,47]. Finally, unexpected brittle failure of the polymeric material occurs during service. The consequences of ESC failures can be an important issue for many applications and is a particular risk when the product is used for crucial applications, such as in medical care [7].
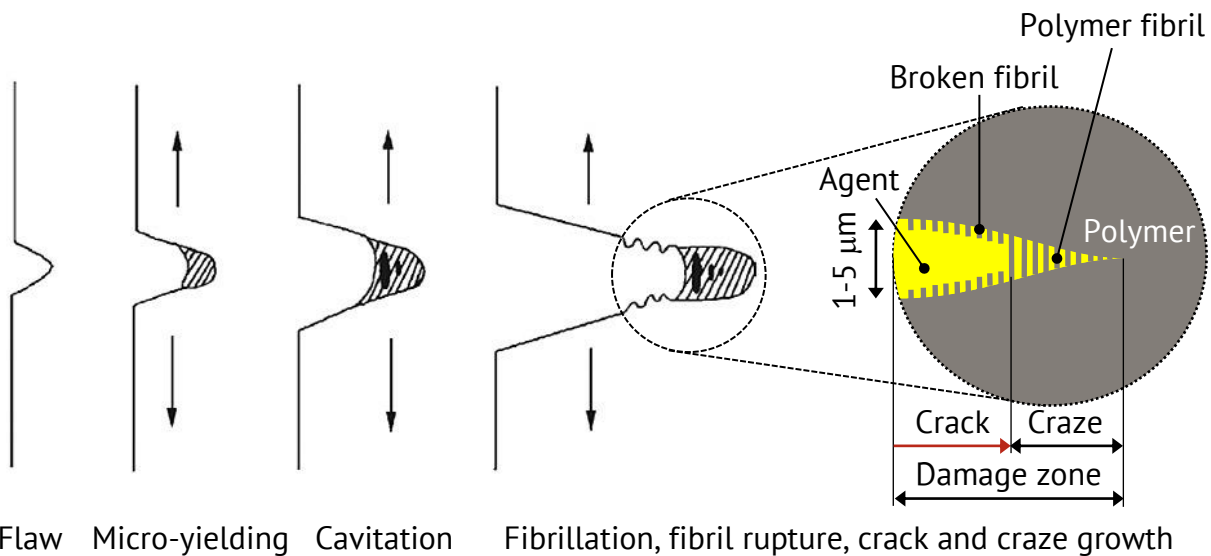
Figure 2.3: The mechanism of ESC in polymers (adapted from references [7,48]).

2.2.2 Factors Influencing Environmental Stress Cracking

In theory, ESC occurs in both amorphous polymers, such as PC, PMMA, PS, and PVC, and semi-crystalline polymers, such as PE [49], PET [46,50], polypropylene (PP). The degree of susceptibility to ESC is a function of their intrinsic properties, such as structure, molecular weight, molecular weight distribution, and degree of crystallinity. Additionally, external factors such as the physical and chemical properties of the stress cracking agent, ambient temperature, and type and rate of applied loading, have a noticeable influence on the ESC resistance of polymers as well. The main factors in both intrinsic and extrinsic parameters influencing ESC behavior of polymer are reviewed in detail in the following section.

2.2.2.1 Intrinsic Properties of Polymer

Polymer Structure

Amorphous polymers exhibit a higher tendency for ESC failure due to their lack of an ordered structure. The randomly entangled chains of amorphous polymer with no ordered structure facilitate fluid permeation into their molecular network and thus promotes premature ESC failure. In contrast, semi-crystalline polymers have a highly ordered molecular structure in the crystalline regions, which can retard the diffusion of the stress cracking agent and act as crack propagation barriers [49,50]. This contributes to a higher degree of ESC resistance. For example, Ramsteiner [51] indicated that syndiotactic crystalline PS shows a higher ESC resistance than atactic amorphous PS, as indicated by a much higher maximum tensile strength in methanol.

Aside from the polymer structure itself, a side chain structure also influences the ESC behavior of the materials. An increase of chain branching generally enhances the probability of tie molecule formation and thereby improves the ESC resistance. Han et al. [52] reported that the ESC resistance of long-chain branched PC was significantly enhanced compared with linear PC. The crack size and the crack number density significantly decreased with the introduction of a long-branched chain structure to PC. Yeh et al. [53] also studied the influence of branch length on the ESC properties of short-chain branch PE in Igepal solution. It is interesting to note that the ESC resistance and failure time of short-chain branch PE dramatically increased as the short-chain branch length increased from 2 to 4 and 6 carbon lengths. This was attributed to the increasing sliding resistance of the polymer chains through the crystal region and the entanglement in the amorphous region.

Molecular Weight and Molecular Weight Distribution

Generally, the average molecular weight (M_w) and the molecular weight distribution (*MWD*) have a noticeable impact on physical properties of a polymer product, including ESC resistance since it reflects the degree of polymer chain entanglements. The higher the molecular weight, the greater the amount of chain entanglements and, therefore, the higher the ESC resistance. A narrowing of the MWD enhances the ESC resistance of materials because of effective chain entanglements [5].

The effect of molecular parameters on the ESC resistance has studied in both semi-crystalline and amorphous polymers. Recently, Nomai et al. [54] stated that the molecular

weight plays an important role in the ESC behavior of polymers especially in an amorphous polymer such as PC. The ESC resistance of PC in isopropanol significantly increased with increasing molecular weight. Altstädt [5] showed an enhancement in ESC resistance for fatigue loading of PS with increasing molecular weight, both with and without an aggressive medium (sunflower oil). This enhancement was primarily due to an increase in craze stability and fibril density, resulting in greater resistance to liquid transport during the diffusion process. Moreover, he also indicated that a broadening of the *MWD* decreases the ESC resistance of PS because the low molecular weight fractions cannot build up an effective polymer chain entanglement for retarding the liquid diffusion process.

For semi-crystalline polymers, the higher molecular weight provided a higher average chain length and the proportion of tie molecules that hold the crystalline region. This interconnectivity can relieve the stress level in the interphase region and contribute to an increase of ESC resistance. Cheng et al. [49] confirmed that PE with a high number of chain entanglements shows greater ESC resistance. They also reported that phase interconnectivity in the crystalline region is an important factor in the ESC resistance of material. Chen et al. [55] also reported that inter-lamellar linkages due to physical chain entanglements lead to an increase in ESC resistance for PE. Similarly, Cazenave et al. [56] found that the excellent ESC resistance of PE were mainly due to the presence of longer chains which can effectively buildup tie chains.

Crystallinity

The improvement of ESC resistance of semi-crystalline polymers depends largely on the crystallite size, degree of crystallinity, and the binding strength of interconnectivity between the crystalline and amorphous phases. For example, Cheng et al. [49,57] found that the size of the crystalline domains was important for the ESC enhancement of PET. The crystals with larger lateral lamella areas result in a higher probability of interconnectivity linkage formation, contributing to a higher ESC resistance. Zhou et al. [50] confirmed that the ESC behavior of semi-crystalline PET depends on crystallinity levels. PET with higher degrees of crystallinity showed lower critical stress for cracking failures than their less crystalline counterparts, which led to a much shorter time to failure for the material. The amorphous phase, which occupied the interconnectivity region, became more progressively restricted with increasing crystallinity, resulting in the reduction of ESC resistance. Cazenave et al. [56] also observed that the ESC resistance of PE increased with decreasing degree of crystallinity in a material. As discussed above [49,55], a higher molecular weight also favors better ESC resistance in the semi-crystalline polymer due to increased chain

entanglements in the interconnectivity area. Aside from crystallinity, the level of side chain branching is also relevant to the ESC resistance of semi-crystalline polymers. Highly branched polymers have a higher density of tie-molecules and lower crystallinity, thus pointing to better ESC resistance of the materials [53].

2.2.2.2 External Environment Parameters

Stress Cracking Agents

As aforementioned, fluid diffusion plays an important role in the ESC behavior of polymers. Once the fluid has penetrated into the polymer structure, it becomes locally plasticized, promoting craze initiation and crack extension in the polymer. The more rapid the stress cracking agent absorption, the faster the macroscopic brittle-crack formation throughout the molecular disentanglement. Generally, the diffusion rate of liquid molecules into polymers depends largely on the molecular size and shape of the liquid and the degree of interaction between liquid and polymer, which can be quantified by the solubility parameters of the liquid relative to those of the polymers [58–60].

The solubility parameter defined by Hansen [60–62] can be divided into three types of cohesive forces that quantitatively describe the dispersion interactions (E_D), permanent dipole-permanent dipole (molecular) interactions (E_P), and hydrogen-bonding (molecular) interactions (E_H) as seen in equation 2.4:

$$E = E_D + E_P + E_H \qquad (2.4)$$

The Hansen cohesion energy (solubility) parameters of a fluid are obtained by dividing equation 2.4 by the molar volume (V), as described in equation 2.5 and 2.6:

$$\frac{E}{V} = \frac{E_D}{V} + \frac{E_P}{V} + \frac{E_H}{V} \qquad (2.5)$$

$$\delta^2 = \delta_D^2 + \delta_P^2 + \delta_H^2 \qquad (2.6)$$

The application of solubility parameters for predicting ESC was firstly suggested by Kambour et al. [63]. The correlation between the ESC behavior of plastics with the solvent solubility parameter was performed using the criterion of a critical strain for crazing/ cracking, as shown in Figure 2.4. In several cases, a distinct minimum in critical strain versus solubility parameter was noted as the solubility parameters of the polymer (δ_p)

and solvent (δ_a) approach one other. However, for some polymers, such as PC and poly-sulfone (PSF), two minimum critical strains were observed. Using this diagram, the ESC behavior can be estimated based on the liquid-polymer interaction. The closer together the solubility parameters between liquid and polymer, the greater the solvation or plasticization due to the higher chemical and structural compatibility. Thus, the polymer will dissolve in the liquid or will be cracked immediately. Crazing promoted by ESC is more likely occur if the solubility parameter of the liquid and polymer are different [64]. A much different solubility parameter leads to a better ESC resistance.
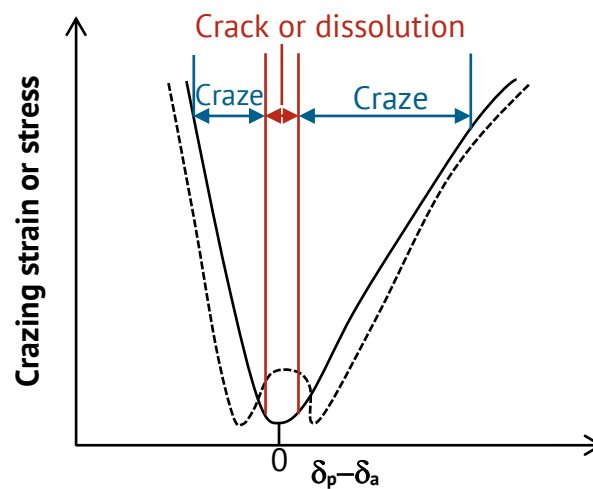
Figure 2.4: Generalized behavior of critical strain/stress versus solubility parameter difference between polymer and the environment liquid (adapted from references [65][64]).

Kjellander et al. [66] indicated that some "non-absorbing" chemicals, such as butter, can reduce the ESC resistance of PC due to the sufficiently similar of solubility parameters. This allowed surface conformational changes, which resulted in the development of stress on the surface, and thus initiated crazing and cracking in PC. Alperstein [48] applied molecular modeling techniques to predict the ESC behavior of PC in different fluids. Experimental work supports the computational finding that the ESC behavior of PC in the presence of stress cracking agents (toluene and water) can be addressed by the solubility parameter. The different behavior between different stress cracking agents was related to their different interactions with the PC chains.

Additionally, Hansen [61,62] and Hansen et al. [60] established that the ESC behavior in polymers not only depends on the solubility parameters of the solvent relative to those of the polymers but also relates to the molecular size and shape of the stress cracking agents. The ESC resistance is reduced when the stress cracking agents have a smaller

molecular size and a less bulky molecular structure, which results in rapid diffusion of the stress cracking agent into the polymer structure. Recently, Nomai et al. [8] also stated that the correlation of the critical stress intensity factor (mode I) with the Hansen solubility parameter showed a very good agreement for different fluids. The stress cracking agents that have lower molar volumes and closer solubility parameters relative to those of the polymers, accelerated the process of macroscopic brittle crack formation, thus reducing ESC resistance of the PC.

Temperature

Apart from the stress cracking agent properties, the environment temperature also noticeable impacts the ESC behavior of polymers. As the temperature is increased, the polymer chains are further apart, thus increase free volume and kinetic energy. This contributes to greater transport of the stress cracking agent into the polymer structure and accelerates the disentanglement process during ESC failure.

According to Wright [47], the value of the stress and strain rate required to initiate ESC decreases as the temperature increases, consequently accelerating the cracking process. Lustiger [67] also stated that the ESC resistance of PE is particularly sensitive to temperature. The crack propagation rate doubled with increasing temperature only 7°C. Soni et al. [68] showed that the strain at break of low-density polyethylene (LDPE) was significantly decreased with the presence of a stress cracking agent. This effect was more pronounced with increasing temperature from 30 to 60°C. An inhomogeneous deformation of LDPE film was observed with the presence of aggressive environments and with increasing temperature. The simultaneous effects of "solvation" of the amorphous regions and "plasticization" at the defect sites in the crystal region occurred during the deformation process of the material. This was responsible for the inhomogeneity of the material's deformation.

2.2.3   Environmental Stress Cracking of Polymer Nanocomposites

As already discussed, reinforcing polymers with small amounts of nano-sized fillers is one of the most effective methods for improving polymer properties. However, up until recently, only a few studies have reported the behavior of reinforced polymers in terms of ESC resistance. In fact, the incorporation of nanofiller into polymers could generally cause two contrary effects on ESC behavior. On the one hand, the extensive internal interface

between the nanofiller and the polymer matrix can support the absorption of the stress cracking agent and thereby reduce the ESC resistance of the materials. On the other hand, it can improve the ESC resistance by controlling new structural arrangements on the molecular scale, promoting effective energy dissipation in the fracture process. It depends on which effect will be dominant. Therefore, particular attention is paid to the effect of nanofiller on the ESC resistance behavior of polymers.

Pons et al. [9] found that the ESC resistance of poly(lactic acid) (PLA) in water improved with the addition of glass fiber. Saharudin et al. [10] also reported that the incorporation of halloysite nanoclay improved the environmental stress cracking resistance of polyester in methanol by increasing both fracture toughness and failure time. Similarly, Rull et al. [11] found that the addition of organo-modified bentonites to polyester effectively reduced water absorption and improved the performance of the composite in a humid environment. Lin et al. [6] also investigated the ESC resistance of PC reinforced with nano-SiO_2 particles under constant loading using an optical technique. They found that the incorporation of nanofiller improves the ESC resistance, and accordingly increases the service lifetime of PC nanocomposites in isopropanol significantly. Moreover, the effect of nano-fillers geometries such as nanoclay platelets, halloysite nanotubes (HNTs), and nanosilicon carbide (n-SiC) particles on the mechanical performance of epoxy-based nanocomposites in a humid environment was investigated by Alamri et al. [69]. They found that the fracture toughness and impact strength of all types of nanocomposites increase after exposure to water because of plasticization effect of water and increased of fiber bridging. The enhancement was more pronounced for nanocomposites filled with n-SiC than for those filled with nanoclay platelet and halloysite nanotubes.

Additionally, some research has studied the effect of nanofiller on the ESC resistance of polymer in different fluids. For example, Bonia et al. [12] examined the ESC resistance of rubber-toughened polyester/clay nanocomposites in sodium hydroxide and hydrochloride acid solutions. They found that the incorporation of organically modified montmorillonite into rubber-toughened polyester produced a product with improved ESC resistance in both stress cracking agents. The nanocomposite has the fastest diffusion rate in the acid agent followed by the base agent. Zhou et al. [13] also studied the craze formation and crack propagation of nanosilica-filled PC in different environments using a bent strip test with constant strain and a creep test with static constant stress. They observed that the ESC resistance of PC significantly improved with the addition of nanofiller. However, PC exposed to toluene failed much earlier than that in isopropanol because of a faster diffusion rate of toluene into the PC matrix. Recently, our previous research [8]

also found that the addition of nano-SiO_2 greatly improved the ESC resistance of PC in all investigated fluids (isopropanol, methanol, aqueous urea solution, and deionized water), especially if the type/shape of the deformation area in front of the crack changes completely, as in mild agents. The most important finding was that the behavior of the polymer-based nanocomposites/stress-cracking-agent-combinations can be scaled using the Hansen solubility parameter, thus, allowing the prediction of the stress cracking behavior as a function of the filler content for different stress cracking agents.

2.2.4 Different Conventional ESC Testing Methods

Since a premature failure due to ESC is a major safety and economic concern, the determination of the ESC behavior of materials and components is an essential part of a product development process. There are a variety of standardized tests available for determining the ESC resistance, which can be divided into two groups, stress (force) controlled tests and strain (deformation) controlled tests. A brief overview of the standardized ESC tests from both methods that are usually applied for assessing the ESC resistance of thermoplastics is given in the following section.

2.2.4.1 Constant Deformation (Strain) Tests

Bell Telephone Test or Bent Strip Tests

The bent strip test (ASTM D1693) was first developed by Bell Laboratories in the USA for testing the ESC performance of flexible polymers such as PE [70]. In this test, rectangular strips specimens (38 x 13 x 3 mm) are notched and bent (at an angle of 180°) in a metal U-shaped specimen holder, as illustrated in Figure 2.5. The maximum surface strain (ε_{max}, %) can be calculated using the following equation:

$$\varepsilon_{max} = \frac{t}{w - t} \times 100 \tag{2.7}$$

where t = Thickness of the sample

w = Width of the holder

After loading, the holder specimens are immediately exposed to the chemical environment (10 vol.% Octylphenoxy poly(ethyleneoxy)ethanol solution, Igepal CO-630) and placed in a water bath at 50°C. Then, the specimens can be inspected either visually or by the automatic technique developed by Saeda and Suzaka [71]. Failure is determined

as the appearance of any visible crack, as seen in Figure 2.5(b). The time required for 50% of the specimens to fail is used as a reference point.
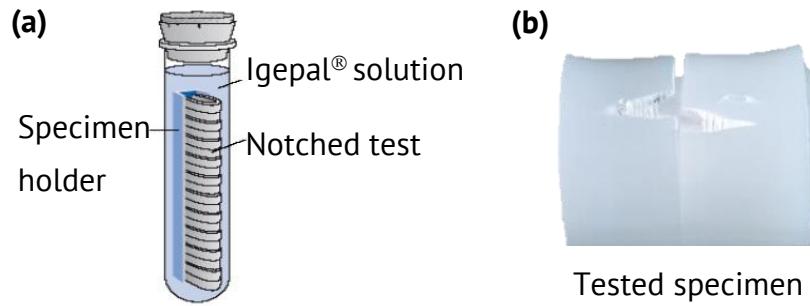
Figure 2.5: (a) Bent strip test for flexible polymers and (b) visible crack in tested specimen (adapted from references [72][73]).

Three-Point Bending Test

The three-point bending test generates a deflection to the middle of a test specimen due to an application of maximum surface strain at this position. This test can be performed in two major gauge variants, as shown in Figure 2.6. The sample is clamped on devices with a certain strain, which can be adjusted by a screw. The maximum surface strain (ε_{max}, %) can be calculated using equation 2.8, as follows:

$$\varepsilon_{max} = 6\delta t L \times 100 \tag{2.8}$$

where δ = Midpoint deflection

t = Thickness of the sample

L = Effective length of the beam/specimen

Once the specimen has been strained, it is quickly immersed in the stress cracking agent. After a set time, the specimen is removed and rinsed with distilled water and then dried for 24 hours at room temperature. Following this, the crazing/cracking and tensile properties of the specimens are investigated.
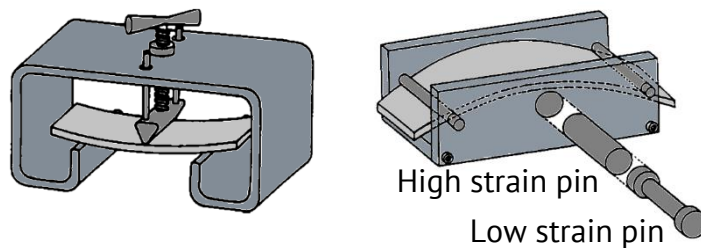
Figure 2.6: Three-point bending apparatus for ESC testing (adapted from reference [47]).

Four-Point Bending Test

The ESC behavior of thermoplastics can also be investigated using a four-point bending test method according to EN ISO 22088-3: 2006. In this test, the specimen is clamped with one of its surfaces on a bending template with a constant radius of curvature, which causes a constant strain. The maximum surface strain (ε_{max}, %) can be calculated using equation 2.9. Different holder radiuses allow for different strain levels.

$$\varepsilon_{max} = \frac{t}{2r + t} \qquad (2.9)$$

where t = Thickness of the sample

r = Radius of the forming holder

Once the specimen is strained, it is brought into contact with the stress cracking agent immediately, as seen in Figure 2.7. Following this method, crazing/cracking can be inspected either visually or by using an online optical detection technique which was recently developed [74].
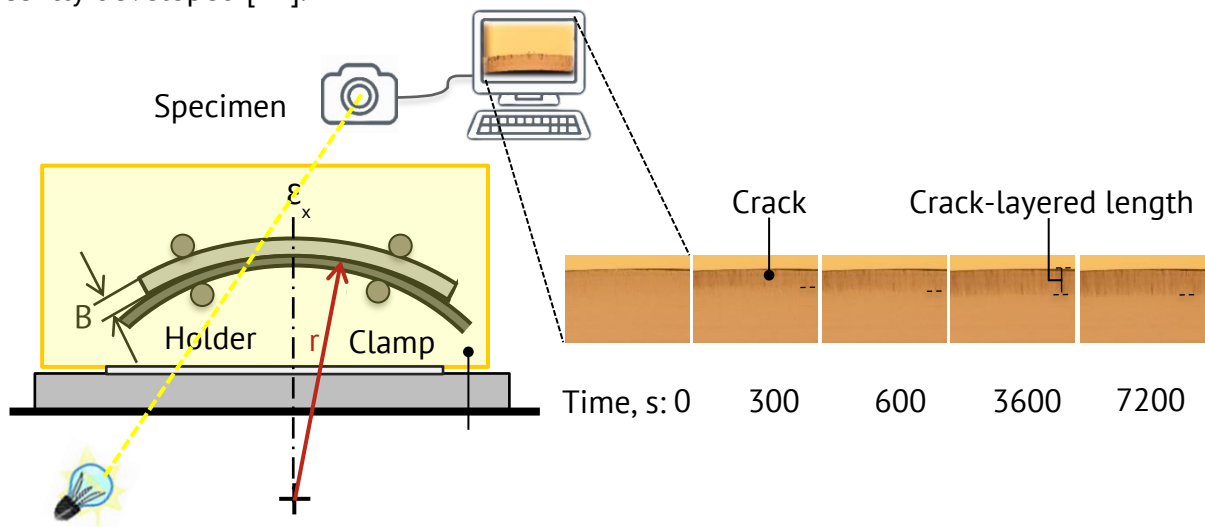
Figure 2.7: Schematic of the four-point bending test with an optical crack detection (adapted from reference [74]).

Generally, the constant deformation test is commonly applied for assessing the ESC resistance of amorphous polymers. As the stress applied to the specimen will decrease during testing, it is not suitable for testing with semi-crystalline polymers, due to their rapid stress relaxation.

2.2.4.2 Constant Load (Stress) Tests

Constant Tensile Stress Tests

In this test, a specimen is subjected to constant tensile stress (below the tensile yield stress of the polymer) under plane strain conditions in air or stress cracking agent at various temperatures. An illustration of the device used for the constant load test is shown in Figure 2.8. The ESC resistance is determined as the time required for crazing/cracking or the threshold stress which no crazes appear in a specific time (typically 100 hours).

Similar to the common test at constant load, the Rapra high-temperature tensile creep rupture test was developed, as seen in Figure 2.8(b). This test involves the application of constant tensile stress and the rupture time of the materials. In this test, the change in length (strain response) under constant stress is recorded. In addition to these standardized tests, a monotonic creep testing machine has been developed by Hough and Wright [47]. The monotonic creep method is capable of high-resolution and discrimination in a short time. This method employs a similar tensile creep machine, but the weight pan is replaced by a blow-molded vessel. In this test, the strain response to a constant stress rate is monitored. By using this method, the deviation of the stress-strain characteristics in air and in the fluid is found. Then, the critical time, critical stress, and critical strain can be evaluated and used as a criterion for the initiation of ESC.
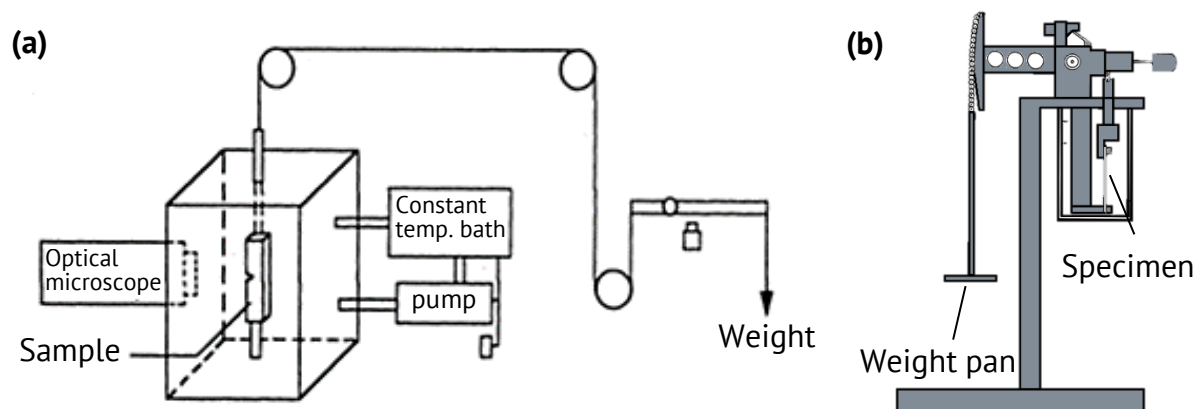
Figure 2.8: Test set-up apparatus for (a) constant tensile stress tests and (b) Rapra high temperature tensile creep rupture (adapted from references [47,53]).

Each of these methods has different advantages and disadvantages. The suitable method for assessing the ESC performance of a specific material should be selected based on the end-use conditions (i.e., constant stress or constant strain) and on the failure criterion [5].

2.2.5   Fracture Mechanics Testing for ESC Investigation

A fracture mechanics framework has attracted increasing interest and is considered as an alternative method for assessing the ESC phenomena [5,75,76]. Fracture mechanics are the fracture analysis of materials containing defects, which could be internal flaws, microcracks, or surface scratches due to manufacturing or external damage. Once the force is applied, the presence of the defect initiates a local distribution of stresses in the materials, as indicated in Figure 2.9. The stress in y-direction reaches a maximum value (σ_m) at the surface of an ellipse crack (x=0) and tends to decrease with distance away from the defect (x increase). In contrast, the stress in the x-direction is zero on the surface of an ellipse crack and increases as x increases, reaching a maximum value close to applied stress (σ) and decreasing to zero at a large distance from the crack. The amplification of the applied stress at the crack tip, which was proposed by Inglis [64], can be calculated using equation 2.10. This relationship indicates that a sharp crack ($a>>b$) causes a concentration of stresses with the highest amplification at the crack tips. Even at low applied stress, the stress can reach the material strength and consequently lead to crack propagation in the material via the crack tip.
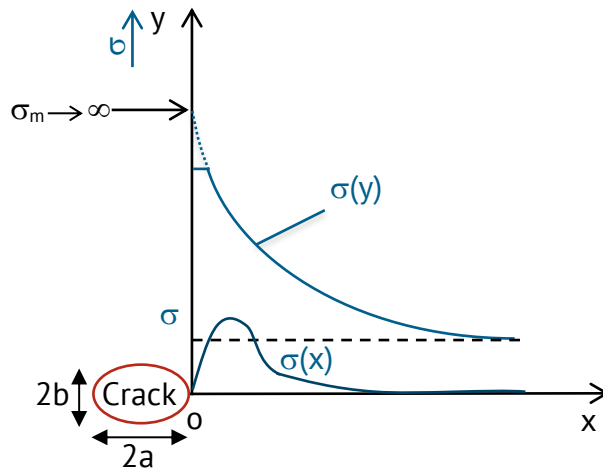
$$\frac{\sigma_m}{\sigma} = 1 + \frac{2a}{b} \qquad (2.10)$$

where σ_m = Maximum value of stress

$\qquad \sigma$ = Applied stress

$\qquad a, b$ = Dimension of crack

Figure 2.9: Distribution of local stresses in an elastic lamina body with the presence of internal elliptical crack.

Based on this theory, stress amplify at the crack tip depends only on the geometric shape of the crack but not on its absolute size. This is contrary to the well-known principle that larger cracks are propagated more easily than smaller ones. Therefore, the solution to this problem is given by Griffith's theory, which is discussed in detail in the following section

Griffith's Theory of Fracture

Griffith's Theory is based on the energy changes due to a crack propagating in a material. In this theory, a thin lamina plate with a certain thickness (B) containing a sharp internal crack with a certain length ($2a$) perpendicular to the direction of applied stress (σ) is considered, as indicated in Figure 2.10. The total energy of the system is divided into two parts, the stored elastic energy and the work done in crack propagation. The total stored elastic strain energy (U_s) for a sharp elliptical crack under a uniformly applied stress can be approximated using equation 2.11:

$$U_s = (\text{crack})\text{volume of cylinder} \times \frac{\sigma^2}{2E} = \frac{\sigma^2 \pi a^2 B}{2E} \tag{2.11}$$

where E = Elastic modulus of material

Griffith's Theory assumes that no heat is dissipated and the work done for two new surface formations takes place without plastic deformation. Thus, the work done to form a crack length $2a$ (U_γ) can be calculated using equation 2.12.

$$U_\gamma = \text{Surface area of crack} \times G_c = 2aBG_c \tag{2.12}$$

Where G_c = Work done to propagate a unit area of crack

Finally, the total energy change (ΔU) of the system can be calculated using equation 2.13.

$$\Delta U = \frac{\sigma^2 \pi a^2 B}{E} + 2aBG_c \tag{2.13}$$

The dependence of different energy changes on crack length is shown in Figure 2.10(b). It is clearly seen that the work done for producing the new crack surface increase linearly with the crack length. In contrast, the stored elastic energy shows a parabolic decrease as a function of crack length. Concerning the total energy change at a small crack length, the work done for crack propagation is dominant. For a large crack length, the decrease of stored elastic energy becomes dominant. Griffith proposed that crack propagation occurs if the energy required to produce the new surface is balanced by a decrease in the elastic stored energy, as indicated by a maximum ΔU point (slope=0) [64].

Accordingly, the strain energy release rate (G_c) for plane stress and plane strain materials are easily derivable, as shown in equations 2.14 and 2.15, respectively.

For plane stress:

$$\sigma_F = \left(\frac{EG_c}{\pi a}\right)^{1/2} \tag{2.14}$$

For plane strain:

$$\sigma_F = \left(\frac{EG_c}{\pi(1-v^2)a}\right)^{1/2} \tag{2.15}$$

where σ_F = Appied stress

$\quad G_c$ = Strain energy release rate

$\quad E$ = Young's modulus

$\quad v$ = Poisson's ratio

$\quad a$ = Crack length
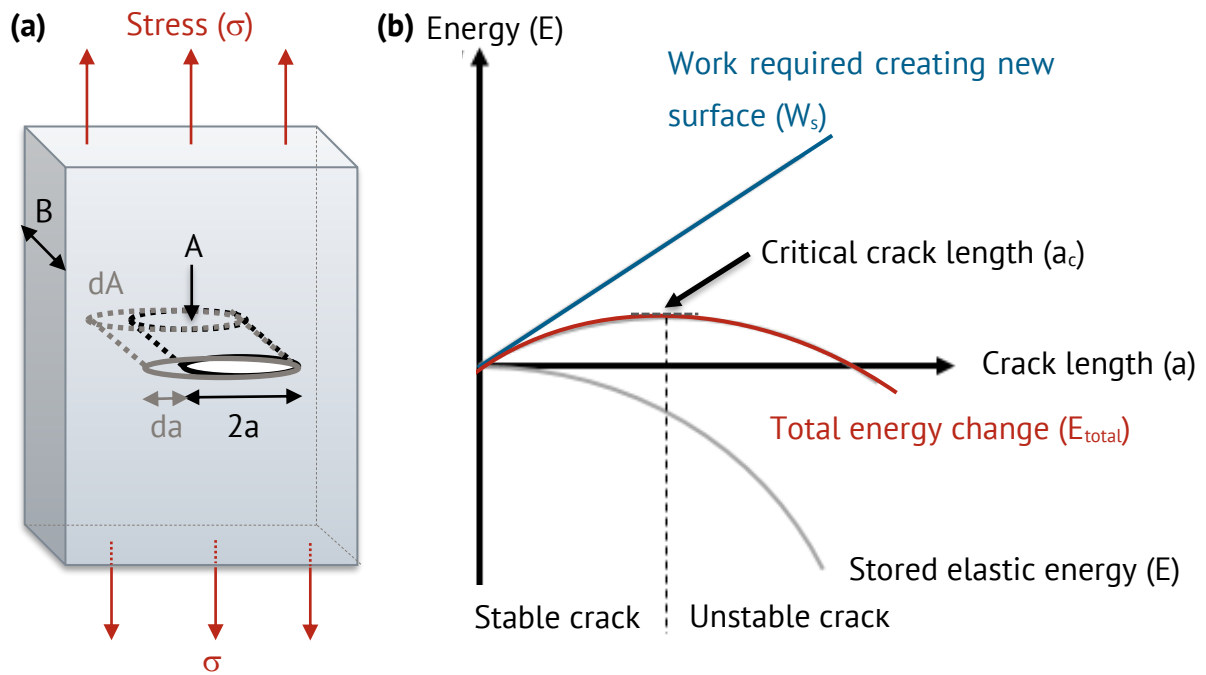
Figure 2.10: (a) thin lamina body containg sharp crack subjected to uniform stress and (b) dependence of the total energy change as a fuction of crack length.

Irwin's Modification Theory

Irwin developed the field of fracture mechanics using the early work of Griffith. A term of strain energy release rate and surface energy was replaced by stress intensity and fracture toughness, respectively [64,77]. The distribution of stress field $\sigma(r,\theta)$ in the vicinity of an infinitely sharp crack tip can be mathematically described by the following equation:

$$\sigma_{yy} = \frac{K_I}{\sqrt{2\pi r}} \cos\frac{\theta}{2}\left(1 - \sin\frac{\theta}{2}\sin\frac{3\theta}{2}\right) \tag{2.16}$$

Stress intensity factor (K_I) is defined as:

$$K_I = \sigma Y \sqrt{\pi c} \tag{2.17}$$

where σ = Applied stress

Y = Geometry factor

c = Crack half-length

The cylindrical polar coordinates of a point with respect to the crack tip for equations 2.16–2.17 is shown in Figure 2.11. For a particular crack system where π and Y are constants, the stress intensity factor indicates that the magnitude of the stress at position (r,θ) depends on the external stress applied and the square root of the crack length. If the $K_I \geq K_{Ic}$ (critical stress intensity factor), fracture of the material occurs. On the basis of equations 2.14, 2.15, and 2.17, the relationship between K_{Ic} and G_C for plane stress and plane strain materials is obtained as described in equations 2.18 and 2.19, respectively.

For plane stress:

$$K_{IC} = (E G_c)^{1/2} \tag{2.18}$$

For plane strain:

$$K_{IC} = \left(\frac{E G_c}{1 - \nu^2}\right)^{1/2} \tag{2.19}$$
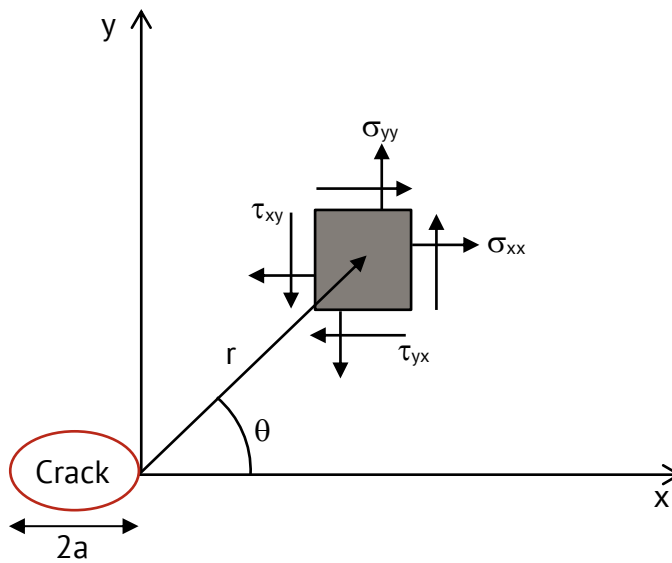
Figure 2.11: Sharp crack length in an infinite lamina subjected to a tensile stress (adapted from reference [64]).

The subscript I in K_I is associated with tensile loading mode. In fact, there are three main loading modes for determining stress intensity factors as follows (Figure 2.12):

- Mode I-opening: a tensile stress normal to the crack plane
- Mode II-in plane shear: a shear stress acting parallel to the crack plane and perpendicular to the crack front
- Mode III-out of plane shear: a shear stress acting parallel to the crack plane and parallel to the crack front

However, Mode I loading is the most common type that leads to brittle failure. Thus, the focus in this work is mainly on Mode I loading.

Mode I: Opening   Mode II: In-plane shear   Mode III: Out-of-plane shear
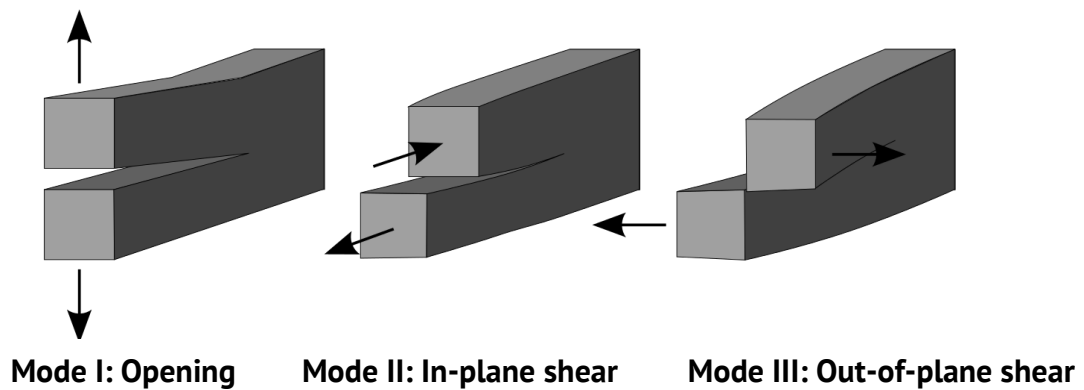
Figure 2.12: The three main fracture modes (adapted from reference [77]).

Fracture Mechanics Testing (Mode I) for ESC Investigation

By using fracture mechanics for ESC investigation under a constant static loading method, the macro-crack growth rate (da/dt) as a function of crack-tip stress intensity factor (K_I) can be used for determining the ESC performance of the materials. Generally, the entire process of crack propagation of the polymer can be divided into three stages (see Figure 2.13):

- The 1st stage−crack initiation: if $K_I < K_{Ith}$, the crack does not propagate and the material can withstand the applied load for an unlimited time.
- The 2nd stage−crack propagation: if $K_I > K_{Ith}$, the crack starts to propagate and the crack propagation rate increases linearly with K_I.
- The 3rd stage−final material failure: if $K_I > K_{Ic}$, unstable crack propagation begins and the material fractures in a short time.

The relationship between crack propagation rate and stress intensity factor in the stable crack growth phase can be described by the Paris−Erdogan law:

$$\frac{da}{dt} = AK^m \tag{2.20}$$

where *A* and *m* are constants, which are depends on the material performances and test conditions.
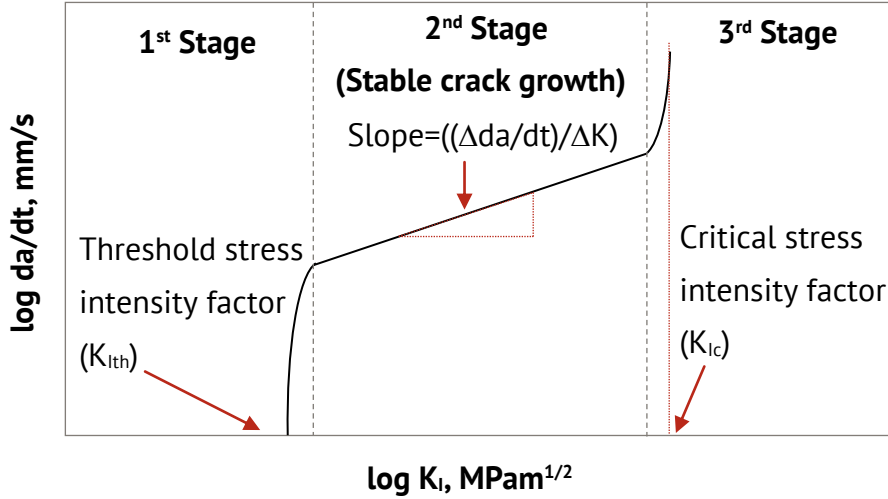
Figure 2.13: Macro-crack propagation rate as a function of K_I factor of the polymer.

2.2.6 Time-Temperature Superposition Principle

The analysis of long-term material damage mechanisms takes a long time under normal circumstances. Therefore, accelerated testing methodologies have been used for the prediction of long-term response of the materials. The time-temperature superposition principle (TTSP) is one of the most widely used to construct master curves referred to a constant temperature [78,79]. An example is shown in Figure 2.14 and equation 2.21, the modulus (*E*) at a certain temperature (*T*) and time (*t*) is horizontally shifted along the time axis to a reference temperature (T_{ref}) using shift factor (a_T). Two empirical equations, the Williams–Landel–Ferry (WLF) equation and the Arrhenius equation, commonly used to describe the mathematical relationship between time and temperature in term of shift factors [80] are shown in equations 2.22 and 2.23, respectively. Many studies demonstrate that TTSP is valid in the linear viscoelastic region for polymers and polymer composites [80,81]. Pedrazzoli et al. [80] studied long-term creep behavior of PP fumed silica nanocomposites using time-temperature and time-strain superposition approaches. They found that both approaches evidence a noticeable stabilizing effect induced by nanoparticles, which is more effective for higher creep stresses and at high temperatures.

In this study, the superposition approach has been applied to construct a master curve of crack propagation model from the available short-term tests at different temperatures. Adapted from the time-temperature superposition principle, master curves of crack propagation models are constructed by shifting the horizontal crack propagation rate (in the stable crack growth region) at various temperatures to the reference temperature using the shift factor (a_T). This approach will be described in detail in section 4.1.5.9: Prediction of ESC behavior of PC nanocomposites using a modified supposition approach.

$$E(T,t) = E(T_{ref}, \frac{t}{a_T}) \tag{2.21}$$

WLF equation:

$$log a_T = \frac{-C_1 \cdot (T - T_{ref})}{C_2 + T - T_{ref}} \tag{2.22}$$

Arrhenius equation:

$$log a_T = \frac{E_a}{R}\left(\frac{1}{T} - \frac{1}{T_{ref}}\right) \tag{2.23}$$

where a_T = Shift factor

T = Elevated temperature

T_{ref} = Reference temperature

C_1, C_2 = Material constant values

E_a = Activation energy

R = Ideal gas constant
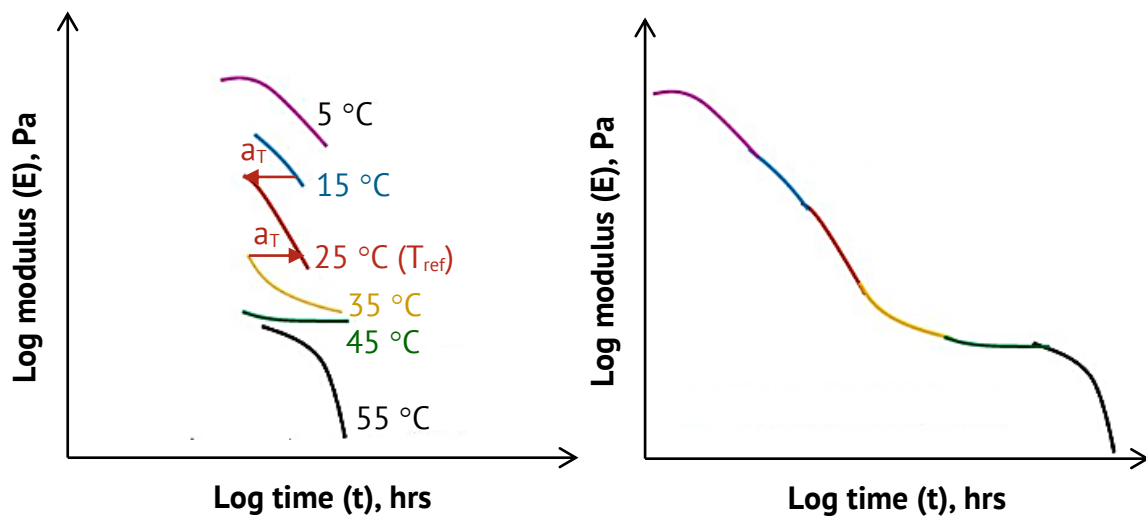
Figure 2.14: Schematic of curve shifting according to general time-temperature superposition [adapted from reference [82]].

As reviewed, the incorporation of small quantities of nanofillers into polymer matrices has been shown to be an effective method for enhancing the mechanical performance of materials. However, very few studies have addressed the influence of nanofillers on the ESC behaviors of polymer. Therefore, it is of great interest to investigate whether the ESC resistance of a polymer can be positively influenced by nanoparticles, especially for amorphous polymers, which are the most susceptible to ESC failure. Moreover, the effects of the intrinsic properties of polymers and external environmental parameters on the ESC behavior of polymer nanocomposites will be investigated to gain a deep understanding and to suggest a model for describing the dependence of ESC behavior based on these parameters.

3   Experimental Procedures

3.1   Materials

3.1.1   Thermoplastic Matrices

In this study, amorphous based polymers were used as polymer matrices. Two different molecular weights of bisphenol A polycarbonate (PC) (high molecular weight PC (PC-H, Makrolon RX 1805) and low molecular weight PC (PC-L, Makrolon 2405)) were supplied by Bayer Materials Science/Covestro AG, Germany. The average molecular weights (M_w) for the PC-H and PC-L are 31,000 g/mol and 24,000 g/mol, respectively. Impact-resistant polystyrene (PS, Terlux HD 2802) was provided by INEOS Styrolution, Germany. Polymethyl methacrylate (PMMA, Plexiglas 6N) was supplied by Evonik Industries AG, Germany. The most important characteristics of the polymer matrices used in this work, based on information from the manufacturer, are listed in Table 3.1.

Table 3.1:   Characteristics of the polymer matrices used in this work

Properties	Unit	Matrix			
		PC-H	PC-L	PS	PMMA
Density	Kg/m^3	1200	1200	1080	1190
Young's modulus	MPa	2400	2400	2000	3200
Tensile strength	MPa	67	65	48	67
Strain at break	%	>50	>50	12	3
Charpy impact strength (23 °C)	kJ/m^2	NB	NB	120	20
Glass transition temperature (10 °C/min)	°C	145	144	107	99
Water absorption	%	0.3	0.3	0.7	1.8
Refractive index	-	1.59	1.59	1.54	1.49

Note: NB = Not break

3.1.2   Nanofillers

As nanofiller, two different sizes of hydrophobic fumed nano-SiO_2 with the mean particle diameters of 7 nm (Aerosil R812s) and 12 nm (Aerosil R8200) from Evonik Industries, Germany were used. Their specifications referred to the information of manufacturers are listed in Table 3.2.

Table 3.2:   Specifications and properties of the nanofillers

Properties	Unit	Nanofiller	
		SiO_2 (R812s)	SiO_2 (R8200)
Diameter of primary particles	nm	7	12
Specific surface area	m^2/g	220±25	160±25
SiO_2 content	%	≥99.8	≥99.8
Surface treatment	-	Hexamethyldisilazane	Hexamethyldisilazane
Density	Kg/m^3	~2	~2
Young's modulus	MPa	73	73
Refractive index n	-	1.45	1.45

3.2   Preparation of Nanocomposites

3.2.1   Extrusion

Polymer granules were pre-dried to avoid hydrolytic degradation during the manufacturing process. In order to obtain effective dispersion and distribution of the nanoparticles in a polymer matrix, a two-step melt-compounding process was applied to all the nanocomposites. Neat polymer and nano-SiO_2 particles were first compounded into a master batch using a co-rotating twin-screw extruder (ZSE 18 MAXX, Leistritz, Nürnberg, Germany). The processing temperature profile (from feeder to die) and the screw speed were set for each of the different materials, as shown in Table 3.3. Then, the obtained polymer filled with SiO_2 master batch was diluted to the desired nano-SiO_2 particle content by using the same extruder under identical processing conditions. After exiting the die, the extruded was cooled in water before being granulated using a pelletizer. The designation and composition of the materials is shown in Table 3.4.

Table 3.3:   Extrusion parameters of different materials

Materials	Temperature, °C	Screw speed, rpm
	From feeder to die zone	
PC-L/SiO_2	130/200/220/240/270/270/270/270/270/270	125
PC-H/SiO_2	130/200/220/240/280/280/280/280/280/280	125
PS/SiO_2	100/160/220/240/270/270/270/270/270/270	110
PMMA/SiO_2	100/180/210/220/240/240/240/240/240/240	100

Table 3.4:   Sample designation and composition of different materials

Designation	Composition	Part (volume ratio)
PC-L-S0	PC-L	100/0
PC-L-S0.5		99.5/0.5
PC-L-S1		99/1
PC-L-S2	PC-L/SiO_2	98/2
PC-L-S3		97/3
PC-L-S4		96/4
PC-H-S0	PC-H	100/0
PC-H-S0.5		99.5/0.5
PC-H-S1	PC-H/SiO_2	99/1
PC-H-S4		96/4
PS-S0	PS	100/0
PS-S0.5		99.5/0.5
PS-S1	PS/SiO_2	99/1
PS-S4		96/4
PMMA-S0	PMMA	100/0
PMMA-S0.5		99.5/0.5
PMMA-S1	PMMA/SiO_2	99/1
PMMA-S4		96/4

3.2.2   Injection Molding

After extrusion, the neat polymers and their compound granules were pre-dried and then injection-molded into $50 \times 50 \times 4$ mm^3 sheets using an injection molding machine (ENGEL victory 80, ENGEL Austria GmbH, Schwertberg, Austria) for further tests. A detailed description of the injection molding parameters is given in Table 3.5.

Table 3.5:   Injection molding parameters of different materials

Materials	Temperature, °C		injection speed, mm/s
	From feeder to nozzle zone	Mold	
PC-L/SiO_2	270/280/280/280	80	200
PC-H/SiO_2	290/300/300/300	85	200
PS/SiO_2	240/250/250/250	60	200
PMMA/SiO_2	235/245/245/245	60	195

3.3   Preparation of Testing Specimens

The specimens used for testing in terms of their mechanical properties, surface wetting/ absorption, and environmental stress cracking (ESC) resistance properties were milled from the injection-molded sheets, as shown in Figure 3.1.
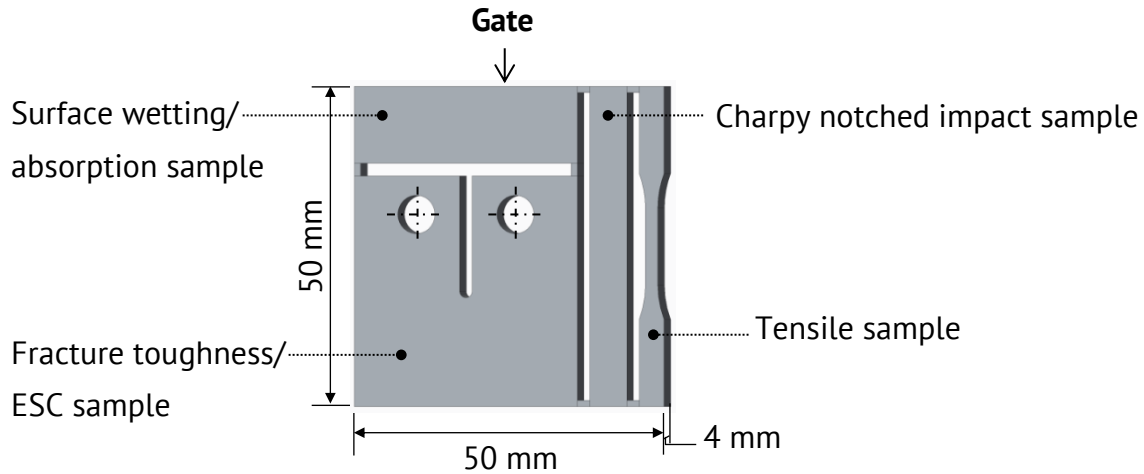
Figure 3.1:   Preparation of testing specimens from injection-molded sheets.

3.4   Characterization of Morphological Structure

Morphological Properties of Particle Dispersion

To examine the morphological properties of filler dispersion, the rectangular specimen from central part of the injection molded plate was fractured by immersing it in liquid nitrogen and breaking it using two grips. The dispersion quality of the nanoparticles in the polymer matrix was studied using a scanning electron microscope (SEM) (SU8000, Hitachi, Japan). Before undergoing analysis, the cryogenic fracture surfaces were sputter-coated with a thin iridium layer. An acceleration voltage of 5 kV was used to collect SEM images of the samples. The equivalent agglomerated size of the nanoparticles was then analyzed using an image analysis technique with an optical microscope (Nikon ECLIPSE LV100POL, Nikon, Japan). The image was firstly converted to a binary image and a thresh-old limit was then specified to distinguish the objects of interest (agglomerated nanoparticles) from the background (polymer matrix). The equivalent diameter was a size feature derived from the area. The automated program determined the diameter of a circle with the same area as the measured object, as demonstrated in Figure 3.2 and equation 3.1.
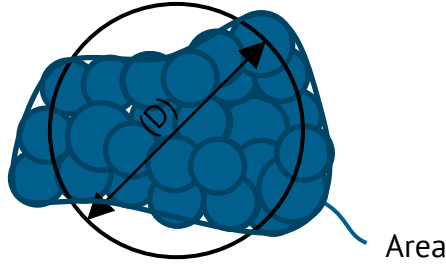
$$Equivalent\ diameter\ (D)\ =\ \sqrt{\frac{4\ \times Area}{\pi}} \qquad (3.1)$$

Figure 3.2: Measurement feature of the equivalent diameter.

Morphological Properties of Fractured Surfaces

The fractured surfaces of failed ESC-test specimens were examined by using a stereo microscopy (SZH, Olympus) and a Scanning Electron Microscope (SEM) (SU8000, Hitachi). Similarly, the fractured surfaces were sputter-coated with a thin iridium layer before analysis. The acceleration voltage of 5 kV was also used to collect SEM images of the samples.

3.5   Characterization of Optical Properties

Optical characterization was carried out according to ASTM D 1003 standards using a haze meter (BYK-Gardner haze-gard plus, BYK-Gardner GmbH, Germany). The injected plate with dimensions of 50 x 50 x 4 mm³ (length x width x thickness) was used as a specimen. As seen in Figure 3.3, an incident light beam Φ_0 was focused on a sample, and a weaker undeviated beam Φ_t was transmitted on the far side. The forward-scattered light flux is denoted by Φ_f, and the scattering angle can be subdivided into two ranges: 0°–2.5° and 2.5°–90°. The transmittance is defined as the fraction of the incident light passing through a specimen, while clarity and haze are defined as the percentages of transmitted light at scattering angles between 0°–2.5° and 2.5°–90° relative to the direction of incident light, respectively [83]. Quantitative evaluations of the optical properties were carried out based on the following equation:

$$L_D = \frac{\Phi_t}{\Phi_0} \qquad (3.2)$$

$$L_T = \frac{\Phi_t\ +\ \Phi_f}{\Phi_0} \qquad (3.3)$$

$$H = \frac{(\Phi_f)_{2.5}^{90}}{\Phi_t\ +\ \Phi_f} \qquad (3.4)$$

where L_D, L_T, and H are the direct light transmittance, the total light transmittance, and the haze, respectively.
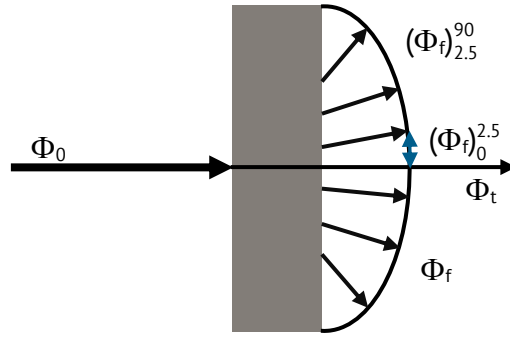
Figure 3.3: Definition of quantitative parameters for transparency characterization.

3.6 Characterization of Mechanical Properties

3.6.1 Tensile Test

The tensile properties of the polymer nanocomposites were determined using a universal testing machine (Zwick 1446, Zwick GmbH & Co. KG, Germany) according to DIN EN ISO 527-2/1BB (dog-bone-shaped specimens). The crosshead speeds were set to 1 and 50 mm/min for the determination of the Young's modulus and the other tensile properties, respectively. The tests were performed at room temperature (23±2°C) and a humidity of 50±10%. All data presented here are based on an average of at least five measurements.

3.6.2 Impact Test

Charpy notched impact tests were performed according to DIN 53453, using a Charpy impact tester (Ceast 9050, Instron, USA) with a 5J pendulum. The shape and dimension of the notch was milled in accordance with ISO 179/1eA. For each material, five specimens were tested at 23±2°C and 50±10% humidity. The impact strength (a_n) was calculated based on the absorbed impact energy (W) in accordance with equation 3.5:

$$a_n = \frac{W}{bh}$$

(3.5)

where b is the width and h is the height of the specimen.

3.6.3 Fracture Toughness Test

The fracture toughness was evaluated based on the ASTM D5045-99 and ASTM E399-90 standards, using a compact tension (CT) specimen. A pre-crack was made in the specimens

by lightly tapping a fresh razor blade into the bottom of the saw slot. The pre-crack length (a_0) ranged from $0.45 < a_0/W < 0.55$. The test was performed at room temperature with a testing rate of 0.5 mm/min using a universal testing machine (Zwick 1446, Zwick GmbH & Co. KG, Germany). The critical fracture toughness (K_{Ic}) was calculated using the following equation:

$$K_{Ic} = f(a_0/W) \cdot (F_{max}/BW^{1/2}) \tag{3.6}$$

where a_0 is the pre-crack length, B and W represent the specimen dimensions (4 mm and 30 mm, respectively), F_{max} is the maximal force in the force–displacement curve, and $f(a_0/W)$ is the calibration factor for CT specimen, which is given as:

$$f(a_0/W) = [(2 + a/W)/(1 - a/W)^{3/2}] \cdot [0.866 + 4.64(a/W) -$$
$$13.32(a/W)^2 + 14.72(a/W)^3 - 5.6(a/W)^4] \tag{3.7}$$
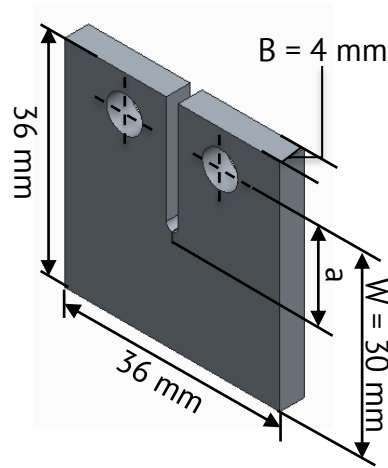
Figure 3.4: Dimensions of CT specimen.

3.7   Characterization of Thermal Properties

To investigate the thermal properties, thin sections were cut from the middle part of injected plate. The thermal properties of the PC nanocomposite were characterized using a differential scanning calorimeter (DSC) (TA Q20, TA instruments, Eschborn, Germany) equipped with an Refrigerated Cooling Systems 90 (RCS90) intracooler. Before the samples were measured, indium was used as a reference material to calibrate both the temperature scale and the melting enthalpy. The weight of each specimen ranged from 5 to 10 mg. Each sample was placed in an aluminium pan and was then completely closed with an aluminium lid. All samples were heated from 25°C to 250°C at a heating rate of

10°C/min (first heating scan) and were kept in an isothermal state for 5 min in a nitrogen atmosphere to erase the previous thermal history. The sample was then cooled to 25°C at a cooling rate of 10°C/min and heated again to 250°C at a heating rate of 10°C/min (second heating scan).

3.8   Characterization of Environmental Stress Cracking Properties

3.8.1   Absorption Test

Before testing, rectangular specimens with dimensions 36 x 12 x 4 mm³ were pre-dried to obtain their initial weight (W_0). Then, the specimens were immersed in ESC agents. At regular intervals, each sample was first removed from the agent and dried excess agent from its surface with a tissue before weighing. The absorption of the ESC agent was then measured by weighing the specimens using a balance (ABT 120-5DM, Kern & Sohn GmbH, Germany) that was accurate to ±0.01 mg. This procedure was repeated until equilibrium was reached. The percentage of liquid content (M_t) was calculated using the following equation:

$$M_t\ (\%)\ =\ [(W_t- W_0)/W_0]\ x\ 100 \tag{3.8}$$

where W_0 and W_t are the specimen weights before and after immersing, respectively.

The diffusion coefficient (D) of the different agents in the polymer can be determined from the slope of the line fitted to the percentage of the liquid content versus the square root of time as is shown in Figure 3.5 and equations 3.9 and 3.10, respectively.
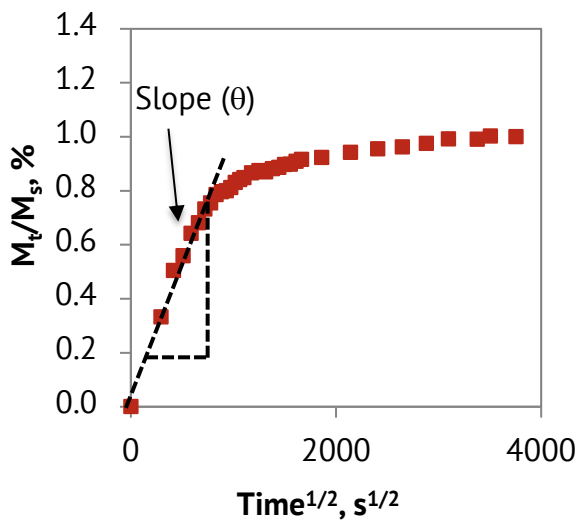
Fick's law for diffusion:

$$\frac{M_t}{M_S} = \frac{4}{l}\left(\frac{Dt}{\pi}\right)^{1/2} \tag{3.9}$$

$$D = 0.0625\,\pi l^2\,\theta^2 \tag{3.10}$$

where M_t = Mass uptake at time (t)

M_s = Mass uptake at equilibrium

L = Thickness of specimen

D = Diffusion coefficient

θ = Slope of curve in the plot

Figure 3.5: Weight gain of polymer as a function of square root of immersion time.

3.8.2 Surface Wetting Test

Contact angle measurements were carried out with contact angle meter (Krüss G2/DSAII, Hamburg, Germany), in order to access the wettability of the solid surface (neat polymer and its nanocomposite) by using three ESC agents: isopropanol, methanol and DI water. A standardized volume of 5 μL was dropped onto the sample surface with a syringe. Pictures of the drops were taken with a digital camera positioned on a contact angle analyzer, and the contact angle was then measured automatically from the captured images. Young's equation, which is shown in equation 3.11, is well known for the calculation of surface free energy based on the contact angle measurement.
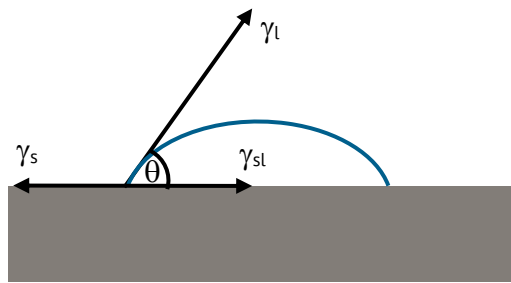
$$\gamma_s = \gamma_{sl} + \gamma_l \cos\theta \qquad (3.11)$$

where

$\gamma_{sl} = $ Surface free energy of solid-liquid interface

$\gamma_l = $ Surface free energy of a measuring liquid

$\gamma_s = $ Surface free energy of solid

$\theta = $ Contact angle between solid and liquid

Figure 3.6: Schematic of a liquid drop on a solid surface showing the quantities in Young's equation.

In this study, the surface free energy of solid-liquid interface was determined based on the method described by Girifalco and Good [84]:

$$\gamma_{sl} = \gamma_l \left(\frac{(1 + \cos\theta)^2}{4\Phi^2} - \cos\theta \right) \qquad (3.12)$$

the function Φ is given as equation (3.13).

$$\Phi = \frac{4(V_s V_l)^{1/3}}{(V_s^{1/3} + V_l^{1/3})^2} \qquad (3.13)$$

where $V_s = $ Molar volume of solid

$V_l = $ Molar volume of liquid

3.8.3   Fracture Mechanic Test

3.8.3.1   Experimental Setup

A schematic representation of the ESC experimental setup is shown in Figure 3.7. The CT specimens for ESC testing were prepared in the same way as the specimens for fracture toughness testing (section 3.6.3). All ESC tests were performed under constant loading (mode I, tension) in the presence of a stress cracking agent, at different temperatures between 23°C and 50°C. In order to obtain a suitable load for application to material for each ESC agent, an optimization load test must be performed using the load increase test. During the testing period, the macro-crack and the damaged area in front of the crack tip were completely surrounded by the ESC agent. Isopropanol (CAS number: 67−63−0), methanol (CAS number: 67−56−1), aqueous ethanol solution (CAS number: 64−17−5, 50% v/v), aqueous urea solution (CAS number: 57−13−6, 32.5% v/v), and deionized (DI) water (CAS number: 7732−18−5) were used as stress cracking agents. The values of the solubility parameters (δ) for the polymers and stress cracking agents and their molar volume are given in Table 3.6, and an overview of the ESC experiments with different testing agents is given in Table 3.7. The development of the macro-crack length and the crack damaged area were monitored and documented using a CCD camera (EOS 1200 D, Canon). All mages captured were saved on a computer for further analysis, and each ESC experiment was repeated at least three times to confirm the reproducibility of the experiment.
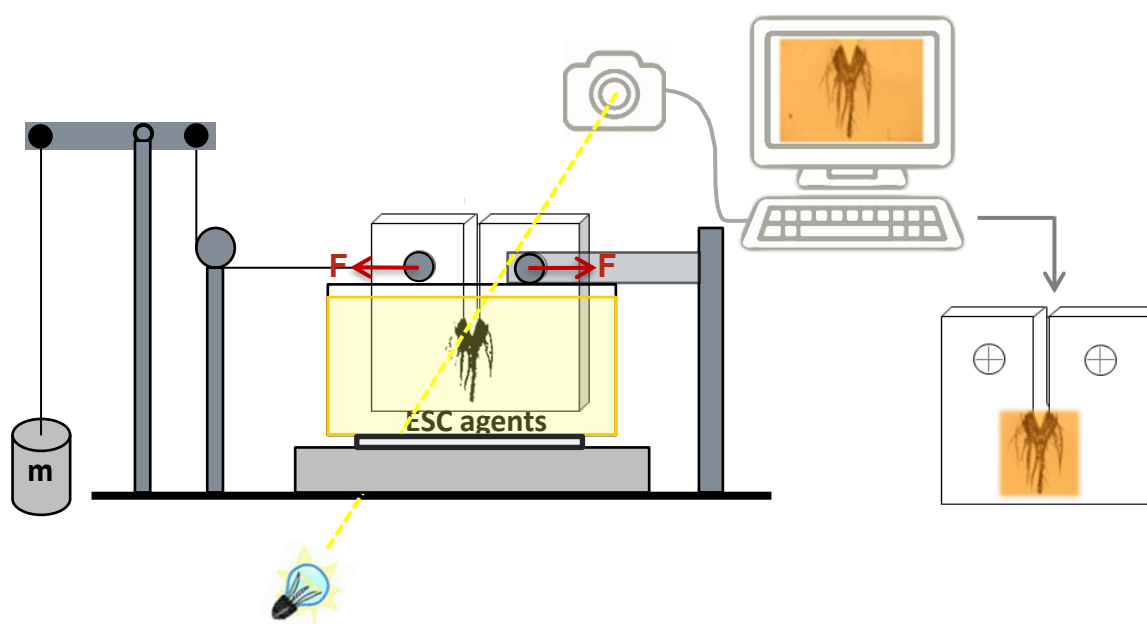
Figure 3.7: Schematic of the ESC test setup.

Table 3.6 Hansen solubility parameters of polymers and stress cracking agents [47].

Materials	Molar volume (cm³/mol)	Solubility parameter (MPa$^{1/2}$)			
		Dispersive, δ_D	Polar, δ_P	Hydrogen bonding, δ_H	Total, δ
PC	-	18.0	10.0	8.0	21.5
PMMA	-	17.7	6.7	6.2	20.0
PS	-	17.6	6.1	4.1	19.1
DI water	18.0	15.5	16.0	42.4	47.9
Ethanol	58.5	15.8	8.8	19.4	26.6
Isopropanol	76.8	15.8	6.1	16.4	23.5
Methanol	40.7	15.1	12.3	22.3	29.7
Urea	45.8	20.9	18.7	26.4	38.5
Ethanol soln.[a]	-	-	-	-	37.3
Urea soln[a]	-	-	-	-	44.8

[a]Solubility parameter values of mixed solvent were calculated by using the equation described in Carvalho et al [85].

Table 3.7 Overview of the ESC experiments with different tested agents

Materials	Filler size (nm)	Filler content (vol.%)	ESC agents					
			Isopropanol	Methanol	Ethanol soln.	Urea soln.	Water	Air
PC-H	12	0/0.5/1/4	X	X	X	X	X	X
PC-L			X	X	X	-	X	X
PS			X	X	-	-	X	X
PMMA			-	-	-	-	X	X
PC-H	7	0/0.5/1/4	X	X	X	-	X	X
PC-L			X	X	X	-	X	X
PS			X	X	-	-	X	X
PMMA			-	-	-	-	X	X

3.8.3.2 Characterization of Environmental Stress Cracking

To determine the transient macro-crack length (da/dt), the macro-crack length was directly measured from the captured images, as shown in Figure 3.8. Although there is a large plastic deformation zone in front of the pre-crack, the mode I stress intensity factor (K_I) for a CT specimen was calculated using linear fracture mechanics, according to the following equation:

$$K_I = f(a/W) \cdot (F/BW^{1/2})$$ (3.14)

where a is the macro-crack length, F is the applied load, B and W represent the specimen dimensions (4 mm and 30 mm, respectively), and $f(a/W)$ is the calibration factor for CT specimens, which is given as equation 3.7.
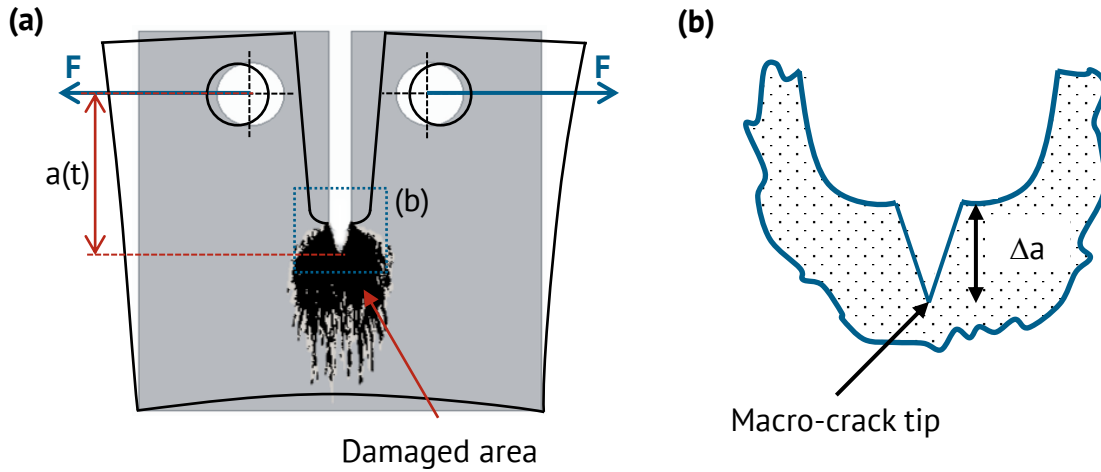
Figure 3.8: Characterization of deformed ESC test samples.

To determine the development of the damaged area, the saved images were analyzed using Matlab image processing software. The images were first converted to binary format and a threshold limit was then defined to distinguish objects of interest (damaged area) from the background, as illustrated in Figure 3.9. Finally, the damaged area was calculated from the pixel numbers.
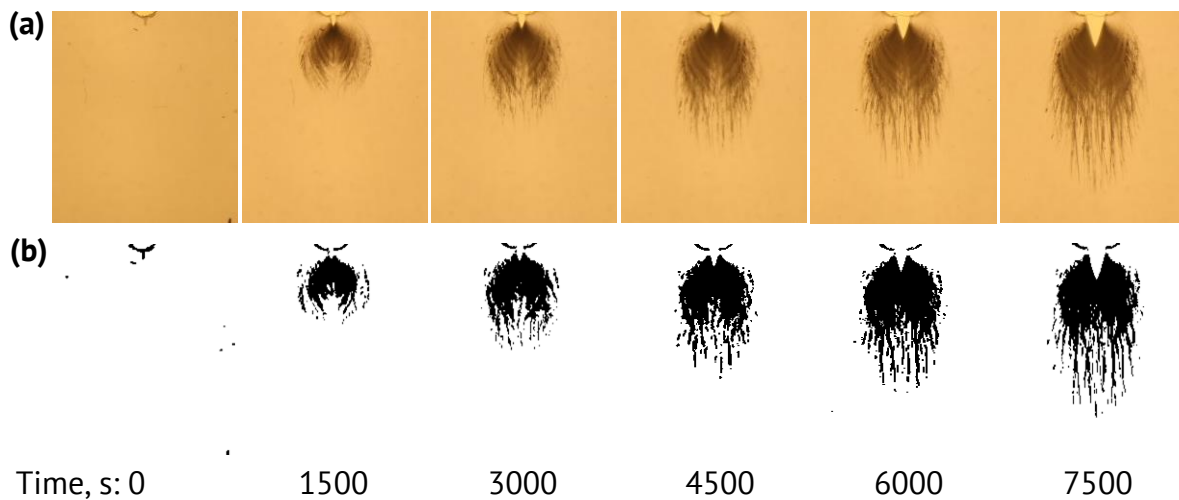
Figure 3.9: Development of the damage area size as a function of times of PC: (a) original images and (b) images in grey scale after processing with Matlab.

4   Results and Discussion

4.1   Polycarbonate Nanocomposites

4.1.1   Morphological Properties of Particle Dispersion

It is well known that the microstructure and the quality of the dispersion of nanofillers within the polymer matrix have a decisive influence on the performance of polymer nano-composites. High-resolution SEM images of fractured surfaces are therefore used to determine the dispersion quality of the nanoparticles in the polymer matrix, as shown in Figure 4.1. In general, particle aggregates/agglomerates are formed due to high rates of particle interaction (i.e. hydrogen bonding, van der Waals), and this increases the effective size of the filler. Accordingly, the SEM micrographs reveal small agglomerations of nano-SiO_2 particles in the form of white dots, which are uniformly distributed in the PC matrix.
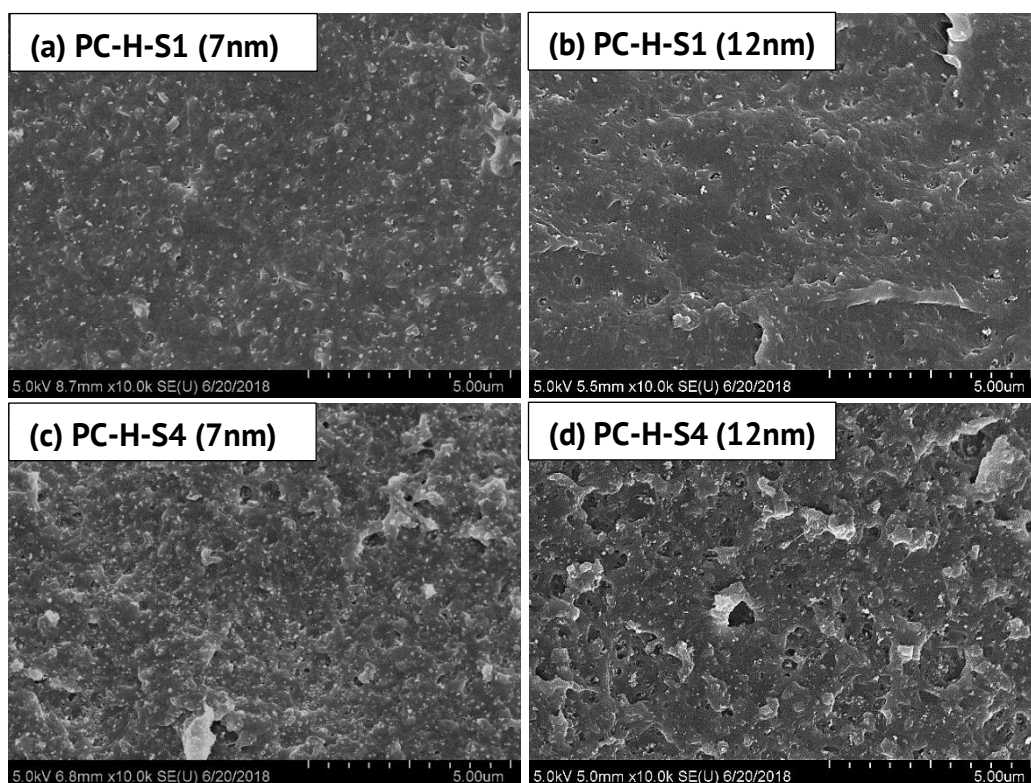
Figure 4.1: SEM micrographs of different materials: (a) and (c) PC filled with 1 and 4 vol.% nano-SiO_2 (7 nm), (b) and (d) PC filled with 1 and 4 vol.% nano-SiO_2 (12 nm).

Figure 4.2 shows the probability and cumulative of the equivalent agglomerate size distribution in the PC matrix. As can be seen from the diagrams and the accompanying table,

materials with 1 vol.% content of nano-SiO$_2$ particles have an average size of 30 nm. An increase in filler content shifts the curve to the right, giving a larger equivalent diameter of the agglomerates. Nanocomposites with 4 vol.% nano-SiO$_2$ contain more and larger nano-SiO$_2$ agglomerates with a mean diameter of 50 to 60 nm. The reason for this is that at high proportions of nanofiller content, filler–filler interactions predominate over the shearing force applied during the mixing process, making it difficult to disperse the agglomerates [42,86,87]. However, the agglomerated size does not change significantly when the primary particle size is reduced from 12 nm to 7 nm. Although small agglomerates can be observed, some individual nanoparticles are also distributed randomly throughout the entire polymer matrix, and this may increase the efficiency of transferring the intrinsic properties of the nanoparticles to the composite.
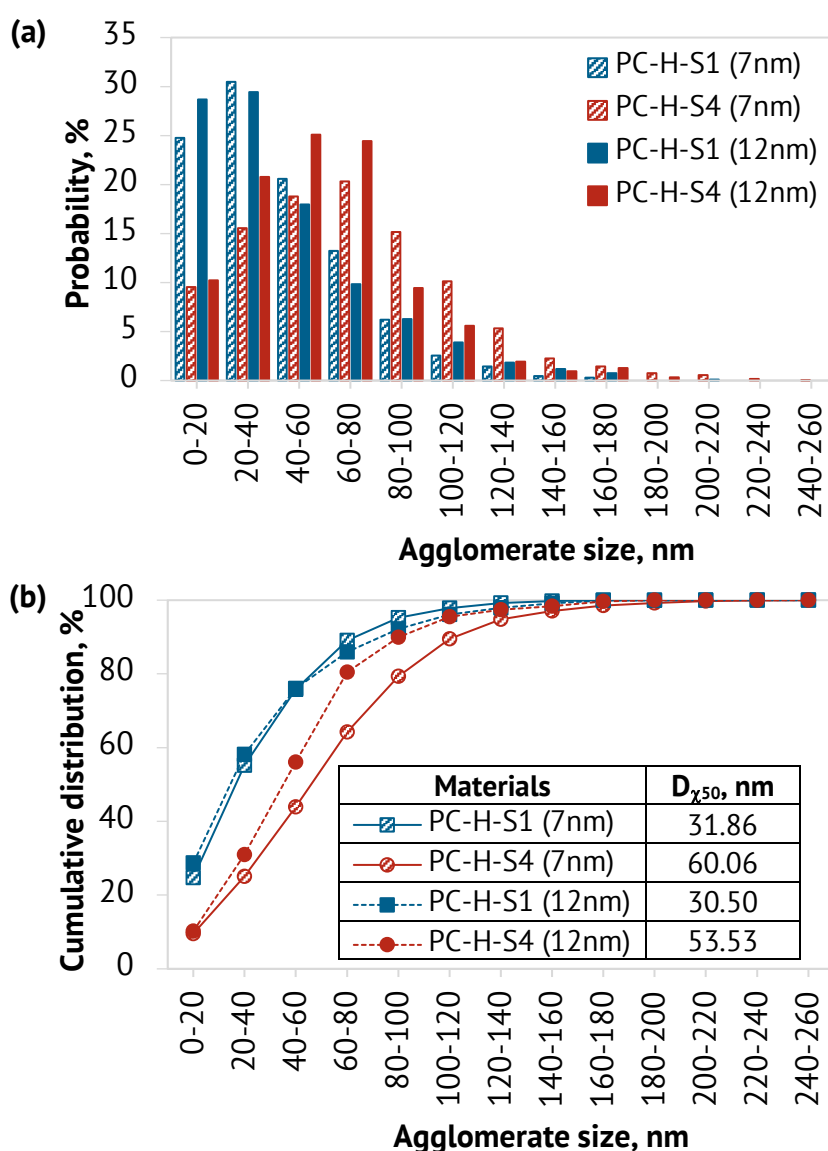
Figure 4.2: (a) Probability and (b) cumulative distribution of the equivalent agglomerate size of the PC nanocomposites.

4.1.2 Optical Properties

Transparency is one of the key properties of amorphous polymer, which is often used in applications that require glasslike clarity, such as in medical devices, optical fiber sensors, optical isolators and packaging products [83]. Representative images of PC nanocomposites containing different sizes and proportions of nano-SiO_2 particles are shown in Figure 4.3. All neat PC matrices used in this study are naturally transparent, while the nanocomposites are translucent but macroscopically homogeneous. Obviously, the polymer nanocomposites become hazy due to the incorporation of fillers, and this is proportional to the size and amount of nanofiller.

		Materials			
	PC	S1 (7nm)	S1 (12nm)	S4 (7nm)	S4 (12nm)
(a)					
(b)					
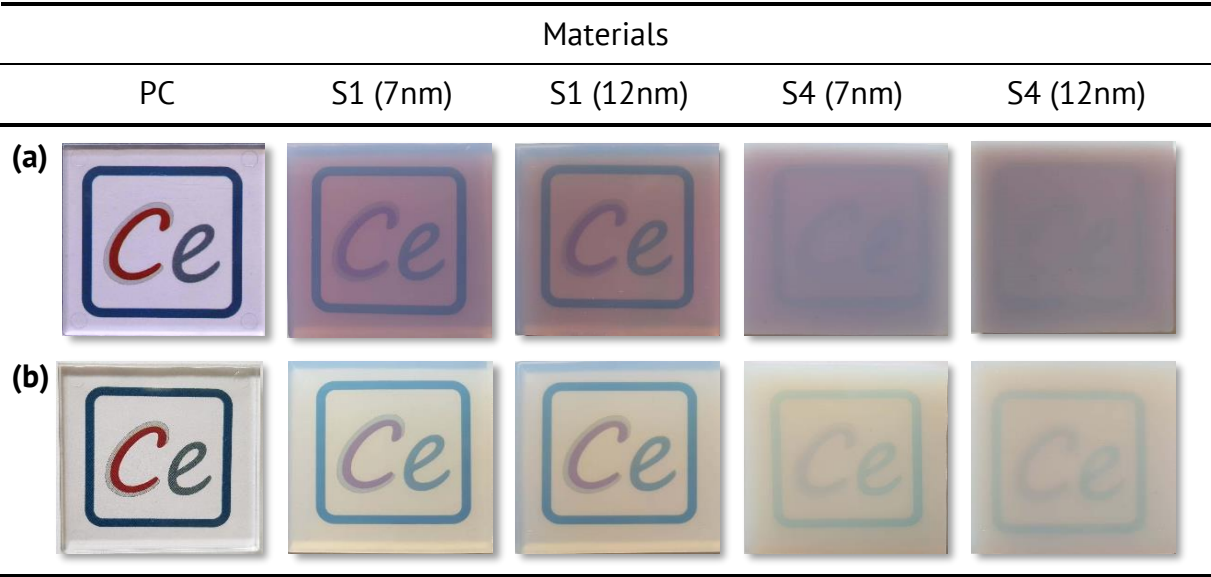
Figure 4.3: Representative images of PC nanocomposites: (a) PC-H and (b) PC-L containing nano-SiO_2 particles with different sizes and concentrations.

Figure 4.4 shows quantitative evaluations of the optical properties of the PC nanocomposites, which are characterized by total light transmittance, haze and clarity (Appendix A). Transmittance is defined as the fraction of incident light passing through a specimen, while clarity and haze are defined as the percentages of transmitted light with scattering angles between 0°–2.5° and 2.5°–90°, respectively, compared to the direction of the incident beam [83,88]. It can be clearly seen from Figure 4.4 that the total light transmittance of the PC nanocomposites decreases significantly with an increase in the nanoparticle content. The main reason for deterioration in the optical transparency of polymer nanocomposites is light loss due to reflection at the interface of the polymeric matrix and the particles. This reflection occurs due to the difference in the refractive indices between the two materials [83]. Simultaneously, an increase in the content of the nano-

SiO_2 particles results in a decrease in clarity and an increase in haze, due to light loss via reflection and scattering [83]. It is worth noting that polymers filled with smaller nano-SiO_2 particles have better optical properties, as indicated by the relatively high clarity and low haze for a given nano-SiO_2 content. This indicates that the small size of the particles is an important feature in avoiding light scattering, as it can provide highly transparent nanocomposites [89].

Figure 4.4: Optical properties of PC nanocomposites filled with nano-SiO_2 of 7 nm (dash line) and 12 nm (solid line): (a) total light transmittance, (b) clarity, and (c) haze as a function of particle contents.

4.1.3 Mechanical Properties

4.1.3.1 Tensile Properties

The mechanical behavior of the PC matrices in the tensile test, as represented by engineering stress-strain curves, is illustrated in Figure 4.5(a). At the beginning of the 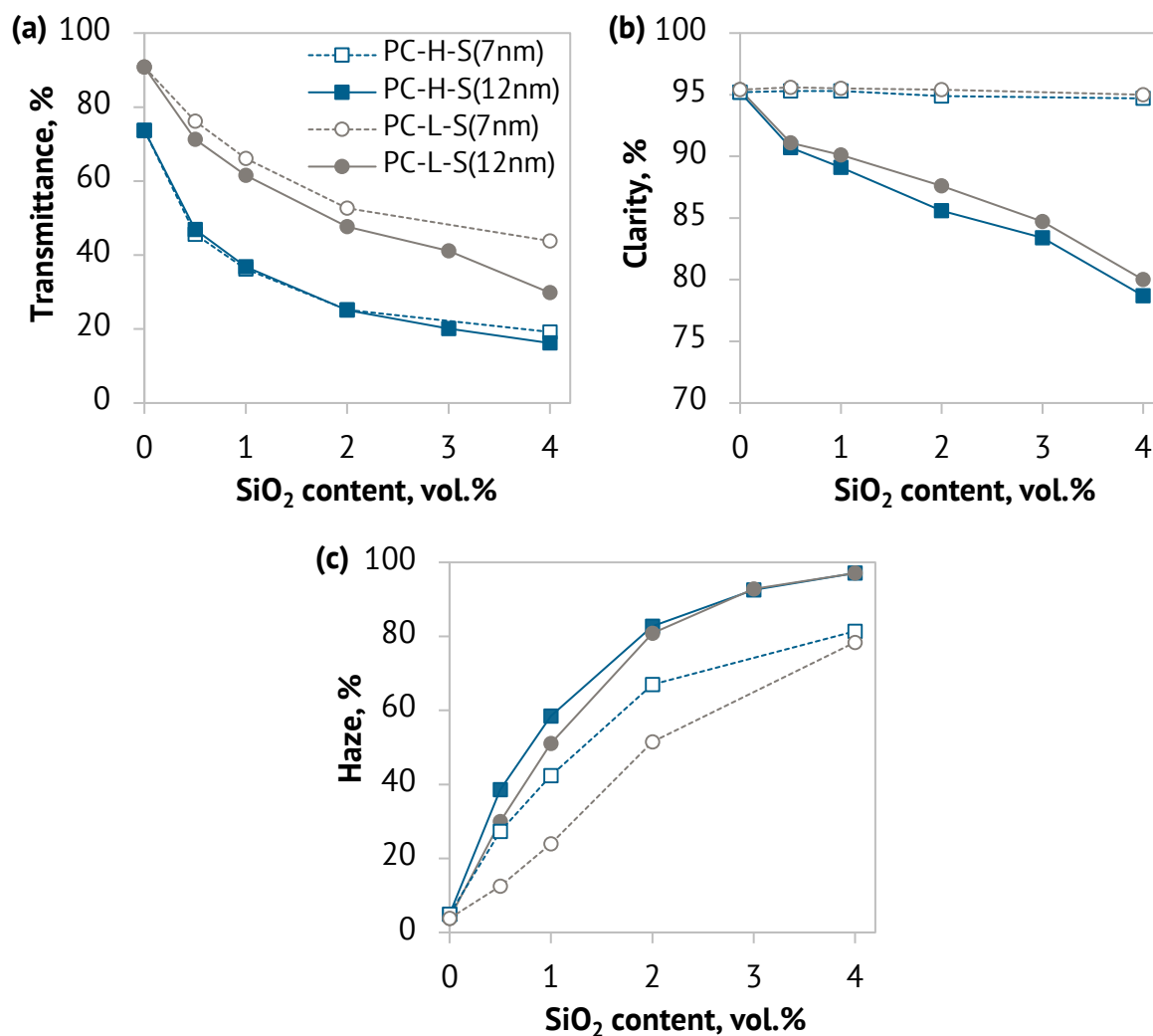deformation process, the material behaves in a linear elastic and viscoelastic manner, followed by a plastic deformation region and finally fracture. The PC-H has a much higher plasticity than the PC-L, and this can be observed experimentally as a strain-hardening response during large strain plastic deformation [90].

The Young's modulus, tensile strength and elongation at break for the PC nanocomposites are depicted in Figures 4.5(b), (c) and (d), respectively (Appendix B and C). As expected, and as already demonstrated in other materials [91], the addition of nano-SiO_2 particles results in an improvement in the elastic modulus of PC nanocomposites. The increase in the rigidity of the polymer nanocomposites can be explained by the partial substitution of soft matrix with stiffer filler, and is also related to the segmental immobilization caused by the rigid interphase between filler and polymer matrix [29,92]. Figure 4.5(c) shows an increase in the tensile strength with the incorporation of a small amount of nano-SiO_2 (0.5–1 vol.%). This indicates that a very large surface area of nanofiller provides a high number of interactions at the filler-matrix interfacial area, and these are responsible for the more efficient transfer of stress across the nanocomposite components [4,14–16]. However, with a further increase in the nanofiller contents beyond 1 vol.%, the improvements are only marginal. In terms of the elongation at break, the PC-based nanocomposites show an enhancement in the elongation with the addition of a small proportion of nano-SiO_2 as can be seen in Figure 4.5(d).

Interestingly, it is apparent that the tensile properties of the PC nanocomposites markedly improve with the presence of smaller nano-SiO_2 particles (7 nm), especially at low filler contents. This result confirms that the specific surface area of the nanofiller plays a significant role in the improvement in the tensile properties. A smaller nanofiller particle has a larger interface area, which increases the degree of interfacial interaction and is more efficient in dissipating energy at the interface between the nano-SiO_2 and the polymer matrix, thus improving the tensile properties of the polymer nanocomposite [16].
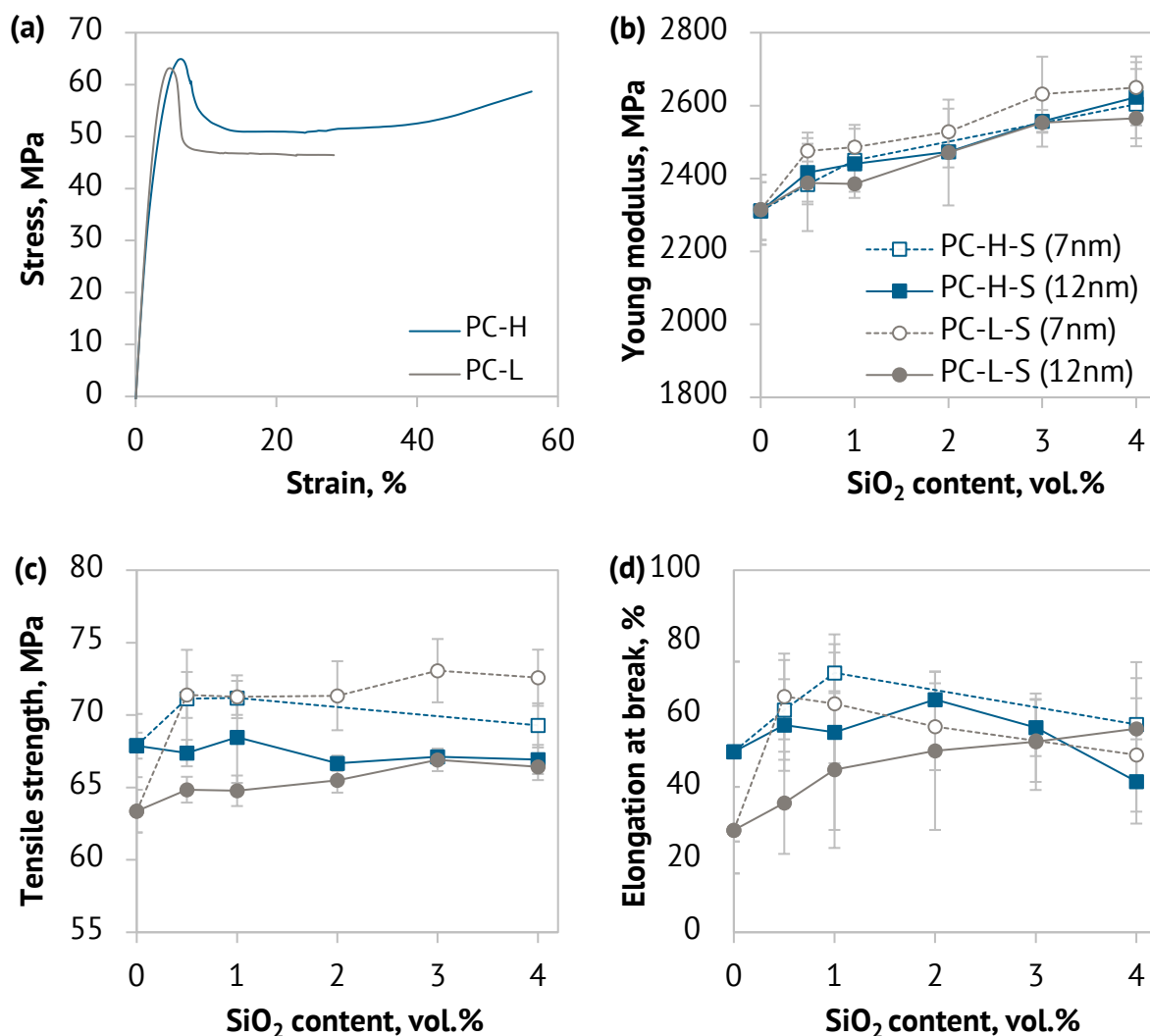
Figure 4.5: Tensile properties of PC nanocomposites as a function of the filler contents and its particle sizes: (a) representative stress-strain curve of PC matrices, (b) Young's modulus, (c) tensile strength, and (d) elongation at break.

4.1.3.2 Impact Properties

Figure 4.6(b) shows representative load-displacement curves for neat PC and PC filled with 1 vol.% of nano-SiO_2, obtained from a Charpy impact test. It can be seen that the PC nanocomposite filled with smaller particles (7 nm) exhibits the highest load maximum and displacement. It is well known that the area under the load-displacement diagram represents the total deformation energy (A_{tot}). By using the approximate method of Schindler [93,94], total deformation energy can be divided into an elastic component (A_{el}), a plastic component (A_{pl}) and a crack propagation energy component (A_R). Thus, the influence of the nanofiller on the crack resistance behavior of polymer nanocomposites can be estimated from its load-deflection diagram, as shown in Figure 4.6(a).

The effects of the nano-filler contents and the particle sizes on the notched impact strength and the corresponding deformation energies of PC-based nanocomposites are shown in Figures 4.6(c) and (d) (Appendix B and C). It is apparent that the deformation energy and the notched impact strength noticeably improve with the presence of nano-SiO_2, especially for smaller particles. The enhancement in the cracking resistance induced by the nanoparticles is responsible for the outstanding improvement in the toughness of the PC-based nanocomposites. In this case, it should be noted that only the specimens of PC nanocomposites with a filler content of up to 1 vol.% and a particle size of 12 nm are completely broken. In contrast, for PC-based nanocomposites filled with more than 1 vol.% of nano-SiO_2 and with smaller particle sizes, the material shows some crack propagation, but only partially breaks. This result confirms that the energy is dissipated at the interface between nano-SiO_2 and the polymer matrix, resulting in a higher toughness of the nanocomposite. This is particularly true for the smaller nano-SiO_2 particles, which have a higher interfacial surface area, thus assuring a more effective energy dissipation at the interface.

A comparison of different molecular weight PC nanocomposites clearly depicts that the impact properties of PC-H is significantly enhanced at very low nano-SiO_2 content as in 0.5 vol.%, whereas the PC-L based nanocomposite still behaves as a brittle material at a given filler content. Therefore, it can be suggested that the transition point of the material properties from brittle to tough, induced by nanoparticles, also depends on the nature of the toughness of the polymer matrix, which is reflected by its molecular weight.
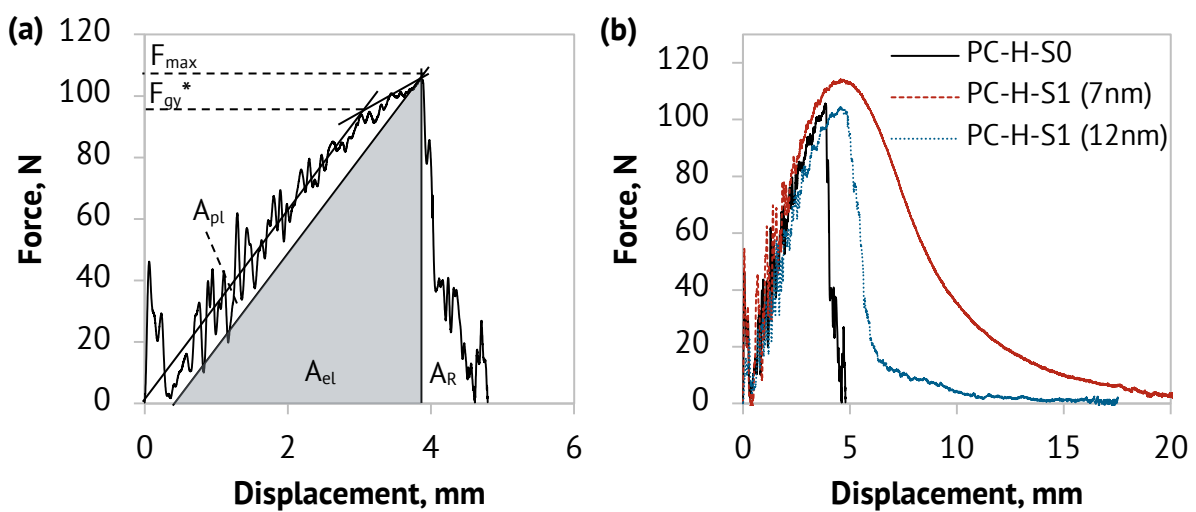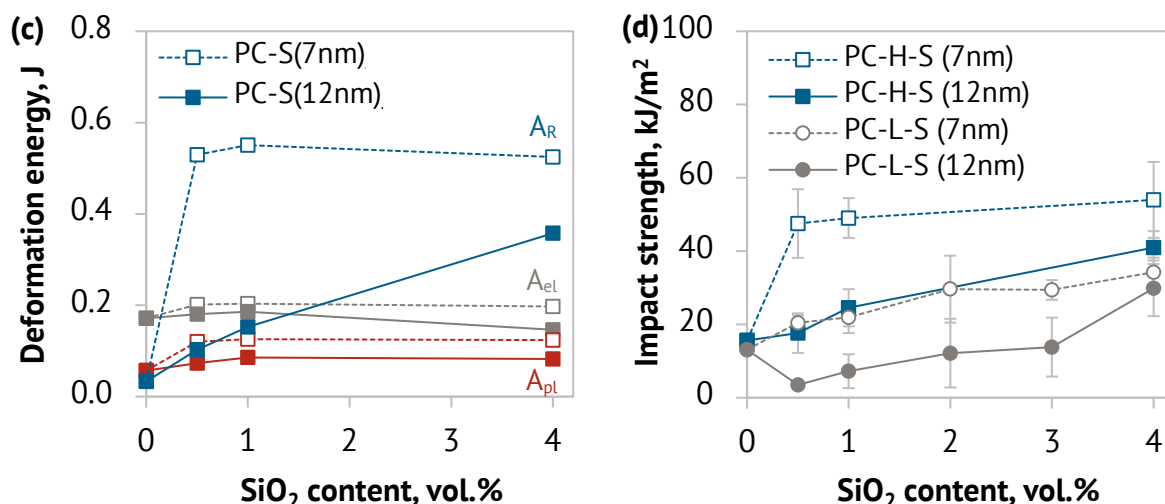
Figure 4.6: Impact properties of PC nanocomposites: (a) typical load-deflection diagram for elastic-plastic material behavior, (b) load-displacement curve of PC-H and PC-H/SiO$_2$ nanocomposites, (c) deformation energy of PC-H nanocomposites, and (d) notched impact strength of PC nanocomposites. (*F$_{gy}$ is the characteristic load value corresponding to the transit from elastic to elastic-plastic material behavior).

4.1.3.3 Fracture Toughness Properties

The representative load-displacement curves for neat PC matrices obtained from the fracture toughness tests (Mode I–Tension) is illustrated in Figure 4.7(a). It can be seen that the PC-H shows much higher load maximum and displacement compared with the PC-L, indicating the higher energy required for crack initiation and propagation which accounts for the higher fracture toughness of the material.

The critical fracture toughness (K$_{Ic}$) of PC nanocomposites which is evaluated from the load-displacement curve, is presented in Figure 4.7(b) (Appendix B and C). Similarly to the impact properties, a clear increase in the K$_{Ic}$ at low nanoparticle concentrations (0.5−1 vol.%) can be distinguished for the PC nanocomposites. A further increase in the nano-SiO$_2$ content more than 1 vol.% does not lead to a significant improvement in fracture toughness. Obviously, the K$_{Ic}$ of PC nanocomposites noticeably improves with the incorporation of smaller nano-SiO$_2$ particles. As is well known, smaller nano-SiO$_2$ particles provide a larger surface area for strong interfacial interaction between the nanofiller and polymer matrix, thus improving the toughness properties of the polymer nanocomposites [16].
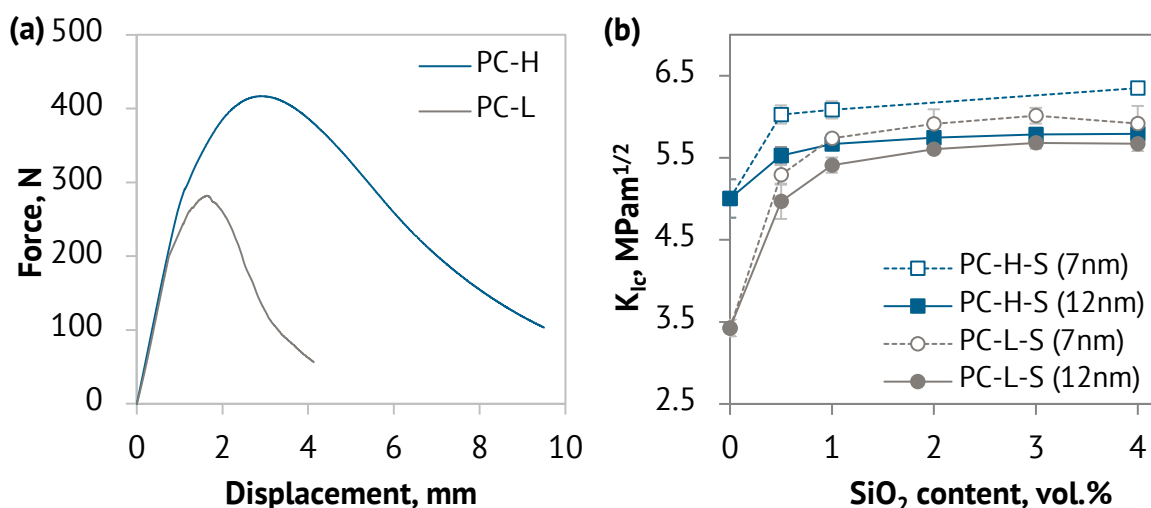
Figure 4.7: Fracture toughness of PC nanocomposites as a function of the filler contents and its particle sizes: (a) load-displacement curve of PC matrices and (b) K_{Ic}.

4.1.4   Thermal Properties

For amorphous polymer, the glass transition temperature (T_g) is an important characteristic that determines its suitability for a particular engineering application. The DSC thermograms of neat PC matrices in the temperature range from room temperature to 250°C is shown in Figures 4.8(a). The PC which has rigid backbones exhibits a high value of T_g (~145°C). Generally, in amorphous polymer nanocomposites, the change in T_g depends on the nanoparticle content and the degree of filler-matrix interaction at the interface [45]. Figure 4.8(b) shows the values of T_g for the PC-based nanocomposites with different nanofiller sizes and contents (Appendix D). It has been noted that the T_g increases by a few degrees with an increase nano-SiO_2 content, because the high degree of intermolecular interaction between the nanofiller and the polymer matrix restrains the freedom of motion of the chain segment in the polymer matrix, resulting in a slight increase of T_g [45,95]. However, the nanoparticle size does not have a significant effect on the T_g of PC.
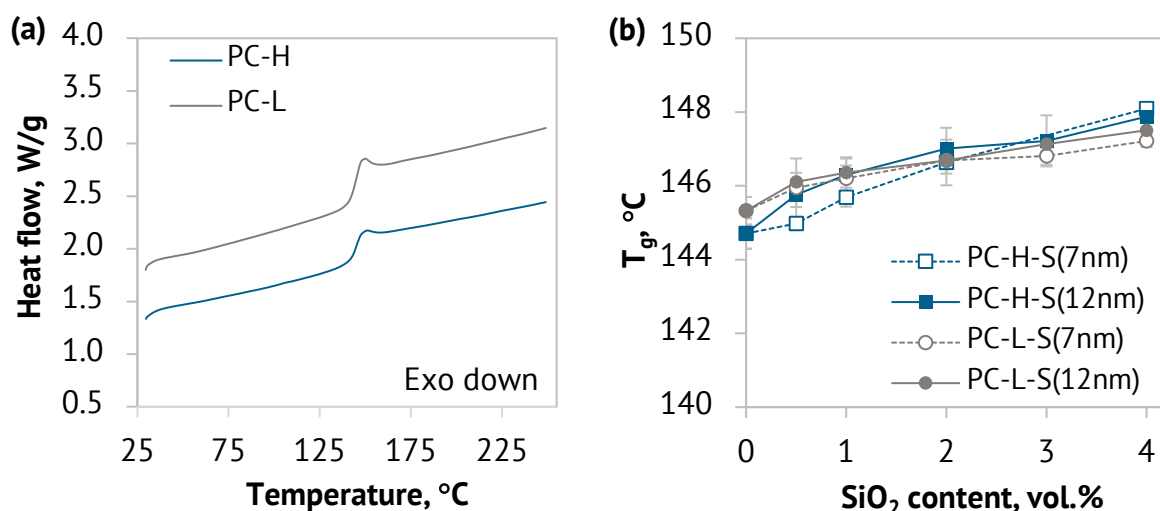
Figure 4.8: (a) DSC thermograms of PC matrices and (b) T_g of PC-based nanocomposites.

4.1.5   Environmental Stress Cracking Properties

It is well-known that fluid diffusion is an important parameter in the environmental stress cracking (ESC) resistance behavior of polymers. The diffusion rate of small molecules into a polymer depends on both the polymer and diffusant factors such as the morphological structure of the polymer, the molecular size of the diffusant, the degree of polymer-solvent compatibility, and the surface or interfacial energies of the polymer [58,59]. Once the fluid has penetrated into the polymer structure, it becomes locally plasticized, promoting craze initiation and crack extension in the polymer. Thus, the diffusion rates and surface wettability of the different ESC agents in the PC were previously determined by absorption and contact angle measurements, respectively. This characterization may promote a better understanding of the environmental effects on the failure properties.

4.1.5.1 Absorption Properties

The absorption behavior of the PC-based nanocomposites immersed in the ESC agents used in this study (isopropanol, DI water and methanol) is shown in Figure 4.9. Based on this absorption result, the diffusion coefficients for the different agents in the PC were then determined, as explained in section 3.8.1. It can be observed from Figure 4.10 and Table 4.1 that DI water has the highest diffusion coefficient, implying the fastest diffusion rate, followed by methanol and isopropanol. This observation indicates that the penetration rates are strongly dependent on the molar volume of the ESC agents [58,96]. DI water, which has a smaller molecular size (18 cm³/mol), penetrates much faster than methanol (40.7 cm³/mol) and isopropanol (76.8 cm³/mol).

However, craze/crack formation in a polymer not only depends on the diffusion coefficient, but also relates to the degree of interaction between the polymer and the agents, which can be predicted by solubility parameters. When there are only small differences between the solubility parameters of the agent and polymer, the agent will have a significant effect on crack formation, due to the higher chemical and structural compatibility. With respect to both the diffusion rate and the solubility effect, methanol is considered to be the strongest agent for macroscopic brittle crack formation, as it has low molar volume and solubility parameters that are closer to those of PC. Therefore, methanol can support the highest degree of absorption, as indicated in Figure 4.9(a). Although DI water has the fastest rate of diffusion into PC, but a large different in the solubility parameter may have only small effect on crack formation.
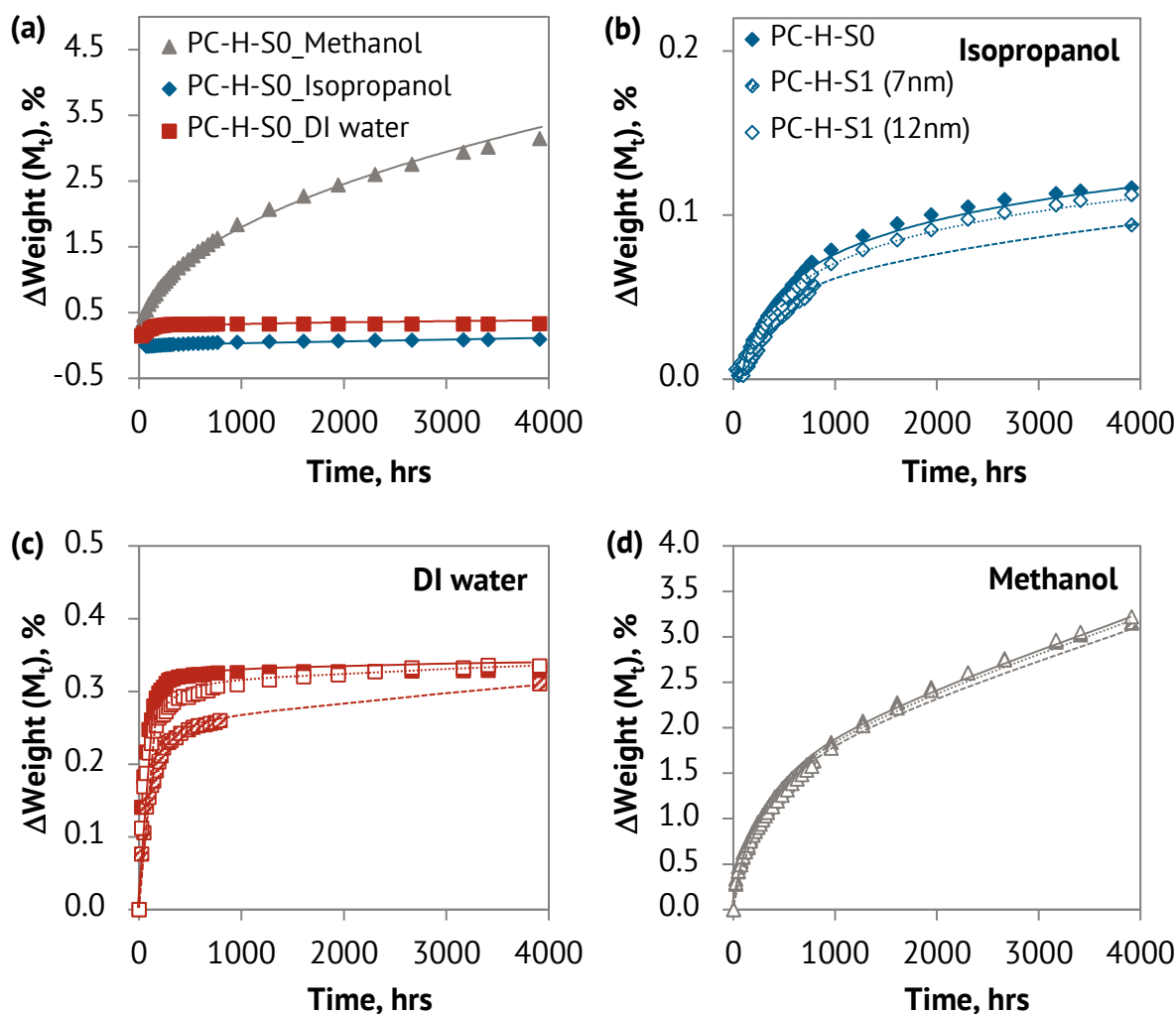
Figure 4.9: (a) Weight change of PC in different agents and (b)–(c) absorption behavior of PC-based nanocomposites in isopropanol, DI water and methanol, respectively.

Interestingly, the addition of nano-SiO$_2$ decreases the absorption rate of all agents into the PC, as indicated by a decrease in the diffusion coefficient, especially in smaller nano-SiO$_2$ particles, as seen in Figure 4.10. In general, the nanofillers can either act as impermeable obstacles rendering the liquid/gas molecules pathways more tortuous (referred as tortuosity) or to increase the free volume at the interfaces and the interstitial regions within the agglomerates, thus accelerating the absorption process into the materials [97,98]. Each of these factors has an opposite effect on the absorption behavior. Thus, the decrease in the diffusion coefficient indicates that the tortuosity is the dominant factor. The uniform dispersion of the nano-SiO$_2$ at the nanometer scale in the PC matrix can increase the mean path length for liquid molecules passing through a huge number of barrier particles during mass transfer, leading to a reduction in the absorption rate [59,99]. A schematic illustration of the diffusion path through a homogeneous polymer structure and a heterogeneous polymer structure such as a nanocomposite is given in Figure 4.11.

Concerning the effect of the molecular weight of the PC, it can be seen that the lower molecular weight PC can absorb the liquid molecules more readily than the high molecular weight PC. Thus, the diffusion coefficient changes inversely with the molecular weight of the PC, as seen in Figure 4.10(b). This phenomenon suggests that polymers with high molecular weight have a tendency to reduce the diffusion rate of the agent, due to the increase in path length arising from the higher degree of polymer chain entanglement, which can retard process of craze and crack formation during the ESC failure.
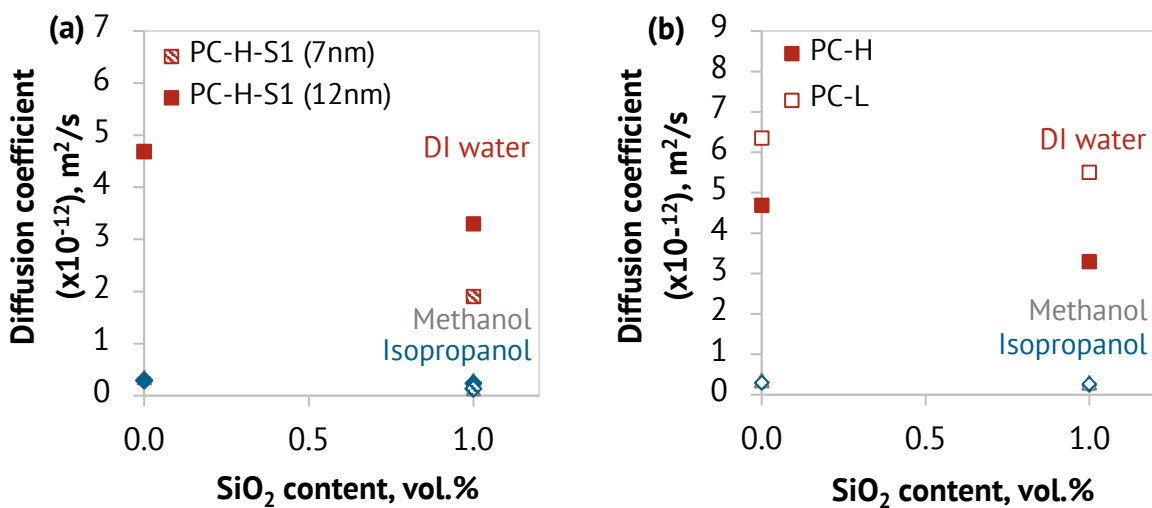
Figure 4.10: Diffusion coefficient of PC-based nanocomposites in different agents: (a) influence of nano-SiO$_2$ and its size and (b) effect of molecular weight of PC.

Table 4.1: Diffusion coefficient of PC-based nanocomposites in different agents

Materials	Diffusion coefficient (D), m^2/s		
	DI water	Methanol	Isopropanol
PC-H	4.68×10^{-12}	0.35×10^{-12}	0.29×10^{-12}
PC-H-S1 (7nm)	1.90×10^{-12}	0.13×10^{-12}	0.13×10^{-12}
PC-H-S1 (12nm)	3.29×10^{-12}	0.29×10^{-12}	0.23×10^{-12}
PC-L	6.35×10^{-12}	0.36×10^{-12}	0.30×10^{-12}
PC-L-S1 (12nm)	5.50×10^{-12}	0.30×10^{-12}	0.27×10^{-12}

Note: Total solubility parameter of PC is 21.5 MPa$^{1/2}$ [47].
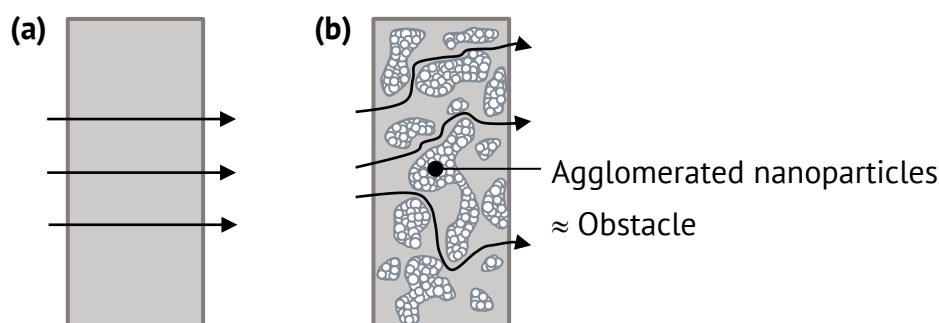
Figure 4.11: Schematic demonstration of diffusion path through a structure: (a) homogeneous and (b) heterogeneous medium (adapted from reference [59]).

4.1.5.2 Surface Wetting Properties

It is generally agreed that a reduction in surface energy due to contact/wetting with chemical agents appears to be an important parameter in accelerating the formation process of crazing and cracking. The wettability of fluid droplets (l) on a solid polymer surface (s) is often described in terms of contact angles (θ) and interfacial tension (γ_{sl}) at the liquid-solid interface. Wetting is favored by a low interfacial free energy at the liquid-solid surface, a high solid surface energy and a low liquid surface free energy or surface tension.

Figure 4.12 shows the contact angle of polymer nanocomposites in contact with different ESC agents (Appendix E and F). It is apparent that the wetting of the surface of the PC-based nanocomposites is more favorable in alcohol agents than DI water, as indicated by lower contact angle. The agents with low surface tension (i.e., isopropanol and methanol) are readily spread over the polymer surface, reflecting the similarity in the energy properties of the liquid and the solid surface, and this may accelerate crazing and cracking in

the ESC process [100]. This result shows very good agreement with the previous results for absorption behavior. An increasing the nano-SiO_2 content and decreasing the nano-filler size causes a slight increase in wettability. Similarly to the absorption test, the wettability is reduced when the polymer has a higher degree of chain entanglement, as in the PC-H. The correlation of the interfacial tension (γ_{sl}) at the liquid-solid interface with the Hansen solubility parameter confirms that the wettability is mainly dependent on the difference between solubility parameters of the polymer and the fluid, as can be seen from Figure 4.12(c).

Figure 4.12: Contact angle of PC nanocomposites in different agents: (a) PC-H, (b) PC-L and (c) interfacial tension of PC nanocomposites as a function of the solubility parameter of different ESC agents.

4.1.5.3 Effect of Nanofiller Content

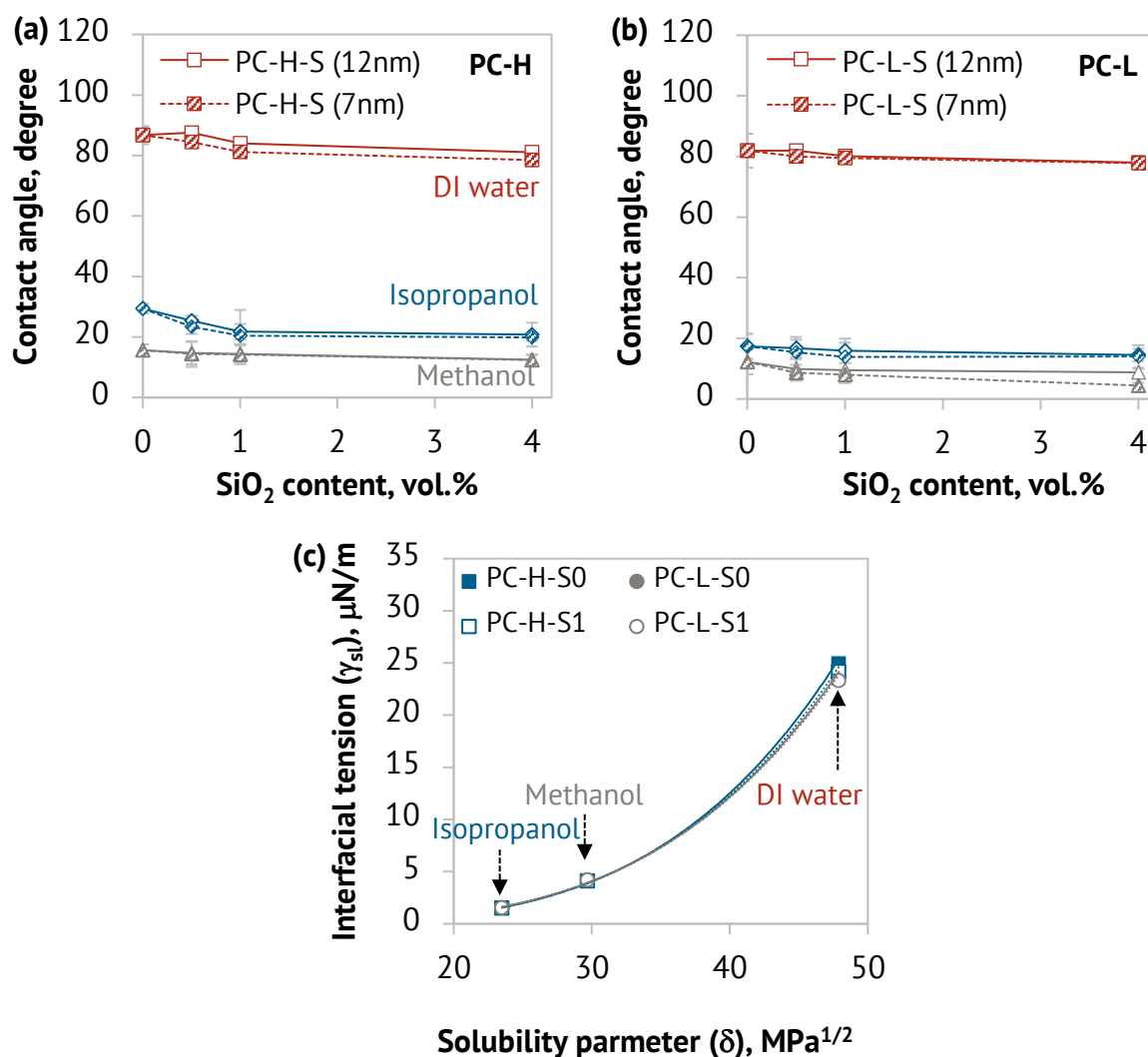As already demonstrated, the incorporation of nanoparticles gives an improvement in the mechanical properties, due to the high levels of filler-matrix interfacial interaction that contribute to effective energy dissipation at the interface. This approach is therefore also applied to enhance the ESC resistance of amorphous-based materials to open up novel opportunities for the materials in various application fields. In the current work, the ESC behavior of PC-based nanocomposites was investigated in different testing agents using a fracture mechanic test method with online optical crack detection, as described in section 3.8.3.

ESC Properties

The development of the macro-crack length and the size of the damaged area as a function of time for PC-based nanocomposites in isopropanol, are shown in Figures 4.13(a) and (b), respectively. The entire process of crack propagation of neat PC and PC nanocomposites can be divided into three phases: crack initiation, crack propagation, and final catastrophic failure, which is follow a typical deformation behavior for polymers. In the primary phase, i.e. the early stage of loading, the size of the damaged area increases rapidly with time. Then, it grows linearly as a function of time in stable phase, and the first macro-crack also becomes visible in this phase. Following this, the size of the damaged area and the length of the macro-crack again increase rapidly with time in the final failure phase. This situation marks the beginning of unstable growth of the damaged area, and the sample consequently fractures within a short period of time. The relationship between the macro-crack length and the size of the damaged area is shown in Figure 4.14(a). It can be observed that the damaged area develops quickly in the early stages and then grows in linear proportion to the macro-crack length. Thus, the macro-crack length can be also assessed based on the corresponding size of the damaged area in this steady state [6].

It can be clearly observed that the growth rate of the damaged area in the PC significantly decreases with the presence of nano-SiO_2 particles, and this is indicated by the reduction in the slope of the curve in the stable crack growth region, as shown in Figure 4.14(b). This result is also related to the slower onset period of unstable damaged area propagation, which is determined from the intersection of the extrapolation line between the stable growth and the catastrophic growth of the damaged area, as shown in Figure 4.13(b). Thus, it can be stated that the addition of nano-SiO_2 particles to PC leads to

slower crack growth and thereby significantly increases the ESC resistance and service lifetime of PC-based nanocomposites, as seen in Figure 4.14(d).
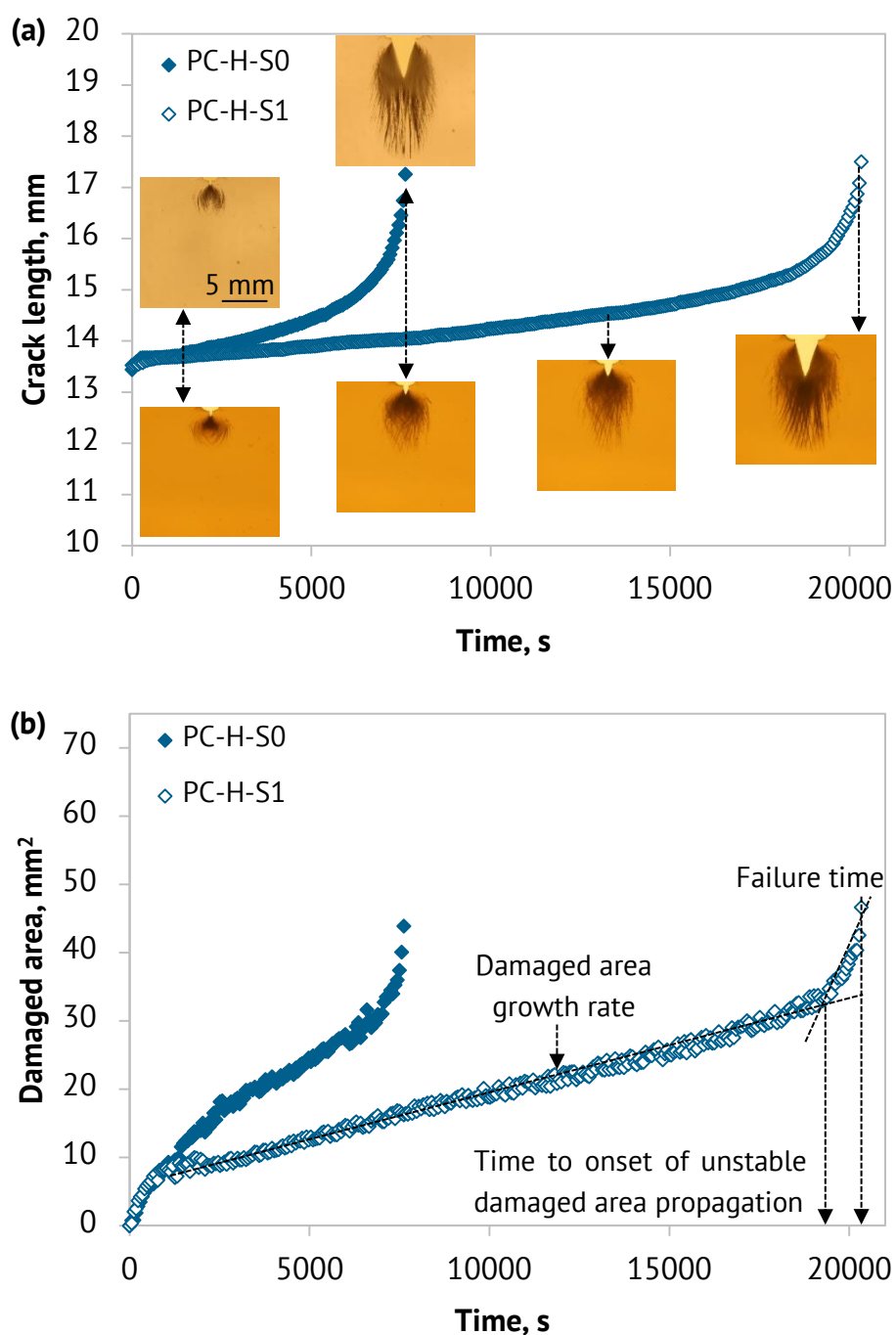
Figure 4.13: (a) Macro-crack length and (b) size of damaged area propagation as a function of time (in isopropanol) of PC and PC filled nano-SiO_2 1 vol.%.
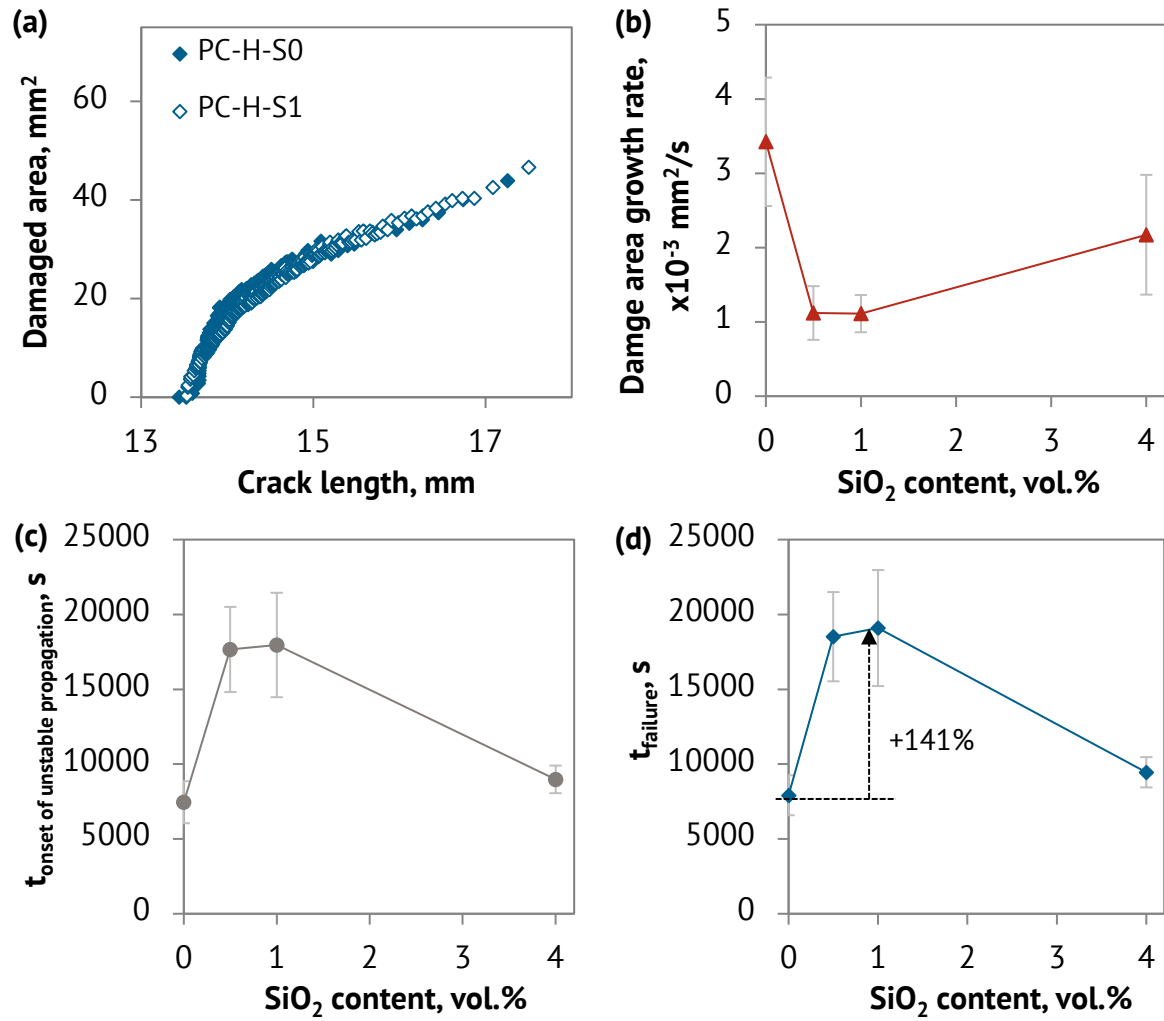
Figure 4.14: (a) Relationship between damaged area and macro-crack length of PC nano-composites, (b) damage area growth rate, (c) time to onset of unstable damaged area propagation and (d) failure time of PC with different SiO_2 contents in isopropanol.

By using the constant mechanical loading method, the relationship between the macro-crack propagation rate (da/dt) and the stress intensity factor (K_I) in the stable phase can be described by the Paris–Erdogan law, as follows:

$$da/dt = AK^m \qquad (4.1)$$

where A and m are constants that depend on the material performance and the testing conditions [5,6].

The influence of nano-SiO_2 content on the macro-crack propagation rate as a function of the K_I factor and the crack growth threshold (K_{Ith}), the critical stress intensity factor (K_{Ic}) and the slope in the stable crack growth region of PC-based nanocomposites in isopro-

panol are presented in Figures 4.15(a) and (b), respectively. It can be seen that the material behavior follows the well-known principle that divides the crack growth as a function of the stress intensity factor into three phases: crack initiation, crack propagation and final failure. The incorporation of nanoparticles into PC increases the values of K_{Ith} and K_{Ic}, as well as reduces the crack propagation rate, indicating an improvement in ESC resistance. The PC nanocomposite with 1 vol.% of nano-SiO_2 particles exhibits the largest improvement in ESC resistance, and slight decrease is seen with 4 vol.% of nano-SiO_2 due to the formation of some larger agglomerates, which act as stress raisers and weak interfacial interactions [101,102]. This explanation can be substantiated by considering the SEM micrographs in Figure 4.21(d), which reveal more and larger agglomerates in the PC nanocomposite filled with 4 vol.% nano-SiO_2.
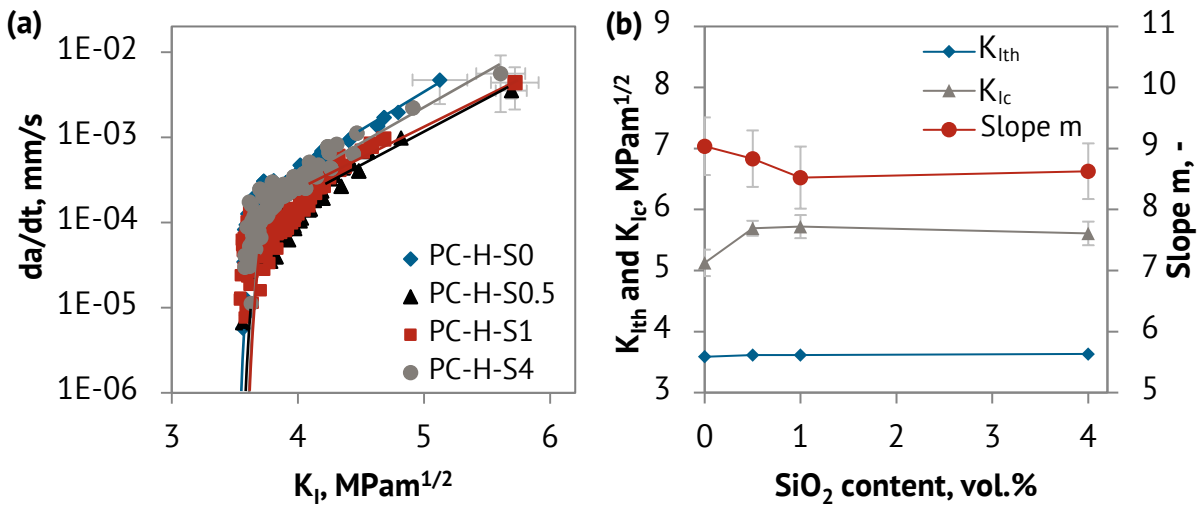
Figure 4.15: (a) Macro-crack propagation rate as a function of K_I factor and (b) K_{Ith}, K_{Ic}, and slope of curve as a function of nanoparticle contents in isopropanol.

As mentioned earlier, the ESC behavior of SiO_2-filled PC was investigated in several fluids (for which the solubility parameter varied from ~23 to 48 $MPa^{1/2}$) in order to correlate the ESC behavior of the PC-based nanocomposites with the stress-cracking agent properties using the Hansen solubility parameter and the molar volumes of the ESC agents. Figure 4.16 presents digital images of the development of the damaged area in PC and PC/SiO_2 nanocomposites at the same testing times in isopropanol, methanol, ethanol solution, DI water and air. In the two-dimensional optical micrographs, the crack growth appears as color (density) changes in front of the advancing ridge tip. Different types of area in front of the macro-crack tip can be observed in different agents, thus indicating different fracture mechanisms. The deformation area develops in two directions, in a similar way to the "candle flame" pattern observed in isopropanol and ethanol solution but on a smaller

scale. The appearance of this shape can be explained on the basis of crack-layer theory [6,103,104]. In methanol, three major directions of spreading of intense crazing are seen around the crack-tip. In contrast, a small wedge-like deformation surrounding the crack-tip is observed if the neat PC is exposed to mild agents such as DI water, aqueous urea solution [8] or air. More importantly, this deformed pattern in mild agents and air is significantly changed in the presence of nano-SiO_2. A much more voluminous damaged area appears in front of the crack tip, implying a different quality of the deformation processes in the materials, whereas this does not occur in the alcohol agents. One can see that the PC nanocomposites show a much smaller damaged area than in neat PC at the same testing times. This result confirms that the addition of nano-SiO_2 particles to PC leads to a slower growth rate of the damaged area in all investigated ESC agents.

Materials	PC	PC/SiO_2 1 vol.% (12nm)
Isopropanol		
Methanol		
Ethanol solution		
DI water		
Air		5 mm
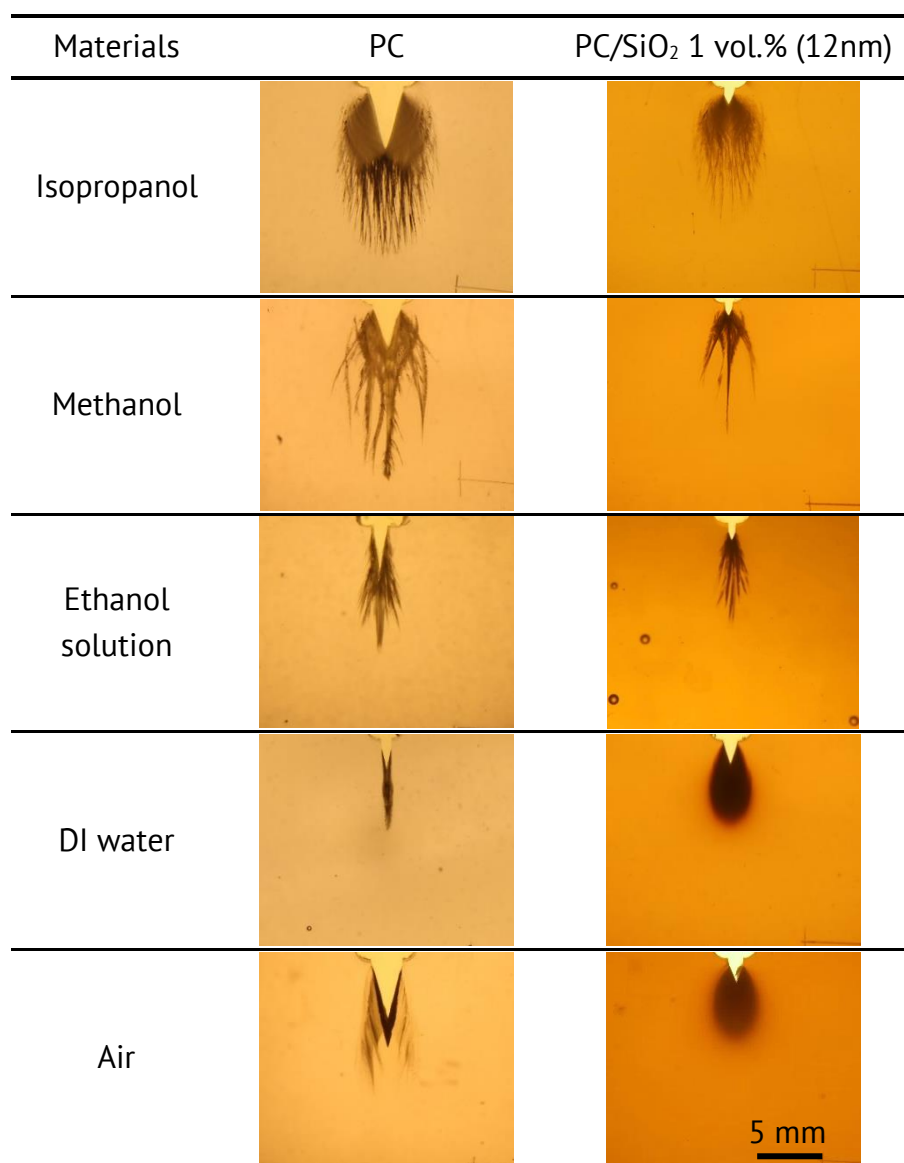
Figure 4.16: Digital images of ESC behavior in different ESC agents of PC and PC/SiO_2 nanocomposites at the same testing time.

The effect of the nano-SiO_2 on the macro-crack propagation rate as a function of the K_I factor of the PC in different ESC agents is shown in Figure 4.17, and the average values of K_{Ith}, K_{Ic} and slope in the stable crack growth region in different materials are shown in Figure 4.18(a), (b) and (c), respectively (Appendix G). It can be seen that the addition of nanoparticles to PC is effective in greatly increasing the ESC resistance of the materials in all investigated fluids. It can be clearly observed in Figure 4.17 that there is a significant improvement in the K_{Ith} and K_{Ic} and a reduction in the crack propagation rate with the presence of nano-SiO_2, especially in mild agents (i.e. DI water and urea solution) and air, where the type/shape of the area in front of the macro-crack tip is greatly changed. These results demonstrate that the incorporation of nano-SiO_2 particles into PC shifts the crack growth initiation and leads to slower crack growth as well as prolongs the onset period of catastrophic crack propagation. As a result, the ESC resistance of PC-based nanocomposites is significantly enhanced [6,8]. It is also interesting to note that a significant improvement in the ESC resistance of the PC is achieved simply by the incorporation of a low concentration (0.5–1 vol.%) of nano-SiO_2 particles, as shown in Figure 4.18.
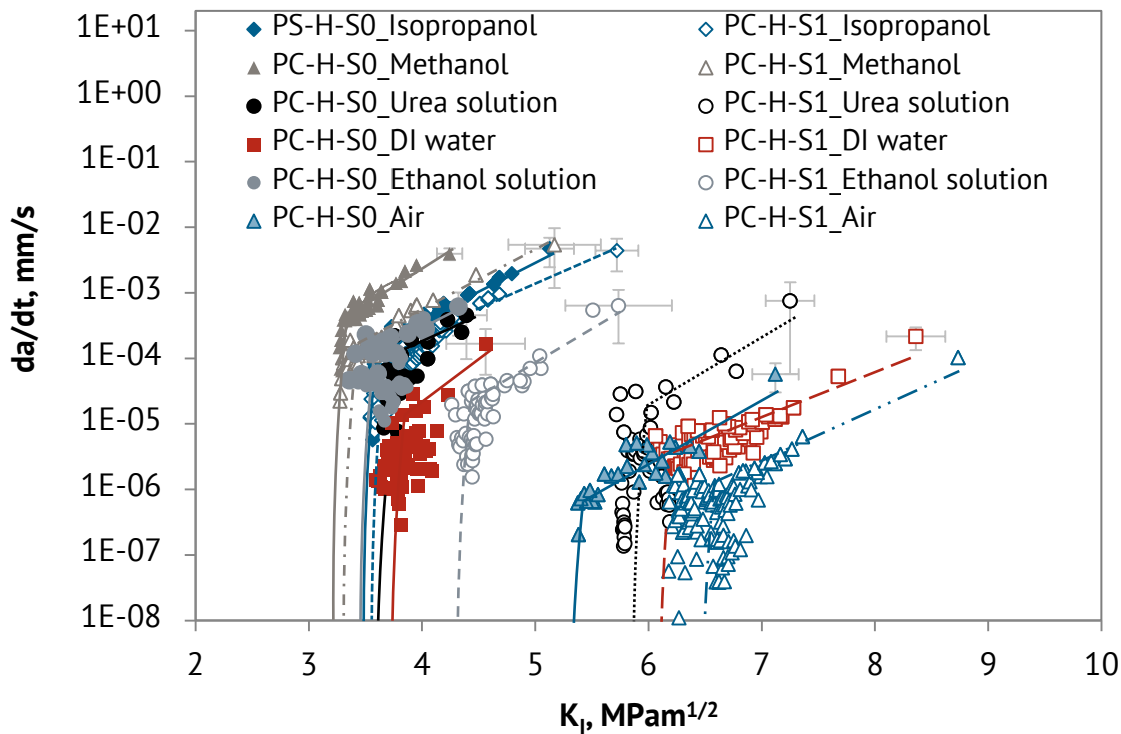
Figure 4.17: Macro-crack propagation rate as a function of the K_I factor for neat PC and PC filled with 1 vol.% of nano-SiO_2 (primary particle size 12nm) in different ESC agents.
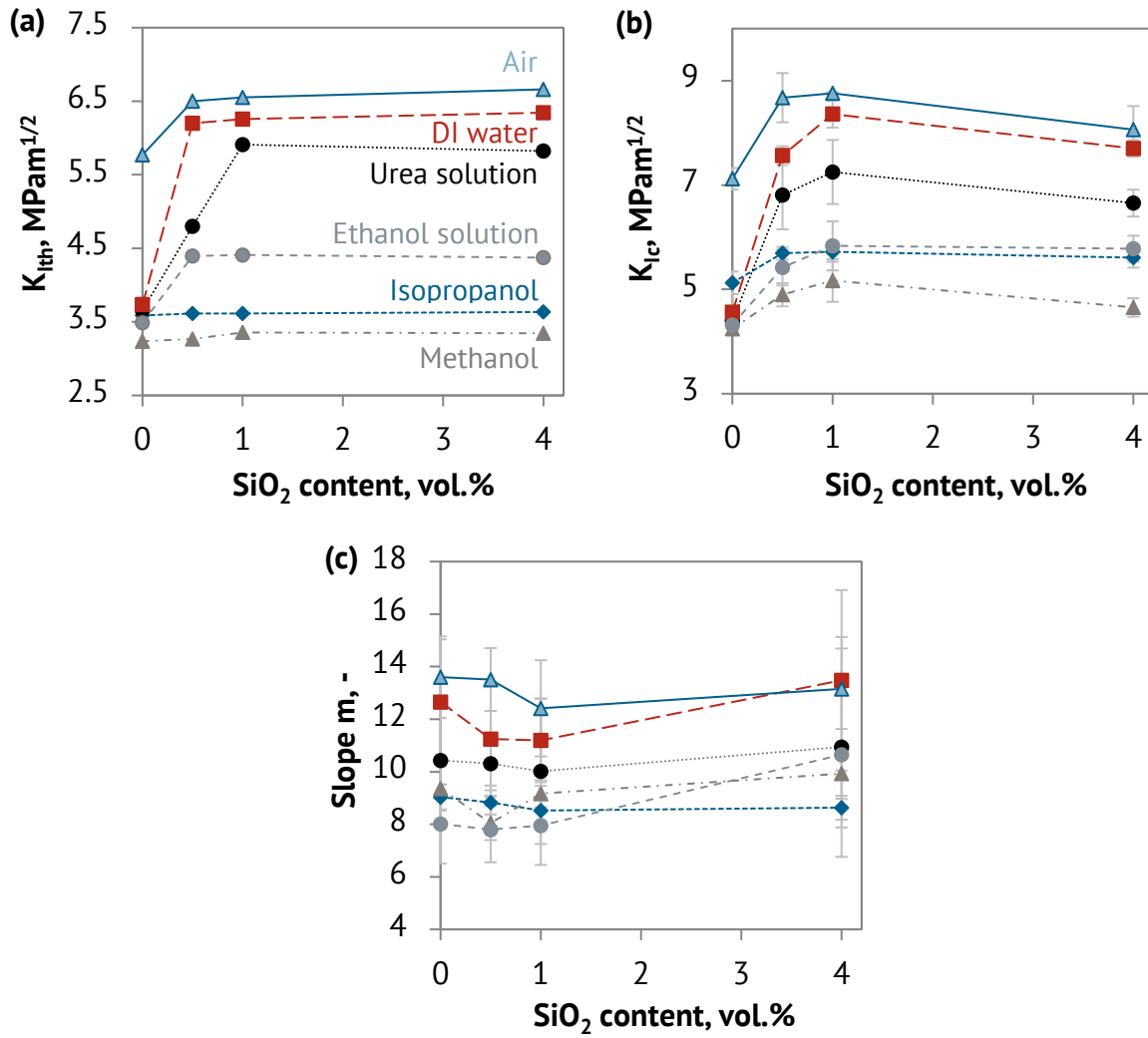
Figure 4.18: (a) K_{Ith}, (b) K_{Ic}, and (c) slope in stable crack growth region as a function of nano-SiO_2 contents in different ESC agents.

Morphological Properties

To determine the relationship between the microstructure and the crack growth mechanisms, the fractured surface of neat PC and PC-based nanocomposites was first observed by stereo microscopy and then using a scanning electron microscope (SEM). Figure 4.19 shows optical micrographs of the fractured surfaces of failed CT specimens in different ESC agents. There are three different regions in the fractured surface, which are labelled 1, 2, and 3. Area 1 is a sharp pre-crack zone produced by a fresh razor blade, and area 2 is the stable crack growth region that is the main area of energy consumption in the ESC deformation process. Thus, the dominant mechanisms responsible for the enhancement in ESC are related to this area. The dashed lines indicate the beginning of unstable crack growth propagation (Area 3) in each specimen, and the material then fractures within a

short time. As seen in Figure 4.19, the onset of unstable damaged crack growth markedly increases with the incorporation of nano-SiO_2, and this is related to the improvements in failure time and ESC resistance of PC nanocomposites in both methanol and isopropanol [6]. In the case of DI water, the onset point of catastrophic failure could not be directly used as a comparison parameter for different materials due to the different testing load. However, the optical micrographs of the PC nanocomposites exposed to DI water reveal an intense stress whitening of the entire fracture surface, whereas this morphology does not occur in neat PC [94]. This result confirms the significant difference in the deformation process quality in mild agents, which correlates well with the ESC resistance of the PC nanocomposites.
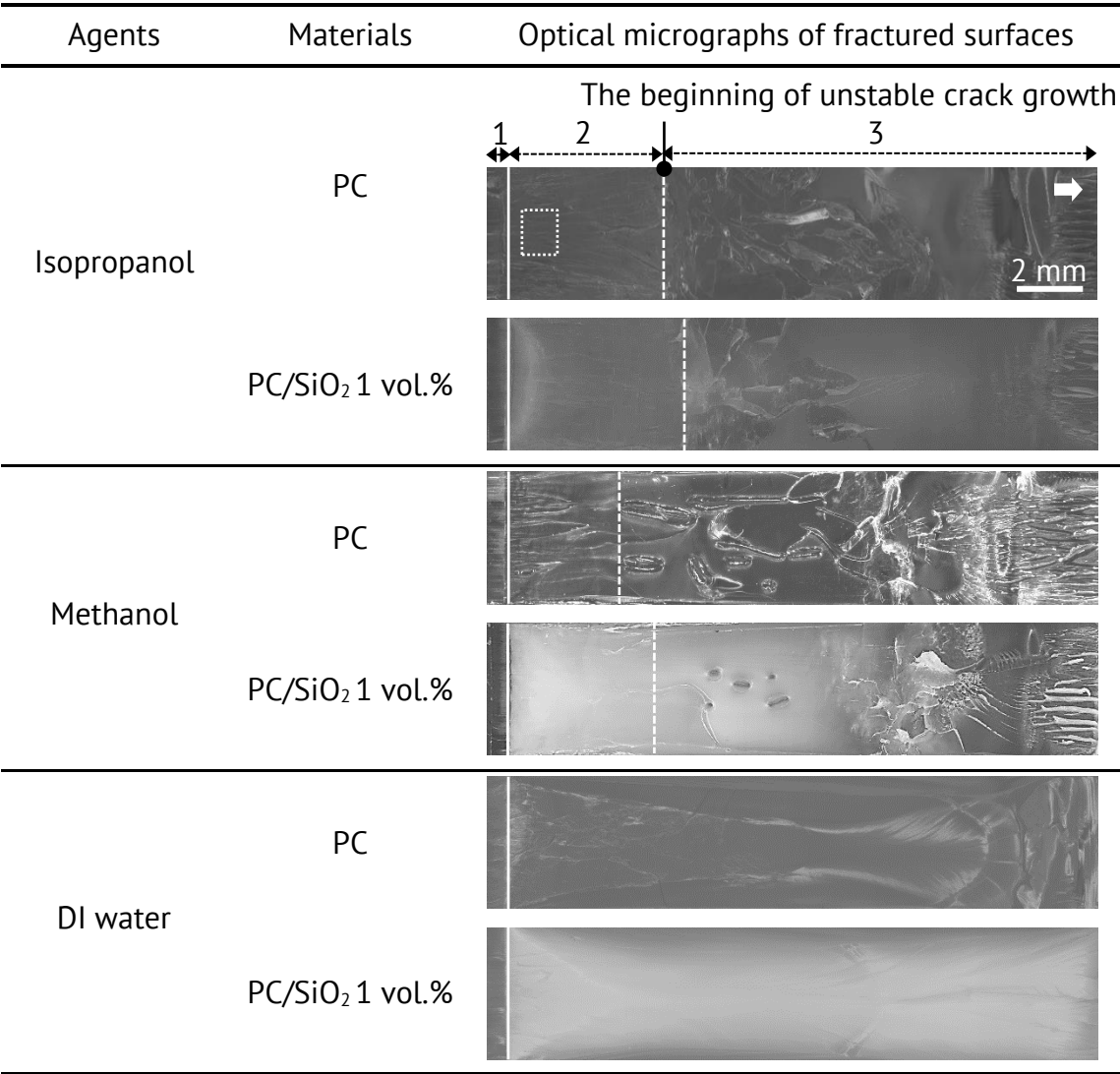
Figure 4.19: Optical micrographs of CT specimen fractured surfaces of PC and PC nanocomposites in isopropanol, methanol and DI water. The white arrows indicate the direction of crack propagation.

The deformation mechanism and the enhancement in the ESC resistance of PC in different stress cracking agents can be demonstrated by considering the SEM micrographs (in the stable crack propagation area, the square region in Figure 4.19) as shown in Figure 4.20. These micrographs present the fractured surfaces of the neat PC and PC nanocomposites, based on different crack types/shapes of the deformed area in front of the crack tip, as shown in Figure 4.16. As seen in Figure 4.20(c), the surface of PC in DI water is a smooth fractured surface without plastic deformation, implying that only a small amount of energy is dissipated during the fracture process. These morphologies confirm the brittle failure behavior of neat PC in mild agents. However, certain features of plastic deformation can be observed in the fractured surface of the neat PC in isopropanol and methanol, but only to a limited extent (Figure 4.20(a) and (b)).

It can be clearly observed from Figures 4.20(e) to (h) that the small number of nano-SiO_2 particles and their agglomerations are evenly dispersed in the PC matrix. These particles serve as sites of local stress concentrators under applied stress. They can initiate cavitation, particle pulling out/debonding, localized micro-deformation, and crack deflection of the PC matrix in nanocomposites. This statement is supported by the numerous cavities and tiny structures with a hyperbolic shape beside plastic deformation and particle debonding of the nano-SiO_2 reinforced PC (marked by white arrows). It is commonly accepted that the formation of these structures is the major energy dissipation mechanism during the deformation process [6,105,106]. These energy-dissipating events can improve the ESC resistance of nanocomposites with an appropriate nanoparticle content, especially in a mild agent (Figure 4.20(g)), where the type/shape of crack significantly changes. This also suggests that the stress whitening appearance observed in optical micrographs occurs due to the light scattering caused by these dissipative energy structures. In contrast, these structures do not occur in neat PC. Based on the SEM results, it can be stated that the presence of nano-SiO_2 in the PC significantly changes the nature of the micromechanisms of deformation of the PC, whereas no indication of a different fractured surface is observed between stress-cracking agents.
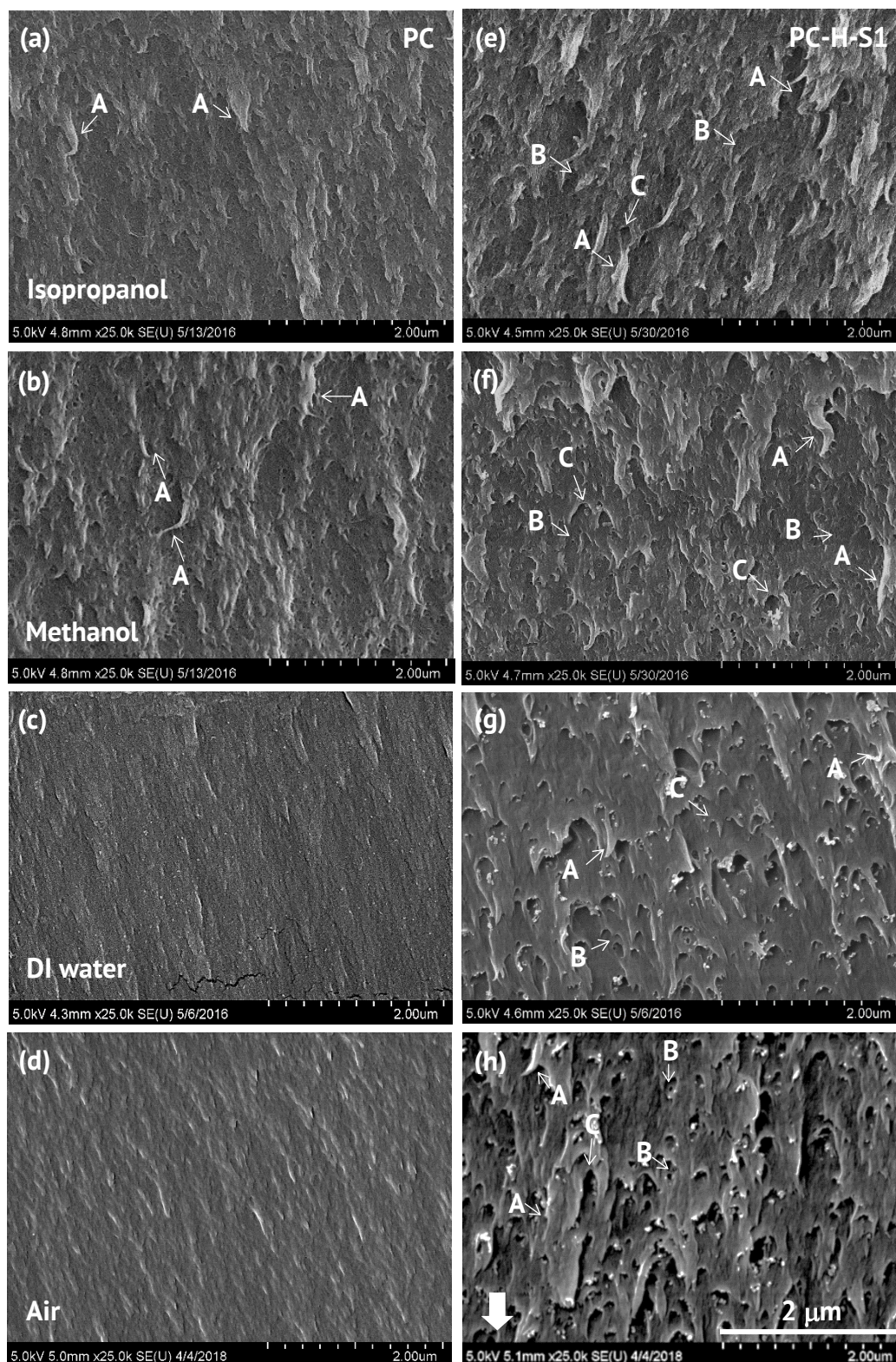
Figure 4.20: SEM images of failed CT-samples of neat PC in (a) isopropanol, (b) methanol, (c) DI water, (d) Air, and PC nanocomposites with 1 vol.% nano-SiO$_2$ in (e) isopropanol, (f) methanol, (g) DI water, (h) air. The white arrows indicate the direction of crack propagation. Features A, B, and C indicate plastic deformation, formation of cavities/nanoparticle debonding, and structures in parabolic shape, respectively.

Representative SEM micrographs showing the effect of nano-SiO_2 content on the ESC resistance of PC are given in Figure 4.21. The fractured surface morphologies reveal the greater formation of dissipative energy structures in the PC matrix with increasing nano-SiO_2 content. This is particularly true for localized microdeformation, which is indicated by an extensively elongated matrix on the fracture surface. Based on this logic, the ESC resistance of the PC nanocomposites should increase with filler content. However, a high content of nanoparticles also facilitates the agglomeration of nanoparticles in the polymer matrix. As indicated in Figure 4.21(d), the PC nanocomposite with 4 vol.% nano-SiO_2 contains more and larger nano-SiO_2 agglomerates, and this can reduce the interfacial area and weaken the performance of the nanocomposite [102]. As a result, the ESC resistance is unchanged or slightly decreased with increasing nano-SiO_2 content up to 4 vol.%, due to the compensation of these two effects.
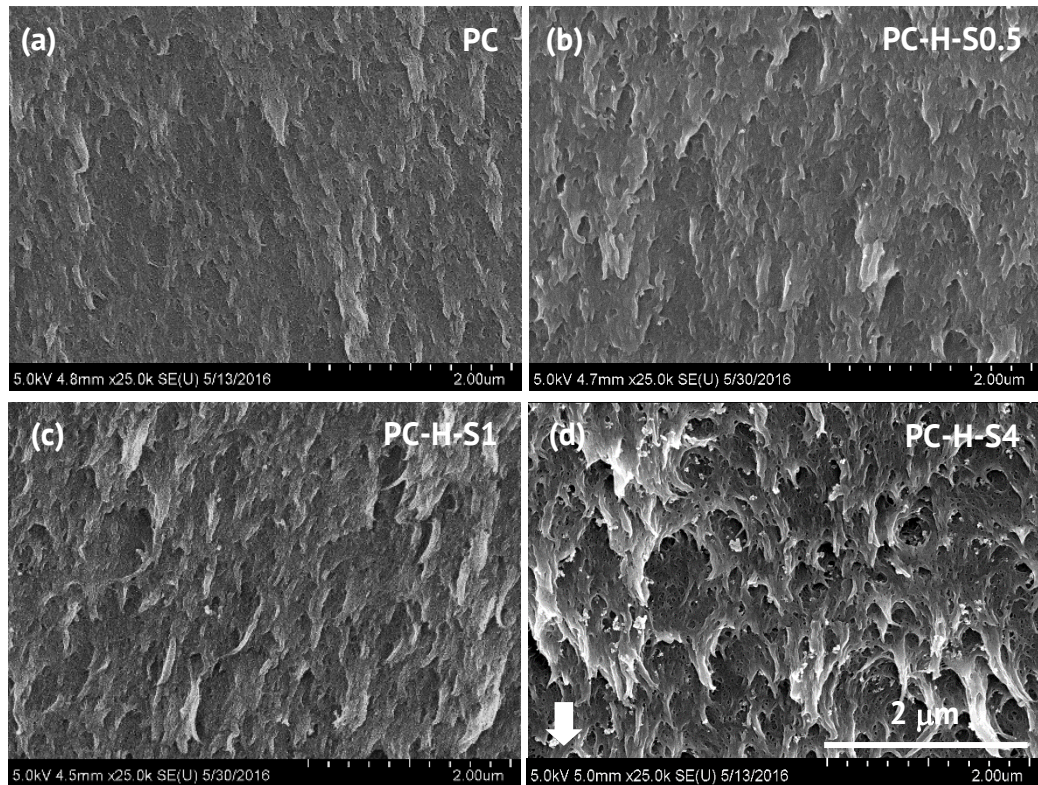
Figure 4.21: SEM images of failed CT-samples in isopropanol of (a) neat PC and PC nanocomposites with (b) 0.5 vol.%, (c) 1 vol.%, and (d) 4 vol.% nano-SiO_2. The white arrows indicate the direction of crack propagation.

4.1.5.4 Effect of Nanofiller Size

ESC Properties

As is well-known, a decrease in particle size results in an increase in the available surface area, and this ensures high levels of filler-matrix interfacial interaction, resulting in effective energy dissipation during the deformation process. In this research, the effect of filler size on the ESC resistance of PC is investigated using two different sizes of nano-SiO_2 with mean particle diameters of 7 and 12 nm. According to the manufacturer, the specific surface areas of particles with diameters of 7 and 12 nm are 220±25 m^2/g and 160±25 m^2/g, respectively.

A comparison of the damaged area development of PC and PC/SiO_2 nanocomposites filled with different nanofiller sizes in various ESC agents is shown in the form of two-dimensional optical micrographs in Figure 4.22. Adding a smaller size of nano-SiO_2 into PC also causes a significant change in the deformed pattern in mild agents and air. At a given testing time, the PC nanocomposites filled with a smaller nano-SiO_2 (7 nm) particles show a significantly smaller damaged area compared to neat PC and PC nanocomposites filled with larger particles (12 nm) in all investigated agents. This result confirms that the smaller nanoparticles are especially advantageous in reducing the growth rate of the damaged area, and hence greatly improve ESC resistance. Figure 4.23 confirms the further considerable enhancement in the ESC performance for PC filled with smaller nano-SiO_2 particles (the pattern-filled symbol) in all investigated agents as well as in air. These diagrams clearly reveal that the decrease in primary nano-SiO_2 particle size from 12 nm to 7 nm results in a significant reduction in the crack propagation rate. Simultaneously, the entire curve is shifted even further toward higher K_I values, indicating that the smaller nano-SiO_2 particles can effectively improve the ESC resistance of the PC by retarding the crack propagation and extending the onset period of catastrophic failure.

Materials	PC	PC/SiO₂ (12nm)	PC/SiO₂ (7nm)
Isopropanol			
Methanol			
Ethanol solution			
DI water			
Air			5 mm
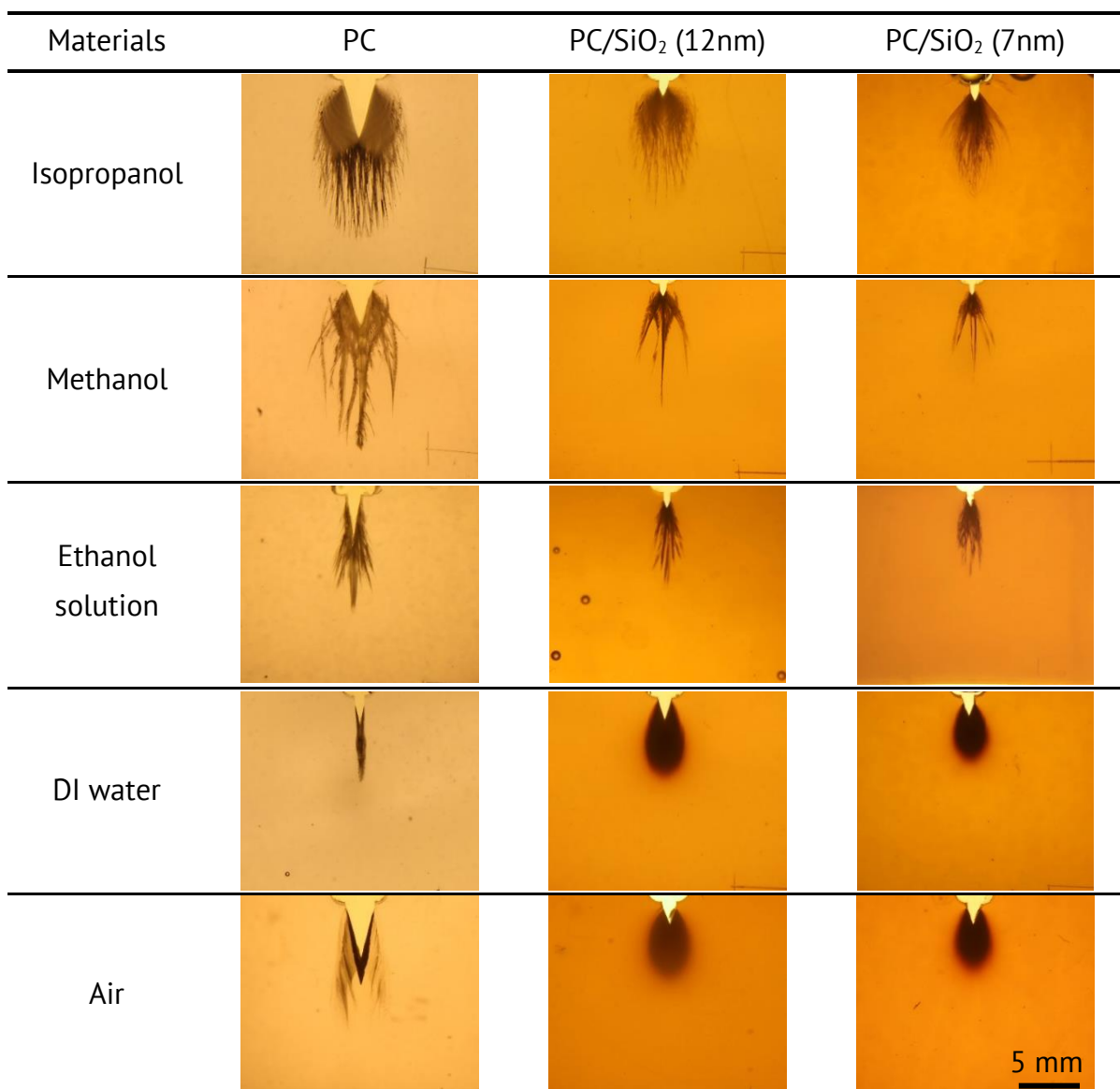
Figure 4.22: Digital images of ESC behavior in different ESC agents of PC and PC/SiO$_2$ nanocomposites (1 vol.% nano-SiO$_2$) at the same testing time.

(a) Isopropanol

da/dt, mm/s — K_I, MPam$^{1/2}$

- ◆ PC-H-S0
- ◈ PC-H-S1(7nm)
- ◇ PC-H-S1(12nm)

(b) Methanol

da/dt, mm/s — K_I, MPam$^{1/2}$
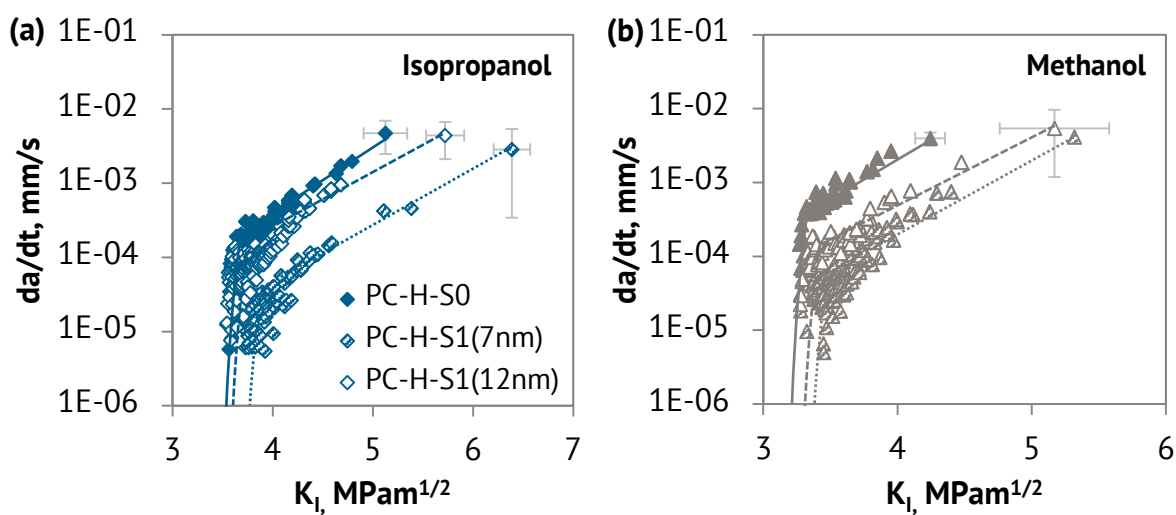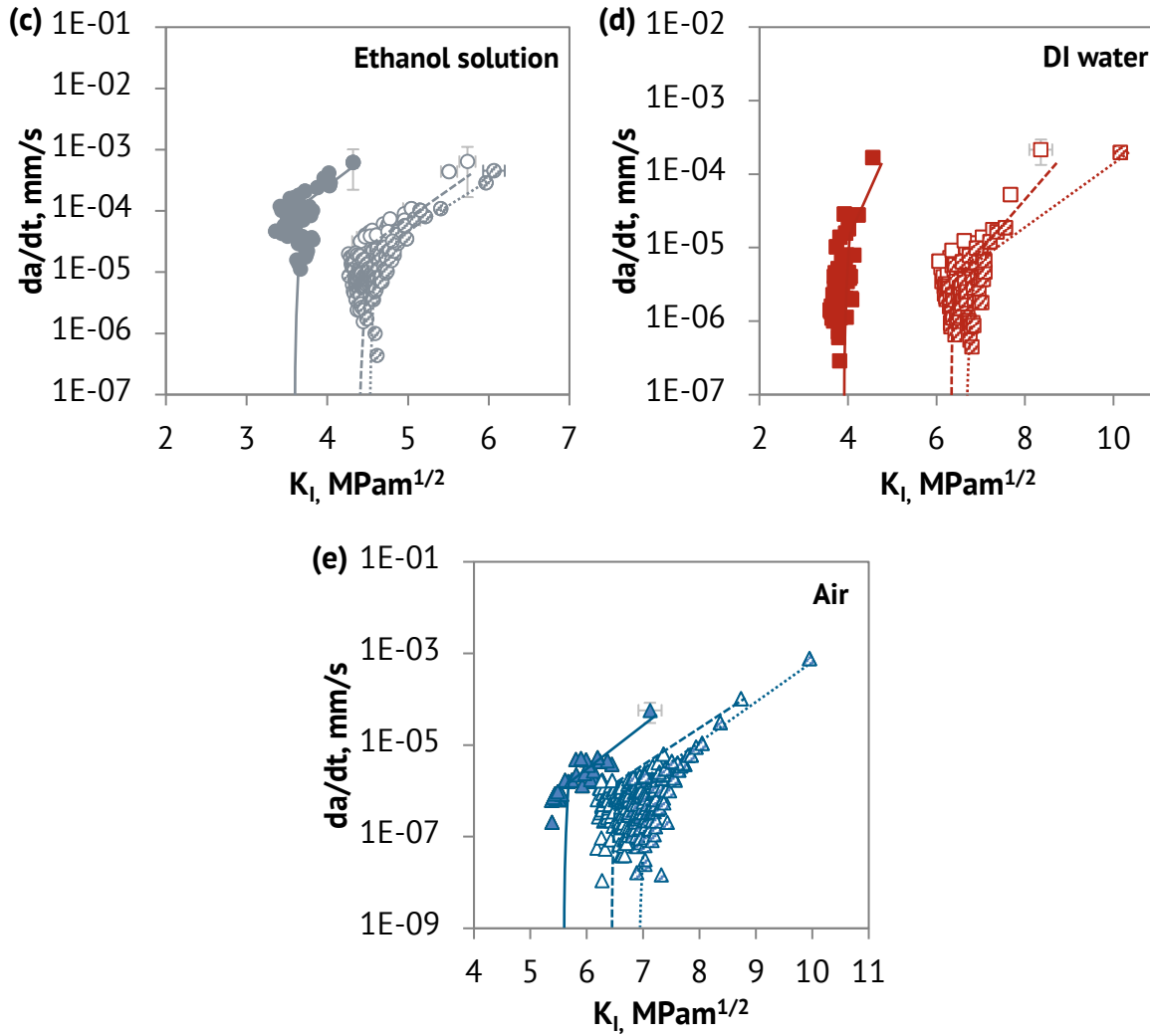
Figure 4.23: Effect of filler size on macro-crack propagation rate as a function of the K_I factor of PC/SiO$_2$ nanocomposites (1 vol.%) in different ESC agents: (a) isopropanol, (b) methanol, (c) ethanol solution, (d) DI water and (e) air.

The effects of the filler content and size of the nano-SiO$_2$ particles on K_{Ith}, K_{Ic} and the slope of the curve in the stable crack propagation region of PC and PC nanocomposites are shown in Figure 4.24 (Appendix G). The results confirm that the improvement in ESC resistance is more pronounced with the incorporation of smaller nanofillers for all investigated contents, due to the higher interfacial surface area. A greater positive energy dissipation effect is induced by smaller nanoparticles, and this enhances crack resistance, which is responsible for the improvement in ESC resistance in all ESC agents. The PC nanocomposite with 1 vol.% of 7 nm SiO$_2$ exhibits the highest ESC improvement. Accordingly, the service lifetime of the materials is significantly prolonged by about 760% and 618% in isopropanol and methanol, respectively, as compared to neat PC (see Figure 4.25). For a nano-SiO$_2$ content more than 1 vol.%, the improvements are only marginal.
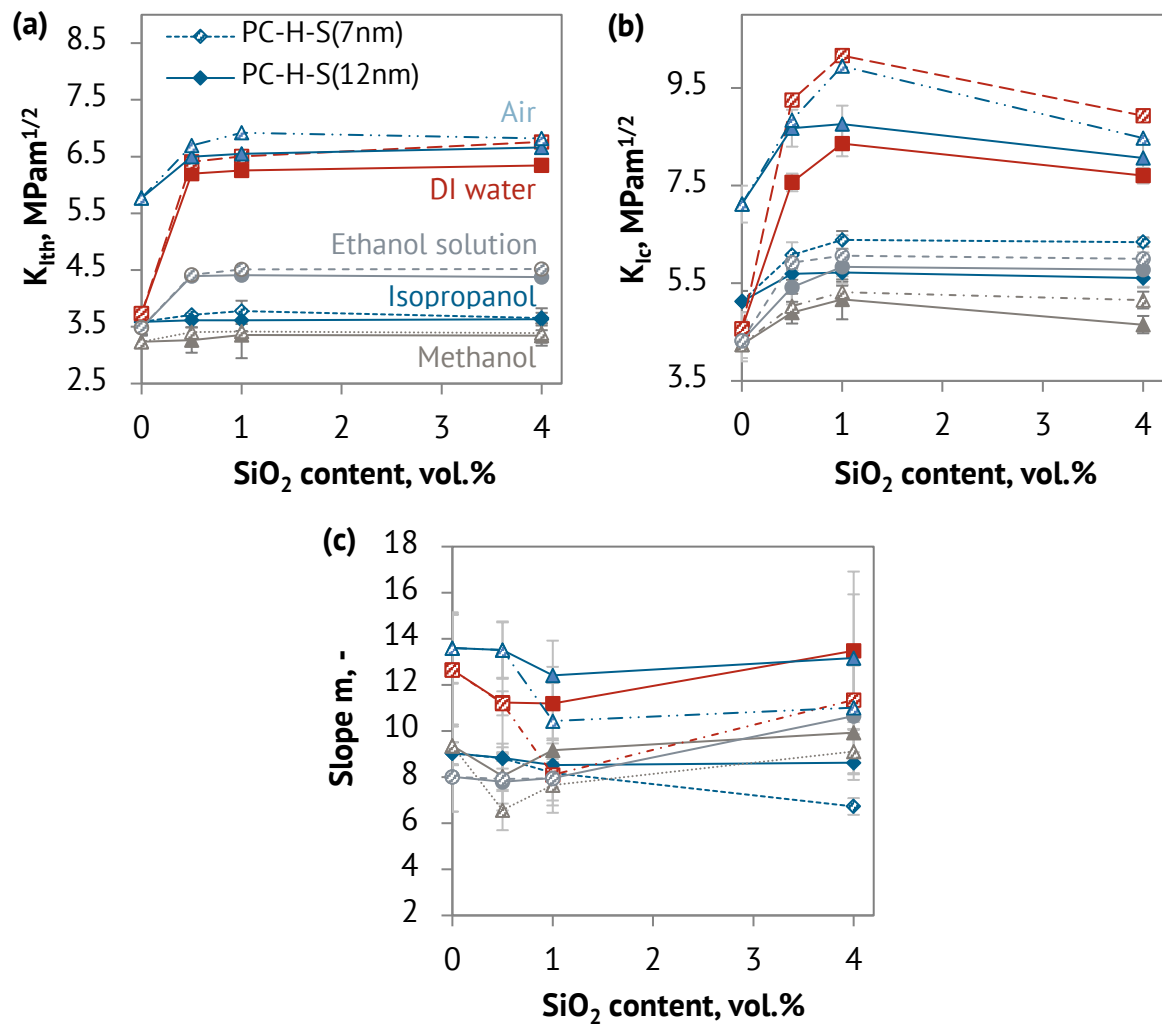
Figure 4.24: (a) K_{Ith}, (b) K_{Ic} and (c) slope in stable crack growth region as a function of nano-SiO_2 contents and size in different ESC agents.
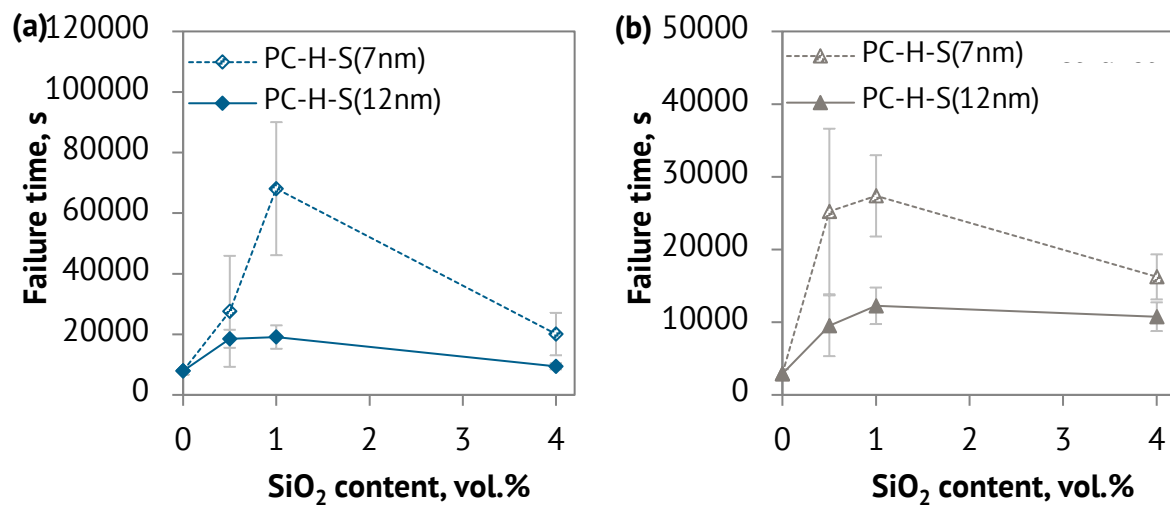
Figure 4.25: Effect of filler size on failure time of PC/SiO_2 nanocomposites in different ESC agents: (a) isopropanol and (b) methanol.

Morphological Properties

The enormous enhancement in the ESC resistance from the incorporation of smaller nano-SiO_2 particles is confirmed by SEM micrographs of the fractured surface of the CT specimen in different ESC agents, as shown in Figure 4.26. When the size of the primary nano-SiO_2 particles was decreased from 12 nm to 7 nm, the fractured surface morphologies indicate more energy dissipation events, as evidenced by the extensive localized microdeformation, cavitation and particle debonding in the PC matrix. This confirms that decreasing the particle size results in an increase in the available surface area, promoting the formation of structures induced by nanoparticles that can dissipate energy more effectively during the fracture process. As a result, a greater improvement in the ESC resistance is achieved compared to nanocomposites filled with larger particles.
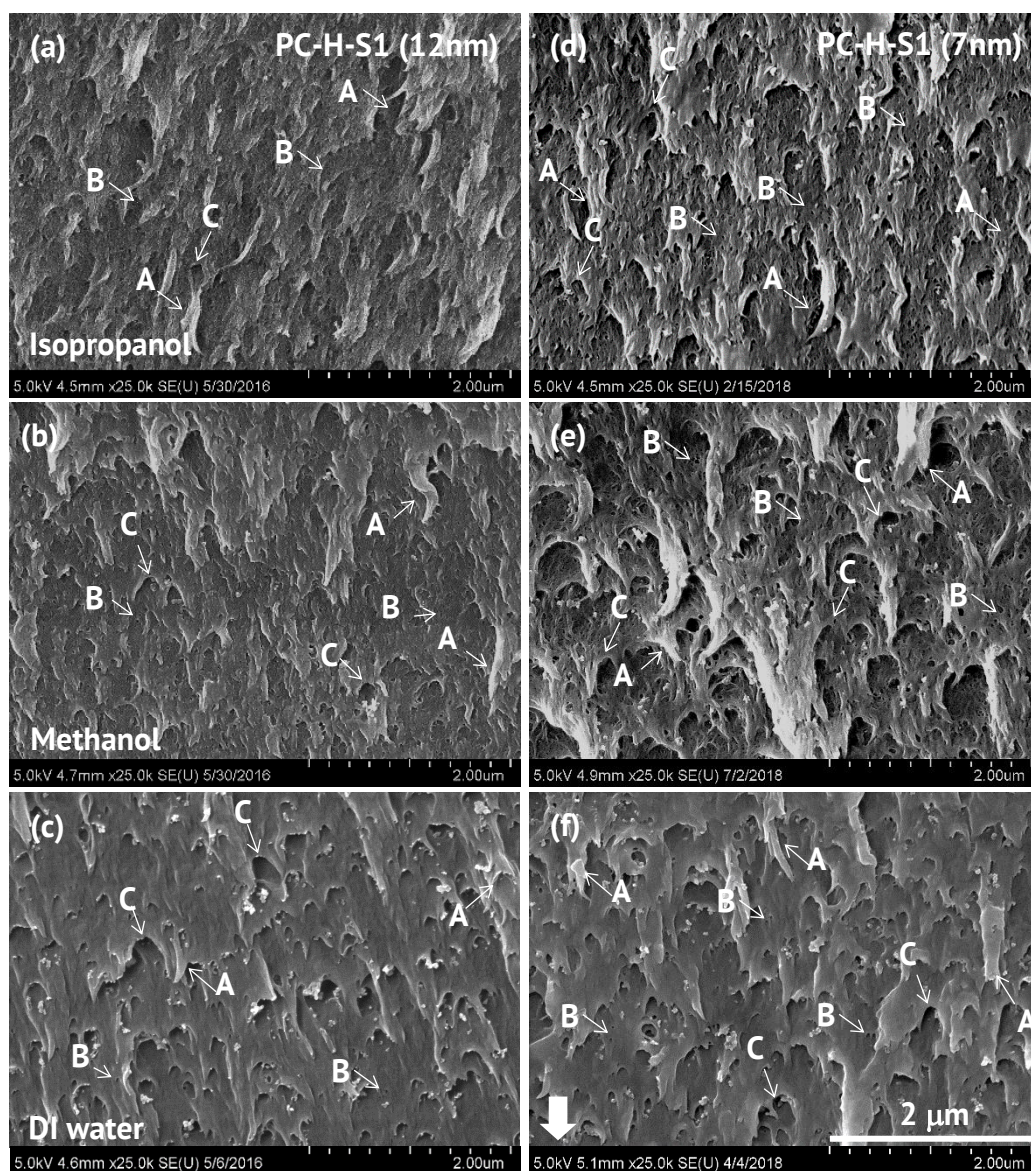
Figure 4.26: SEM micrographs of PC filled with 1 vol.% of different nano-SiO_2 size: (a)-(c) 12 nm and (d)-(f) 7 nm in isopropanol, methanol, and DI water, respectively.

4.1.5.5 Effect of Properties of ESC Agent

Figure 4.27 displays the correlation between the K_{Ic} of different materials and the solubility parameter of the stress cracking agent. In accordance with Wright [47], the result in the range studied here is similar to the right-hand side of the general W-curve of critical strain versus the solubility parameter of the solvent for PC. Neat PC is prone to stress cracking when contaminated with alcohol solvents, due to the similarity in the solubility parameters. Methanol, which has a lower molar volume than isopropanol, is much more aggressive due to its rapid diffusion within the polymer structure. As explained earlier, ESC agents tend to weaken intermolecular forces between polymer chains and facilitate molecular disentanglement of the polymer. This phenomenon promotes macroscopic brittle crack formation and consequently leads to ESC failure.

In the case of nanocomposites, the extensive internal interface between the nanofiller and the polymer matrix can either support the absorption of the ESC agent or control new structural arrangements on the molecular scale [8,14]. Each behavior has an opposite effect on the ESC resistance of materials. However, as already demonstrated in the absorption test results, the uniform dispersion of the nano-SiO_2 particles can act as impermeable obstacles rendering the liquid molecules pathways more tortuous, thus even delays the absorption process in the materials. Moreover, the results in this study also display a clear enhancement in ESC resistance with the presence of nanoparticles, and especially in mild agents, where the solubility parameter of the agent differs significantly from that of neat PC [8]. The aforementioned difference in the type/shape of the deformed area in mild agents results in extraordinary improvements in ESC resistance by triggering a kind of blunting of the micro-crack due to multiple deformation processes on a small scale [8]. These results indicate that the combination effects of the retardation of ESC agent diffusion and the new structural arrangements induced by nanoparticles provide synergistic effects, which promote a great improvement in the ESC resistance of PC-based nanocomposites.

In fact, the degree of ESC enhancement depends not only on the differences in the solubility parameter of the ESC agent (δ_a) and polymer (δ_p) but also relates to the molar volume (V) of the ESC agents. The lower molar volume and less bulky molecular structure of the agent accelerate the process of macroscopic brittle crack formation, and vice versa. Therefore, both of these parameters must be taken into account. Hence, the correlation between the relative values of K_{Ic} for the PC nanocomposites with neat PC as a function of $(\delta_a-\delta_p)/V^{1/2}$ for each ESC agent is plotted in Figure 4.28. It is interesting to note that the

degree of ESC improvement for the PC-based nanocomposites in this study is well described by a simple linear relationship as function of $(\delta_a-\delta_p)/V^{1/2}$.

Figure 4.27: K_{Ic} of PC and PC nanocomposites with different filler concentration and size as a function of solubility parameter of ESC agents.
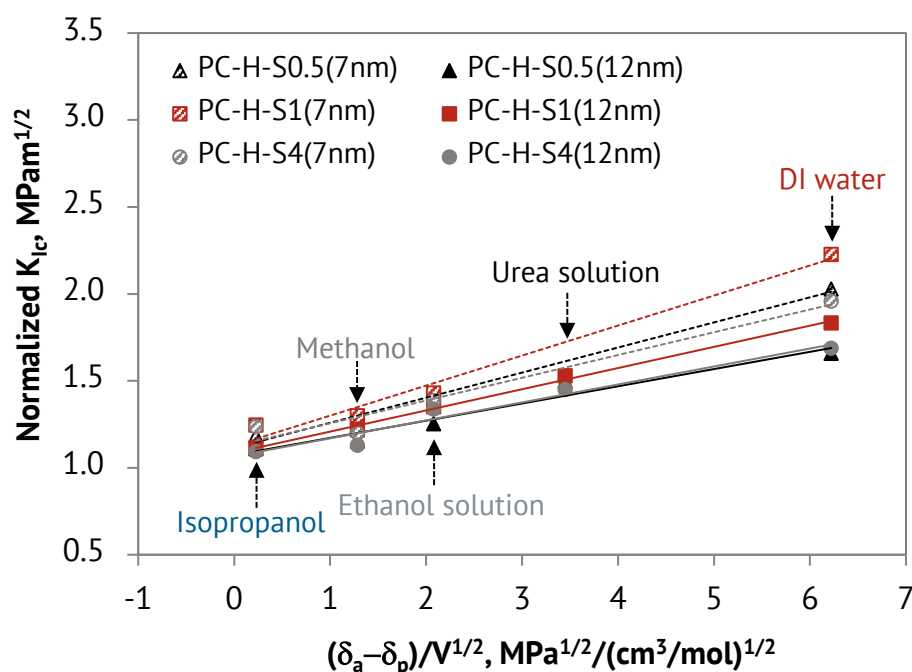
Figure 4.28: Normalized K_{Ic} of different materials as a function of solubility parameter and molar volume of ESC agents.

4.1.5.6 Effect of Molecular Weight of Polymer

As is well known, amorphous polymers are susceptible to ESC failure due to their lack of an ordered structure. Stress cracking agents are better able to diffuse into their molecular network, and this promotes premature failure via molecular disentanglement. As a result, molecular parameters such as molecular weight and its distribution play an important role in the ESC behavior of amorphous polymers. To investigate the influence of molecular weight on the ESC resistance of PC, a different grade of PC with lower molecular weight was also investigated in different agents. The molecular weights of low (PC-L) and high (PC-H) molecular weight PC are 24,000 and 31,000 g/mol, respectively.

Firstly, the influences of nano-SiO_2 particles on the ESC resistance properties of PC-L-based nanocomposites are shown in Figures 4.29 and 4.30 (Appendix H). Similarly, a significant improvement in ESC resistance can also be observed in PC-L based nanocomposites in all investigated agents, as indicated by an increase in the values of K_{Ith} and K_{Ic} and a decrease of slope in the stable crack growth region for the nanocomposites. This is particularly true in the case of smaller nano-SiO_2 particles, which provide a greater surface area, ensuring high levels of energy dissipation during the fracture process. In all ESC agents, the PC-L nanocomposites with 1 vol.% loading of 7 nm SiO_2 particles exhibit the highest improvement in the ESC resistance.

Moreover, it can be seen that the degree of the ESC resistance enhancement is again related to the properties of ESC agents, such as their molar volume and solubility parameter relative to the polymer, as seen in Figure 4.30. The maximum improvement in ESC resistance is shown when the solubility parameter of the stress-cracking agent is much higher than that of PC, as in DI water. The maximum enhancement of the K_{Ith} and K_{Ic} values as well as the greatest reduction of the crack propagation rate in the stable crack growth region, is achieved by approximately 102%, 140%, and 80%, respectively. As discussed earlier, this enormously improved ESC resistance of the PC-based nanocomposite in mild agents is attributed to the formation of multiple crazing in the deformation area, which is induced by small nanoparticles [8].

Figures 4.29: (a) K_{Ith}, (b) K_{Ic} and (c) slope in stable crack growth region of PC-L based nanocomposites as a function of nano-SiO_2 contents and sizes in different ESC agents.
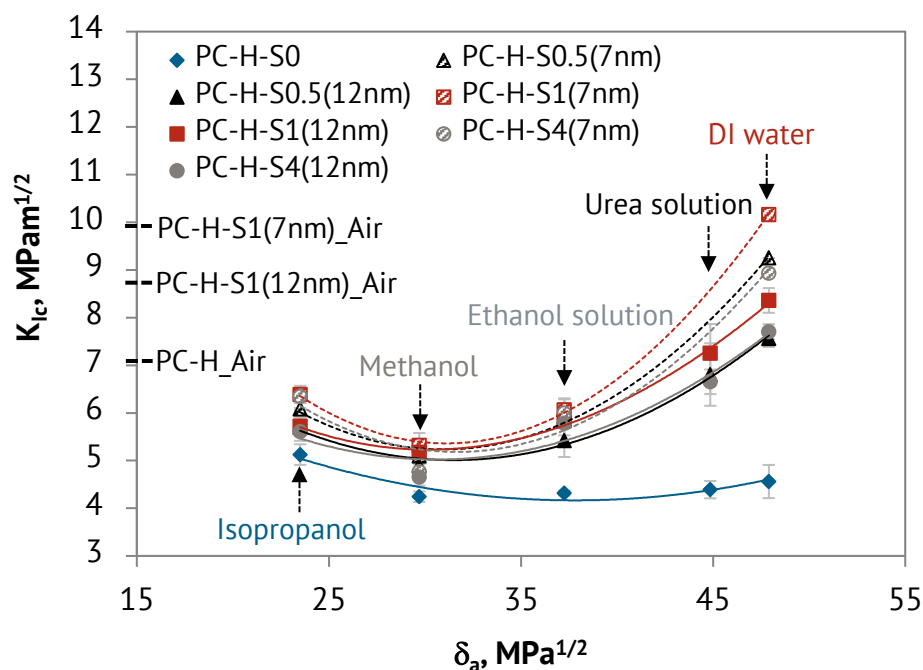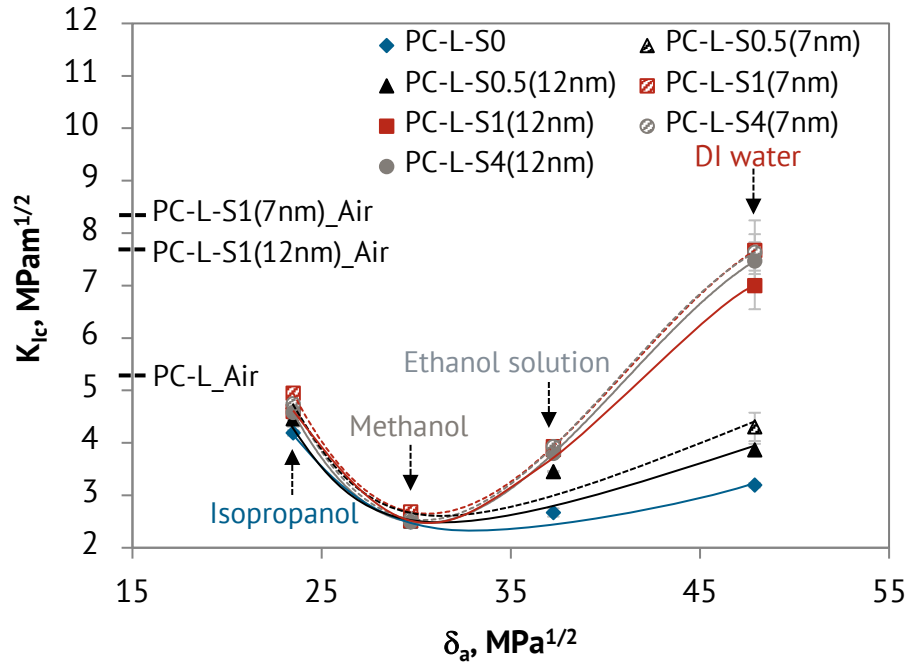
Figures 4.30: K_{Ic} of PC-L based nanocomposites with different filler concentration and size as a function of solubility parameter of ESC agents.
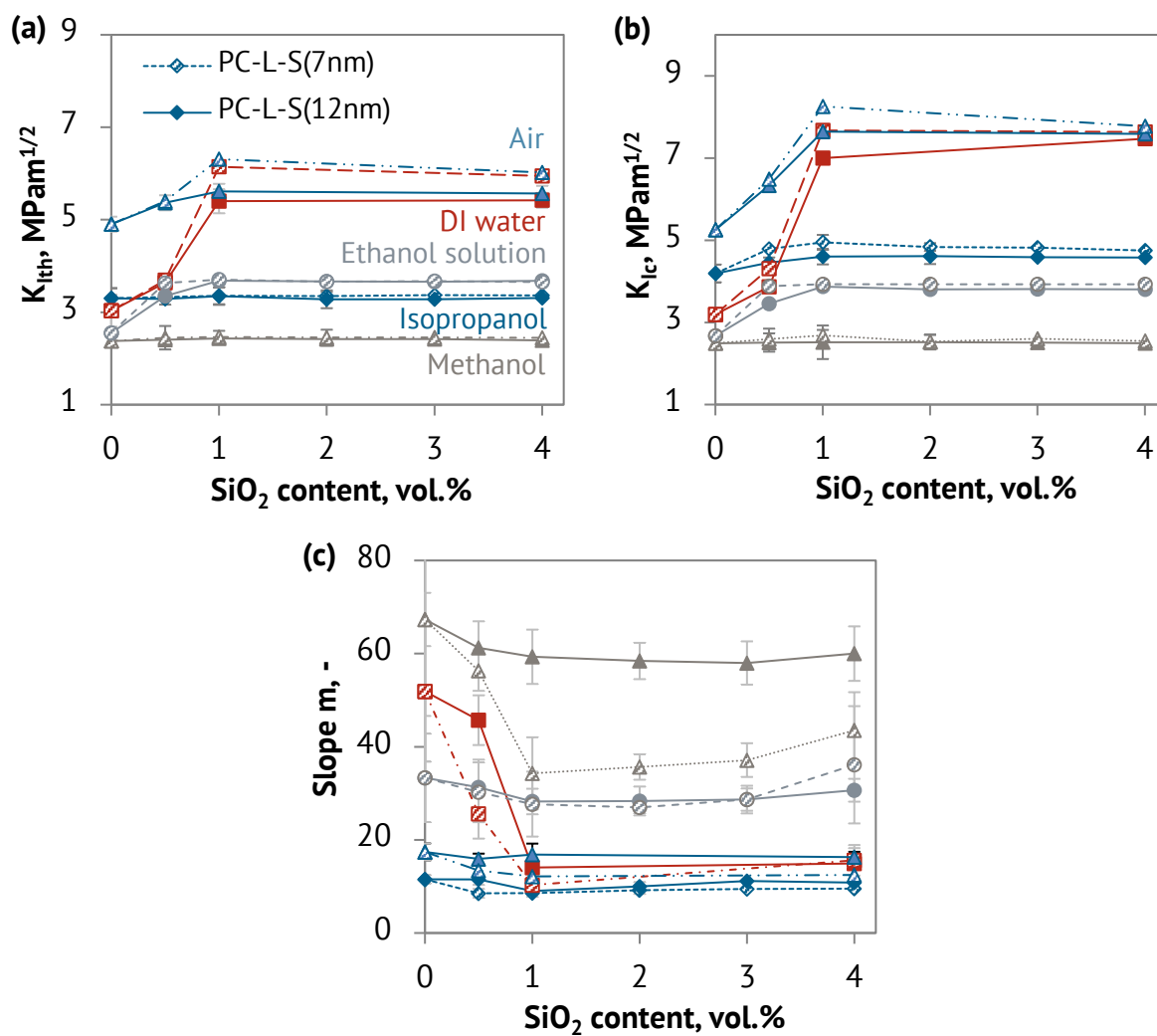
Figures 4.31 (a)-(d) illustrate the effect of the molecular weight of PC on macro-crack length propagation as a function of K_I factor in different ESC agents. A comparison clearly reveals an improvement in ESC resistance of both neat PC and PC nanocomposite with increasing molecular weight of PC. This result is reflected in a decrease of the crack prop-agation rate and the slope of the curve in the stable crack growth region. Simultaneously, the entire curve is shifted toward higher K_I values. The average values of the K_{Ith}, K_{Ic} and the slope of curve in the stable crack propagation region of both PC and PC nanocompo-sites influenced by the molecular weight of PC are shown in Figure 4.32. An obvious enhancement in K_{Ith} and K_{Ic} as well as a reduction of crack propagation rate at any given nano-SiO_2 content for different ESC agents, is obtained with increasing molecular weight of the PC. This is attributed to the fact that a higher molecular weight provides more entanglement of the polymer chains. This causes an increase in craze stability and fibril density, which contributes to greater resistance to the stress cracking agent transport [5,46]. This result also correlates with the decrease in the diffusion coefficient of the ESC agents with increasing molecular weight of the PC, as earlier discussed in section 4.1.5.1. As a result, a high level of ESC resistance is achieved due to the more stable craze devel-opment in the PC with high molecular weight.
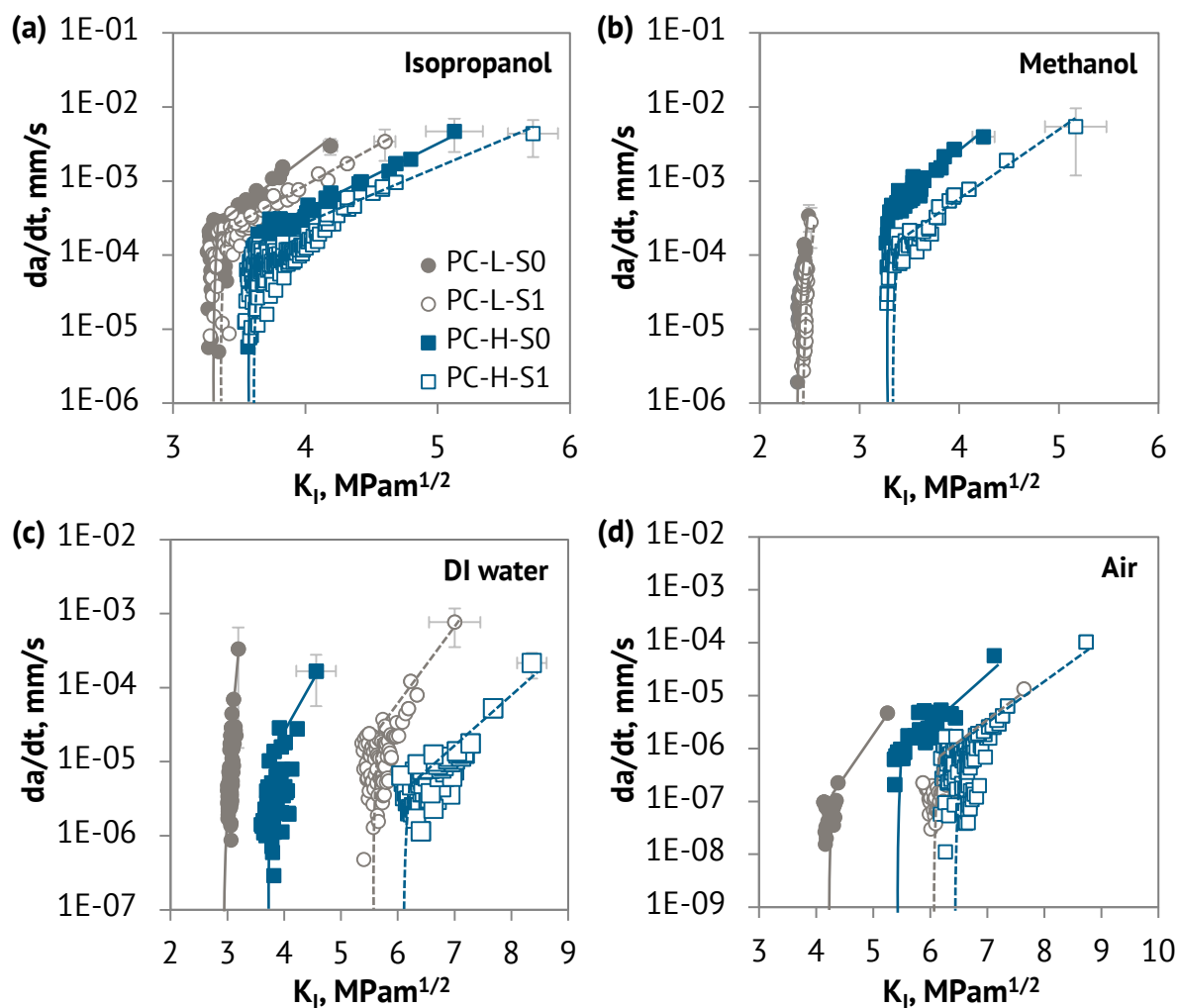
Figures 4.31: Effect of molecular weight on macro-crack propagation rate as a function of the K_I factor of PC/SiO$_2$ nanocomposites (1 vol.%) in different ESC agents: (a) isopropanol, (b) methanol, (c) DI water and (d) air.
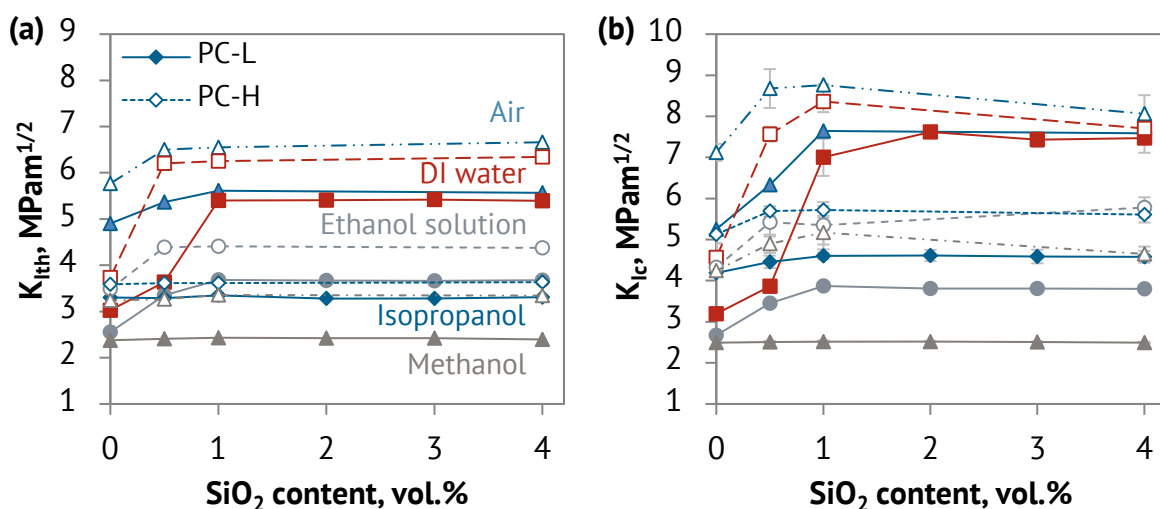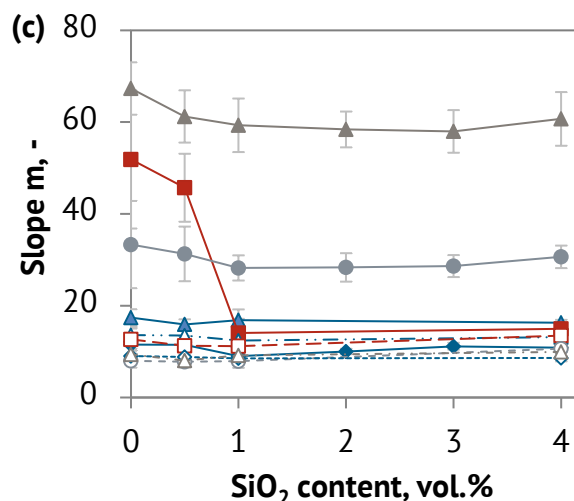
Figures 4.32: (a) K_{Ith}, (b) K_{Ic}, and (c) slope in stable crack growth region as a function of nano-SiO$_2$ contents and molecular weight of PC in different ESC agents.

An overview of the enhancement degree in ESC resistance by increasing the molecular weight of the PC is considered based on the relative K_{Ic} values, obtained by dividing the K_{Ic} of PC-H by that of PC-L, as shown in Figure 4.33. In the case of neat PC, the influence of molecular weight is most significant in aggressive agents such as methanol. As discussed earlier, the higher molecular weight is able to build up effective chain entanglements, which contribute to greater craze stability and fibril density, resulting in a higher resistance to severe stress cracking transport through the polymer structure during the diffusion process.

Similarly, the increased molecular weight of the PC gives rise to an outstanding relative K_{Ic} value for PC/SiO$_2$ nanocomposites with both nano-SiO$_2$ particle sizes of 7 and 12 nm, and particularly evident in methanol and DI water. The greatest enhancement in the ESC resistance is observed in PC filled with 0.5 vol.% nano-SiO$_2$ in DI water, reflecting the different quality of the deformation processes in these two different molecular weight PC nanocomposites. The change in deformation mechanism towards multiple crazing induced by smaller quantities of nanoparticles occurs more effectively in PC-H by triggering much more dissipative energy structures on its fractured surface, as seen in Figure 4.34. This result correlates well with the toughness properties of PC-H, which are significantly enhanced at very low nano-SiO$_2$ content as in 0.5 vol.%, confirming a high potential of energy dissipation within the fracture process. Therefore, it can be suggested that the molecular weight of the polymer is an important parameter for controlling a transfor-

mation of the deformation mechanism from a brittle to tough fracture via multiple craz-ing. This ultimately provides an opportunity to tune the desired properties of the polymer nanocomposites, including ESC resistance.

(a) PC-H-S(12nm)

(b) PC-H-S(7nm)
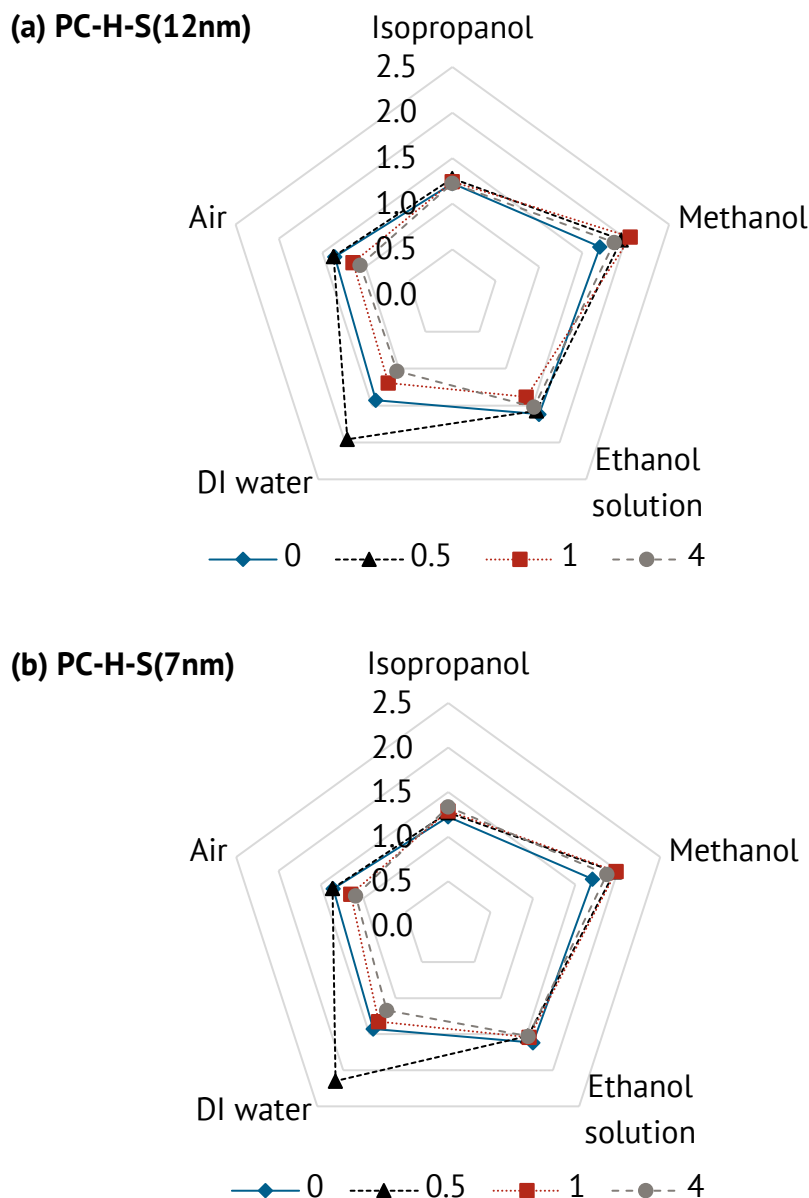
Figures 4.33: Relative K_{Ic} improvement based on molecular weight parameter of PC nanocomposites filled with different nano-SiO$_2$ size: (a) 12nm and (b) 7 nm.

Morphological Properties

The fractured surfaces of two different molecular weights PC filled with nano-SiO$_2$ (12 nm) in different ESC agents is shown in Figure 4.34. It can be seen that the molecular weight of PC has distinct effect on the macroscopic fracture appearance. More plastic

deformation, cavitation and particle debonding took place in the PC-H matrix (Figure 4.34(a)-(c)) in all fluids used, and especially in DI water. Thus, it can be stated that a greater fraction of the energy dissipation through these toughening mechanisms occurs in the PC-H, and this results in much better ESC resistance compared to PC-L nanocomposites.
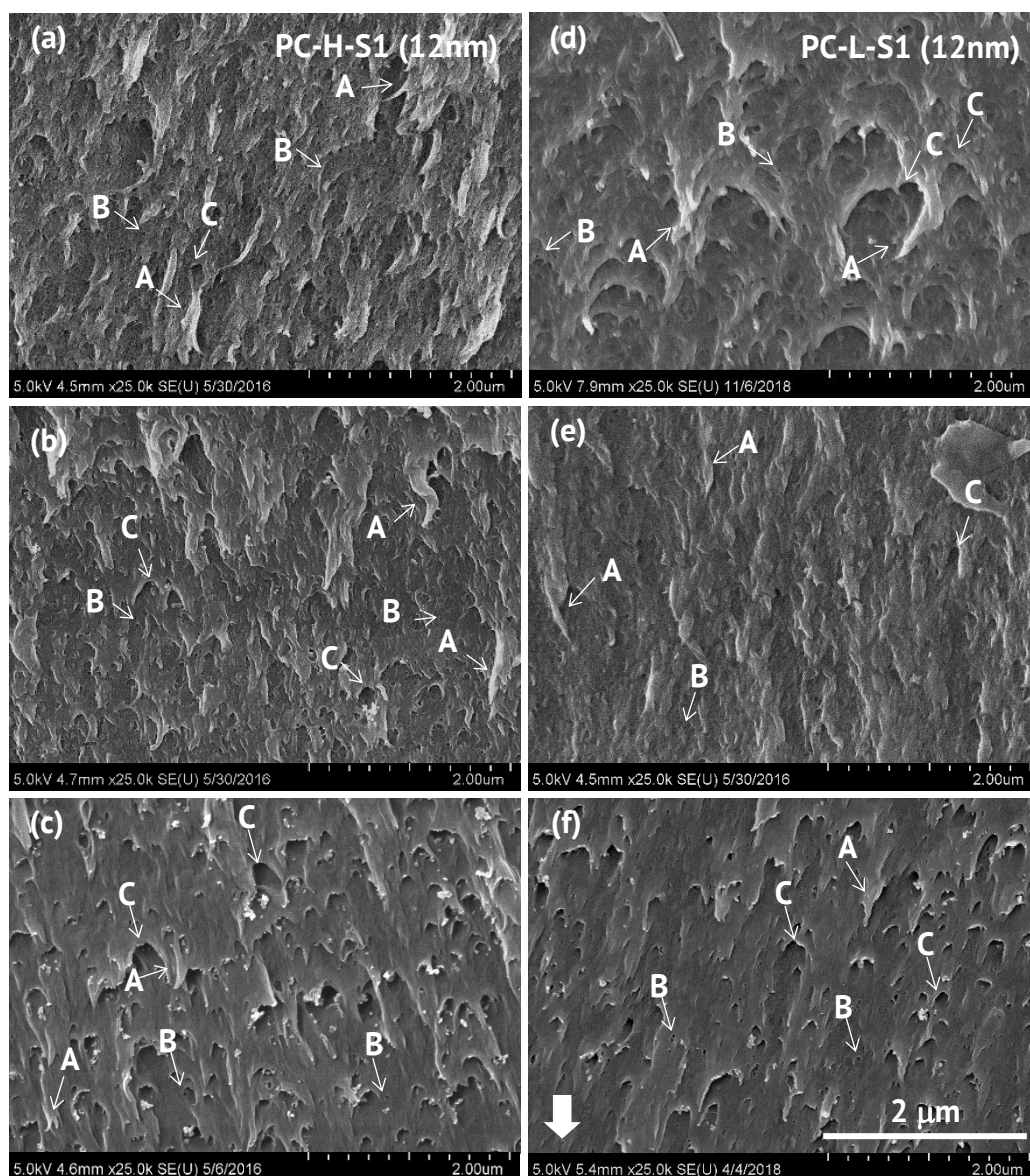
Figures 4.34: SEM micrographs of different molecular weight PC filled with 1 vol.% nano-SiO_2: (a)-(c) PC-H and (d)-(e) PC-L in isopropanol, methanol, and DI water, respectively. The white arrows indicate the direction of crack propagation. Features A, B, and C indicate plastic deformation, formation of cavities/nanoparticle debonding, and structures in parabolic shape, respectively.

4.1.5.7 Prediction of ESC Behavior of PC nanocomposite

Since premature failure due to ESC is a major safety and economic concern, the ability to predict ESC behavior can enhance product performance and consequently reduce product failure during service. As noted above, the ESC behavior of materials is strongly influenced by stress-cracking agents and the content and size of the nanofiller. Therefore, the correlation of the relative K_{Ic} of PC-based nanocomposites to neat PC (tested in air) with the solvent solubility parameters and molar volume is shown in Figure 4.35.

Figure 4.35: Relationship between solvent solubility parameter and its molar volume, filler content and its size, and relative K_{Ic} of (a) PC-H and (b) PC-L based nanocomposites.

The equation that fits the experimental data is proposed as in equation 4.2.

$$K_{Ic,\ nanocomposite} = K_{Ic,\ neat\ PC(air)}\ [a + bx + cx^2 + dxlnv_f + ex^3] \qquad (4.2)$$

where

$K_{Ic,\ nanocomposite}$	= Critical stress intensity factor of PC nanocomposite
$K_{Ic,\ neat\ PC}$	= Critical stress intensity factor of neat PC in air
v_f	= Volume fraction of nano-SiO$_2$
x	= Term of ESC agent properties; $(\delta_a-\delta_p)/V^{1/2}$
δ_a	= Total solubility parameter of ESC agent
δ_p	= Total solubility parameter of polymer
V	= Molar volume of ESC agent
a, b, c, d, e	= Constant parameters from the experiment data fitting which are

> 0.757, -0.273, 0.114, 0.0005, and -0.012 for neat PC-H
>
> 1.007, -0.455, 0.241, -0.0074, and -0.025 for PC-H/SiO$_2$ (7nm)
>
> 0.857, -0.216, 0.114, 0.0005, and -0.012 for PC-H/SiO$_2$ (12nm)
>
> 1.026, -1.095, 0.540, 0.054, and -0.060 for neat PC-L
>
> 1.237, -1.232, 0.610, 0.030, and -0.066 for PC-L/SiO$_2$ (7nm)
>
> 1.152, -1.095, 0.552, 0.039, and -0.060 for PC-L/SiO$_2$ (12nm)

The estimated value of K_{Ic} from the fitting equation shows an appropriate linear dependence on the experimental data, as shown in Figure 4.36. Therefore, this equation could be proposed as an useful tool for predicting the ESC behavior of PC-based nanocomposites from several perspectives. Firstly, prediction of the deterioration in ESC performance of PC-based materials due to the contamination of chemicals during service can be achieved by using the environmental liquid properties, such as its molar volume and solubility parameter, in the equation. Conversely, due to the remarkable improvement in the ESC resistance of PC-based nanocomposites creates some challenges in material characterization, since testing times become much longer. The determination of K_{Ic} for highly ESC-resistant materials such as in mild agents and air may take six months or more, and this is not cost-effective. Therefore, it is possible to use this equation to determine the value of K_{Ic} in a long-term cracking test from short-term experiments in aggressive agents, which allows us to minimize the testing time. The proposed equation can also be adapted to estimate a suitable amount of nanofiller to provide desirable properties for a PC-based product, while considering the expected stress levels and the exposed fluids in end-use conditions.

Figure 4.36: Correlation between estimated result from the proposed equation and experimental data of PC-H and PC-L based nanocomposites with the nano-SiO$_2$ particles size of (a), (c) 12nm and (b), (d) 7nm, respectively.

4.1.5.8 Effect of Temperature

ESC Properties

As is well known, the environmental temperature has a noticeable influence on the ESC resistance of polymers. According to Wright [47], the values of the stress and strain rates required to initiate ESC decrease as the temperature increases, accelerating the cracking process in the material. Therefore, the effect of temperature on the ESC behavior of PC-based nanocomposites was investigated at four different temperatures ranging from 23°C to 48°C (in order to stay below the boiling points of the agents).

Figure 4.37 shows the influence of temperature on the crack propagation rate as a function of K_I factor for PC-based nanocomposites in isopropanol. The corresponding values of K_{Ith}, K_{Ic} and the slope of curve in the stable crack growth for different materials are shown in Figure 4.38. It can be seen that both neat PC and PC nanocomposites exhibit a decrease in crack growth resistance with increasing temperature, as reflected by an increase in the crack propagation rate and a decrease in the K_{Ic} of the materials. This can be attributed to an increase in the free volume at higher temperatures, which contributes to greater transport of the agent into the polymer structure. As discussed earlier, the more rapid the absorption of the chemical agent, the faster the polymer will be subjected to crazing and cracking. As a result, a decreased in ESC resistance with increasing temperature is occurred, as seen in Figure 4.38. Accordingly, the failure time of the materials decreases as temperature increases.

However, it should be noted that adding small amounts of nano-SiO_2 particles to PC still has a positive effect on the ESC resistance at all elevated temperatures by postponing the final failure of the materials. PC nanocomposites with 1 vol.% of nano-SiO_2 particles exhibit the highest improvement in K_{Ith} and K_{Ic} values compared with neat PC. A similar result is also found in other ESC agents (Appendix I and J).
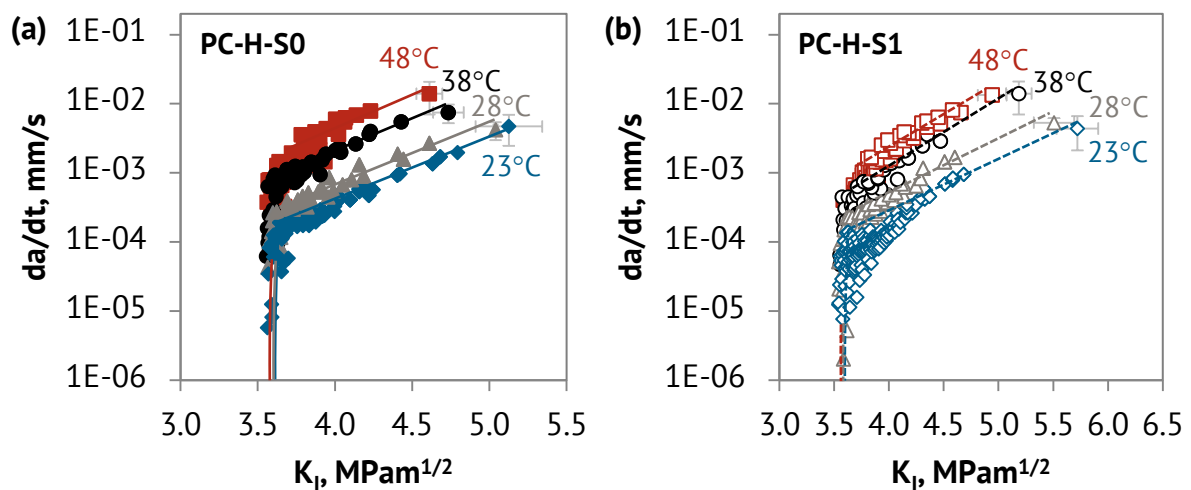
Figure 4.37: Effect of temperature on crack propagation rate as a function of K_I factor of PC nanocomposites in isopropanol.
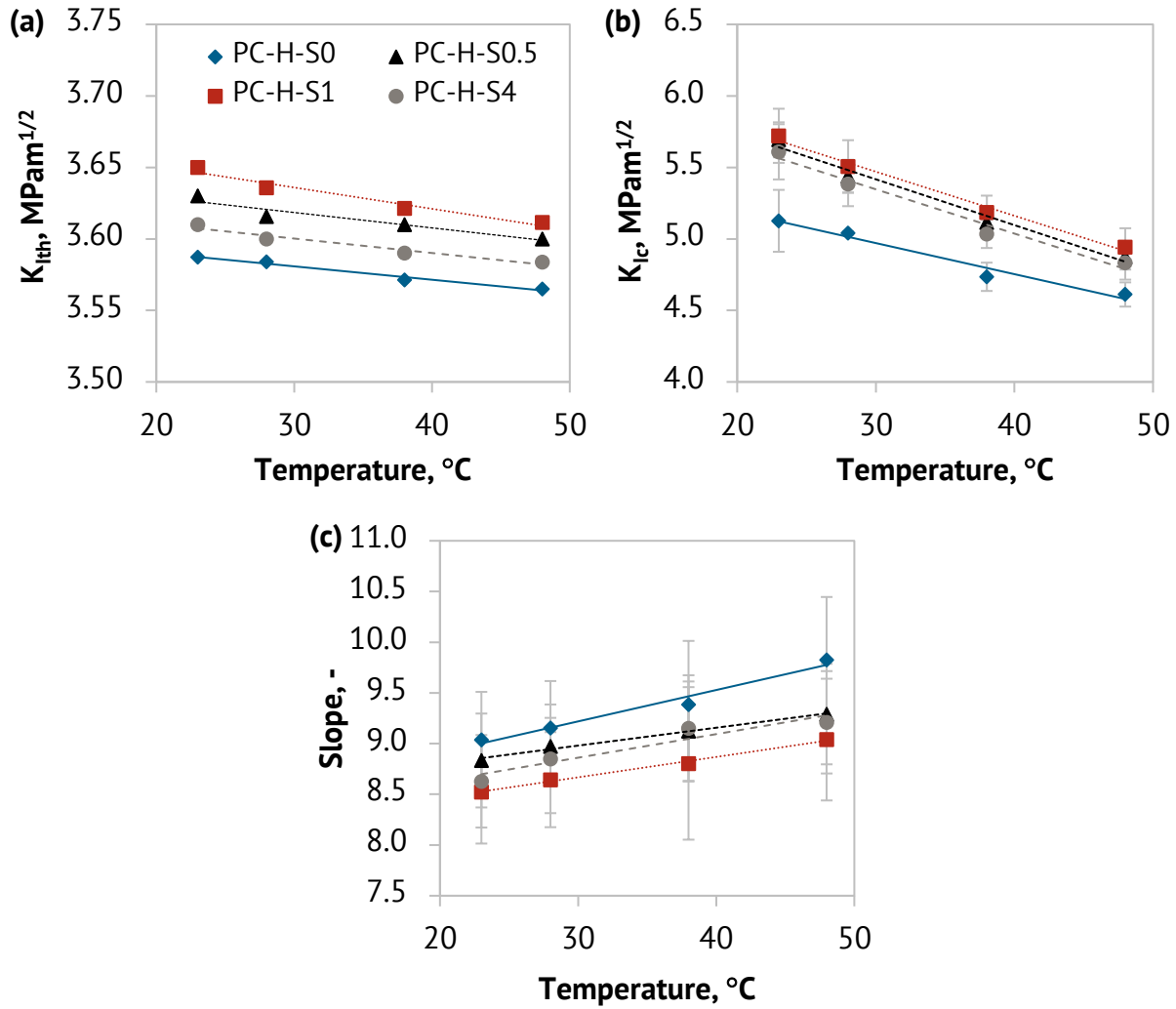
Figure 4.38: K_{Ith}, K_{Ic}, and slope of curve in stable crack growth region as a function of the temperature of PC nanocomposites in isopropanol.

The degree of ESC resistance deterioration due to the temperature effect can be described by using an Arrhenius equation, as follows:

$$k = Ae^{-\frac{E_a}{RT}} \tag{4.3}$$

where k = Rate constant

A = A constant for a given reaction

E_a= Activation energy

R = Gas constant (8.3145 J/mol·K)

T = Temperature (Kelvin)

Figure 4.39 represents the Arrhenius plot of ln K_{Ic} of PC nanocomposites in different ESC agents as a function of inverse temperature. In agreement with the Arrhenius relation,

the ln K_{Ic} of both PC and PC nanocomposites increases linearly with the inverse temperature in all investigated fluids. The activation energy (E_a) of each material can be calculated from the slope of the fitting straight-line, and these values are summarized in Table 4.2. It can be seen from Figure 4.40 that the estimated value of the K_{Ic} at different temperatures of the PC nanocomposites by using equation 4.3, demonstrates linear dependence on the experimental data. This results confirm that the proposed equation enables to predict the ESC behavior as a function of temperature in PC-based nanocomposites for different investigated fluids. In this logic, it is possible to use this approach to accelerate a long-term cracking test, particularly for slow crack growth behavior as in mild agents. The value of K_{Ic} in a long-duration cracking test at room temperature can be determined from short term experiment at a higher temperature which allows us to reduce the testing time.
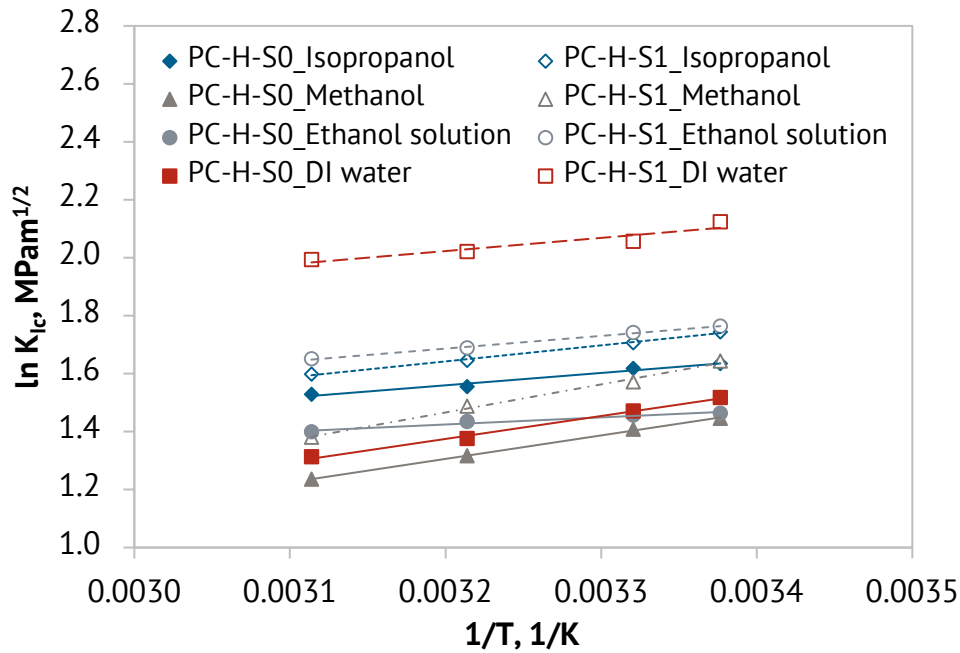
Figure 4.39: Arrhenius plot of ln K_{Ic} as a function of inverse temperature of PC and PC nanocomposites (1 vol.% nano-SiO_2) in different ESC agents.

Table 4.2 Activation energy values for PC nanocomposites with different ESC agents

Materials	Activation energy (E_a), kJ/mol			
	Isopropanol	Methanol	Ethanol solution	DI water
PC-H-S0	3.544	6.735	2.036	6.576
PC-H-S0.5	4.833	8.400	3.997	2.298
PC-H-S1	4.599	8.050	3.652	3.780
PC-H-S4	4.726	7.848	4.320	2.418
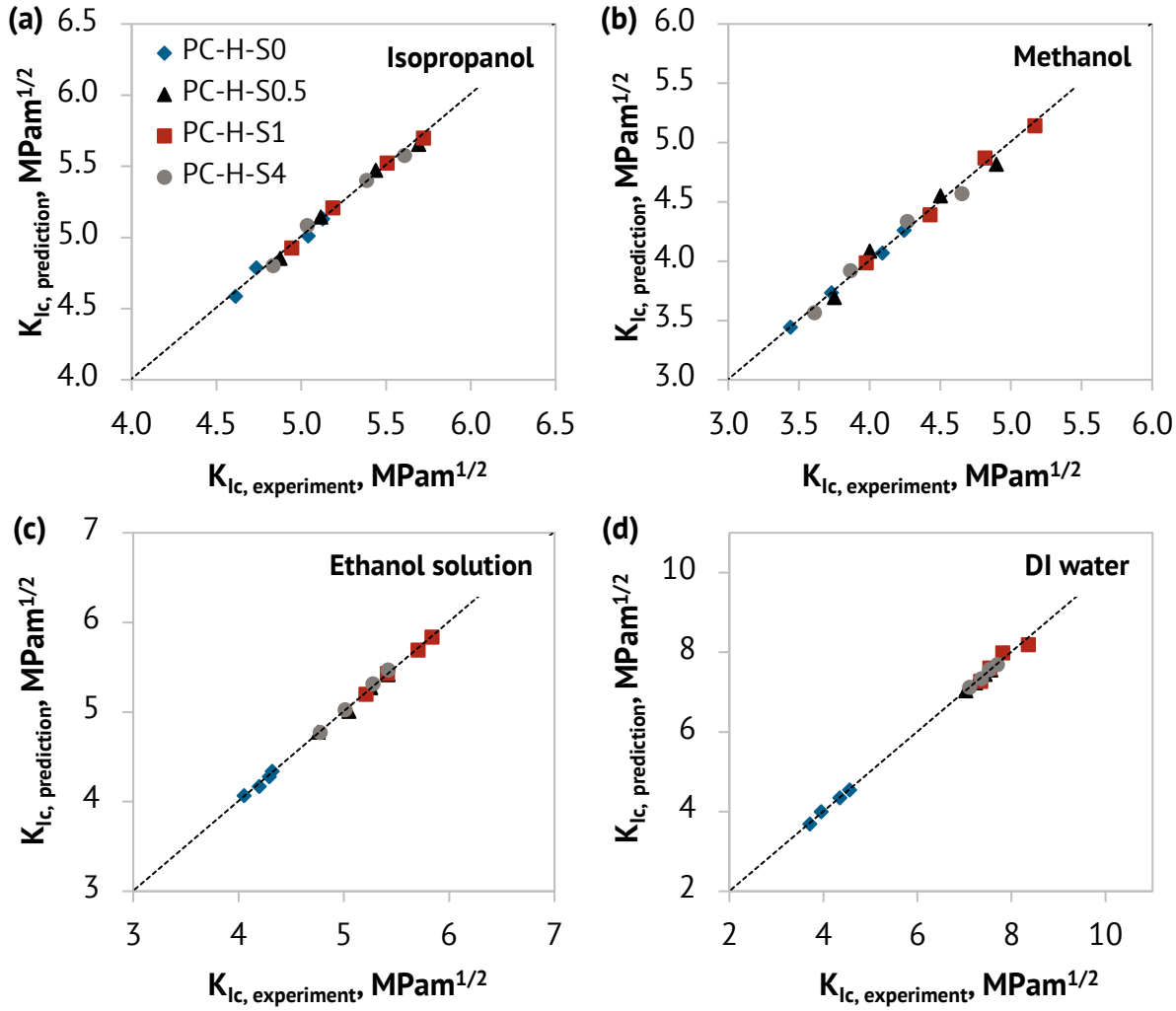
Figure 4.40: Correlation between estimated result from the Arrhenius equation and experimental data at different temperatures of PC based nanocomposites in different ESC agents: (a) isopropanol, (b) methanol, (c) ethanol solution and (d) DI water.

4.1.5.9 Prediction of ESC Behavior of PC nanocomposite using supposition approach

As discussed earlier, the analysis of long-term damage mechanisms, such as ESC resistance in mild agents, takes a long time under normal circumstances. Therefore, an accelerated testing method that involves increasing the tested temperature based on the superposition principle is an alternative method for predicting the ESC behavior of these materials. Adapted from the time-temperature superposition principle (Figure 2.14), the master curves of crack propagation models are constructed by shifting the crack propagation rate horizontally (in the region of stable crack growth) at various temperatures (T) to a reference temperature (T_{Ref}), using a shift factor (a_T), as described schematically in Figure 4.41 and equation 4.4. An empirical equation called the Williams–Landel–Ferry (WLF) equation is commonly used to calculate the temperature-dependent shift factor a_T

for amorphous polymers, as shown in equation 4.5 [80]. The corresponding dependence of the shift factor on the temperature calculated from equation 4.5 is shown in Figure 4.42.

$$da/dt(T, K_I) = da/dt(T_{Ref}, K_I/a_T) \tag{4.4}$$

$$log\,a_T = \frac{-C_1 \cdot (T - T_{Ref})}{C_2 + T - T_{Ref}} \tag{4.5}$$

where C_1, C_2 = Material constant values
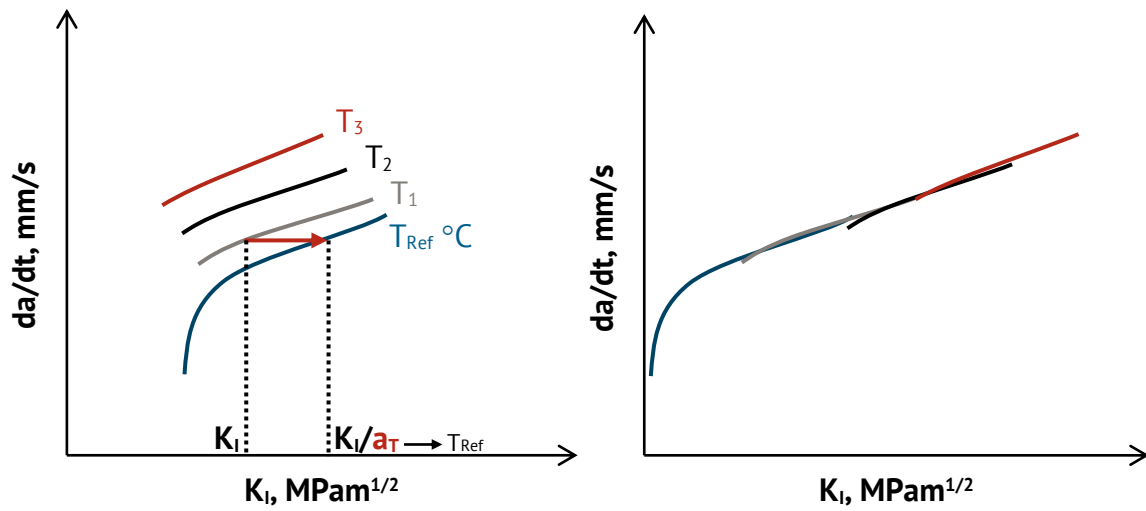
Figure 4.41: Schematic of curve shifting according to the modified superposition approach with crack propagation behavior.
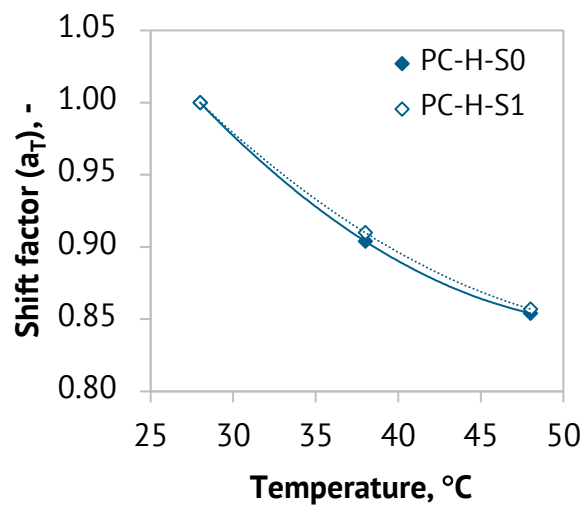
Figure 4.42: Shift factors for PC and PC nanocomposite in isopropanol; T_{Ref}=28°C.

A plot of the deformation process of the master curve and the results of the experiment involving neat PC and PC nanocomposites tested at different temperatures in isopropanol

is presented in Figure 4.43. It can be clearly seen that the obtained master curve shows very good agreement with the deformation behavior of the materials at room temperature. Therefore, the same underlying failure mechanism between the master curve and experiment can be assumed.
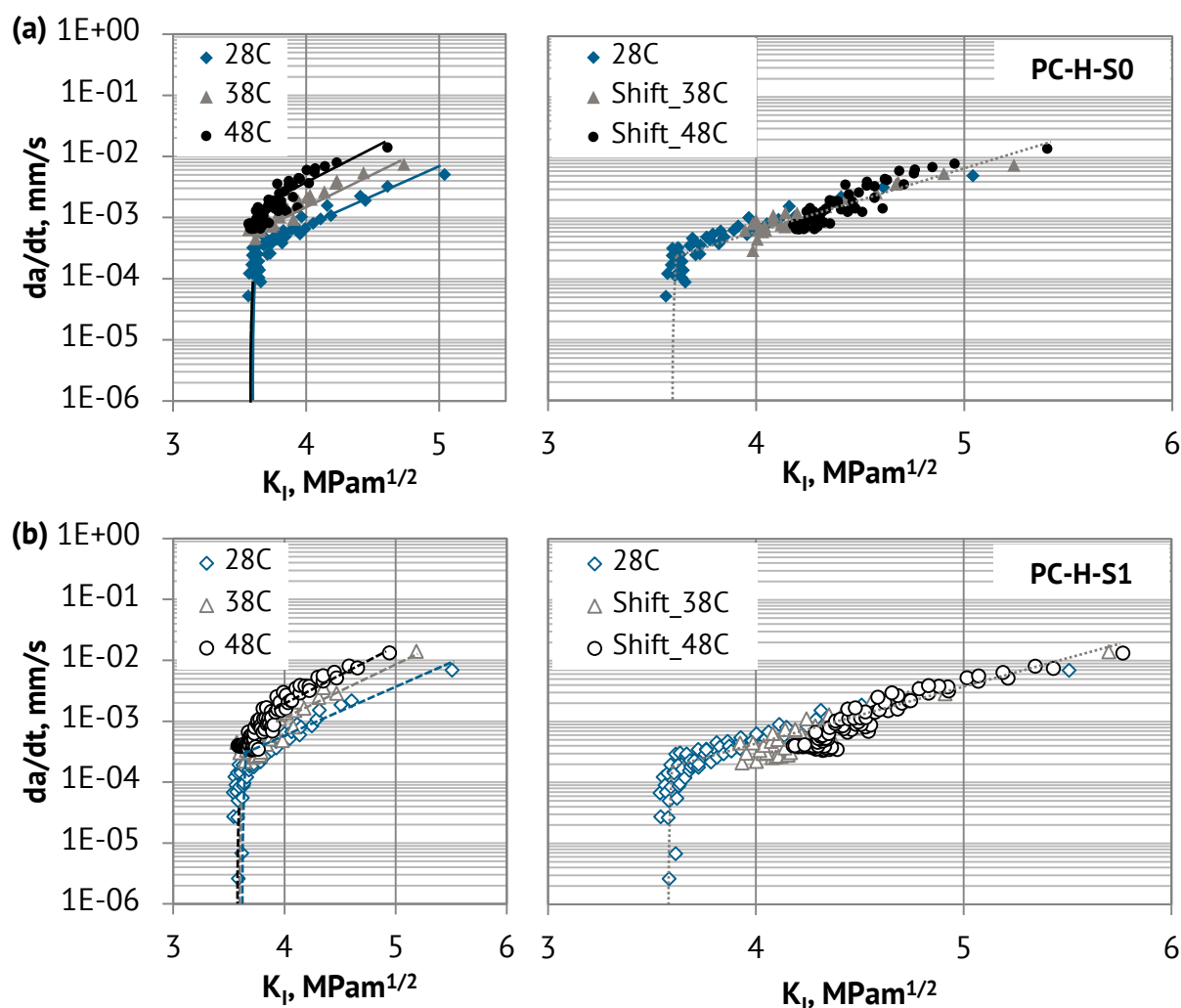
Figure 4.43: Crack propagation behavior of (a) PC and (b) PC nanocomposite at different temperatures and their master curves; T_{Ref}=28°C.

Additionally, it can also be observed that the master curves for the deformation process in all investigated fluids agree well with the results of existing ESC resistance tests at room temperature, as shown in Figure 4.44. The tendency of the ESC resistance curve is similar to the experimental results, which depends on the difference in the solubility parameters of the ESC agent and polymer and the molar volume of ESC agents. As shown in Figure 4.45, the estimated values for K_{Ith}, K_{Ic} and the slope of curve in the stable crack growth region from the master curve shows an appropriate linear dependence on the

experimental data. The good reproducibility of the construction of the master curves in-
dicates that the superposition approach is a suitable comparative method that could be
of great assistance in predicting the stress cracking behavior, especially for long-term
cracking tests in mild agents, allowing the testing time to be minimized.
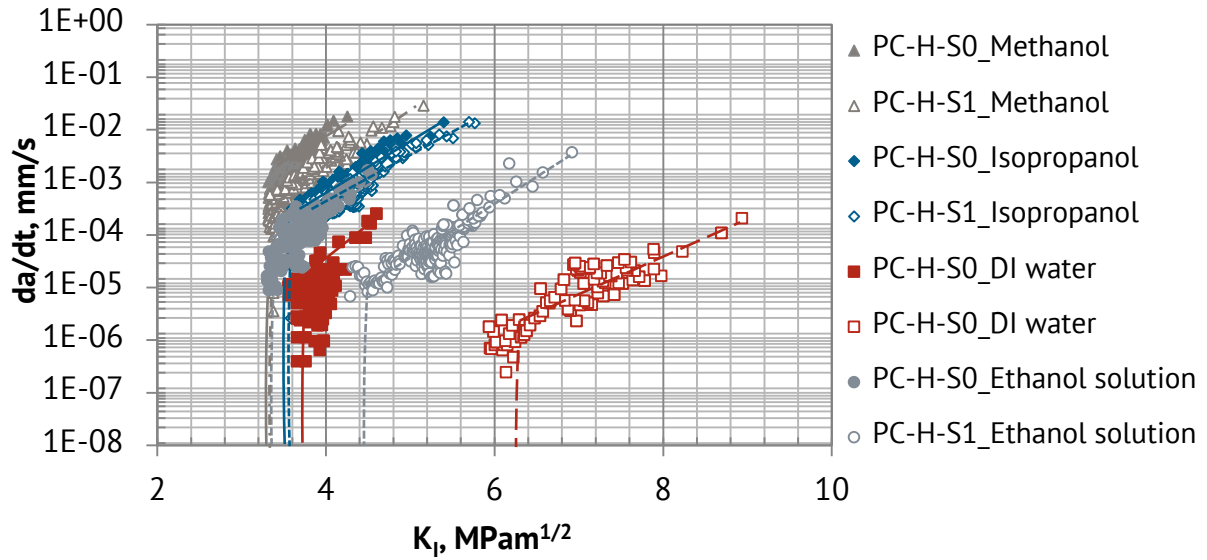
Figure 4.44: Master curves of PC nanocomposites with different ESC agents; T_{Ref}=28°C
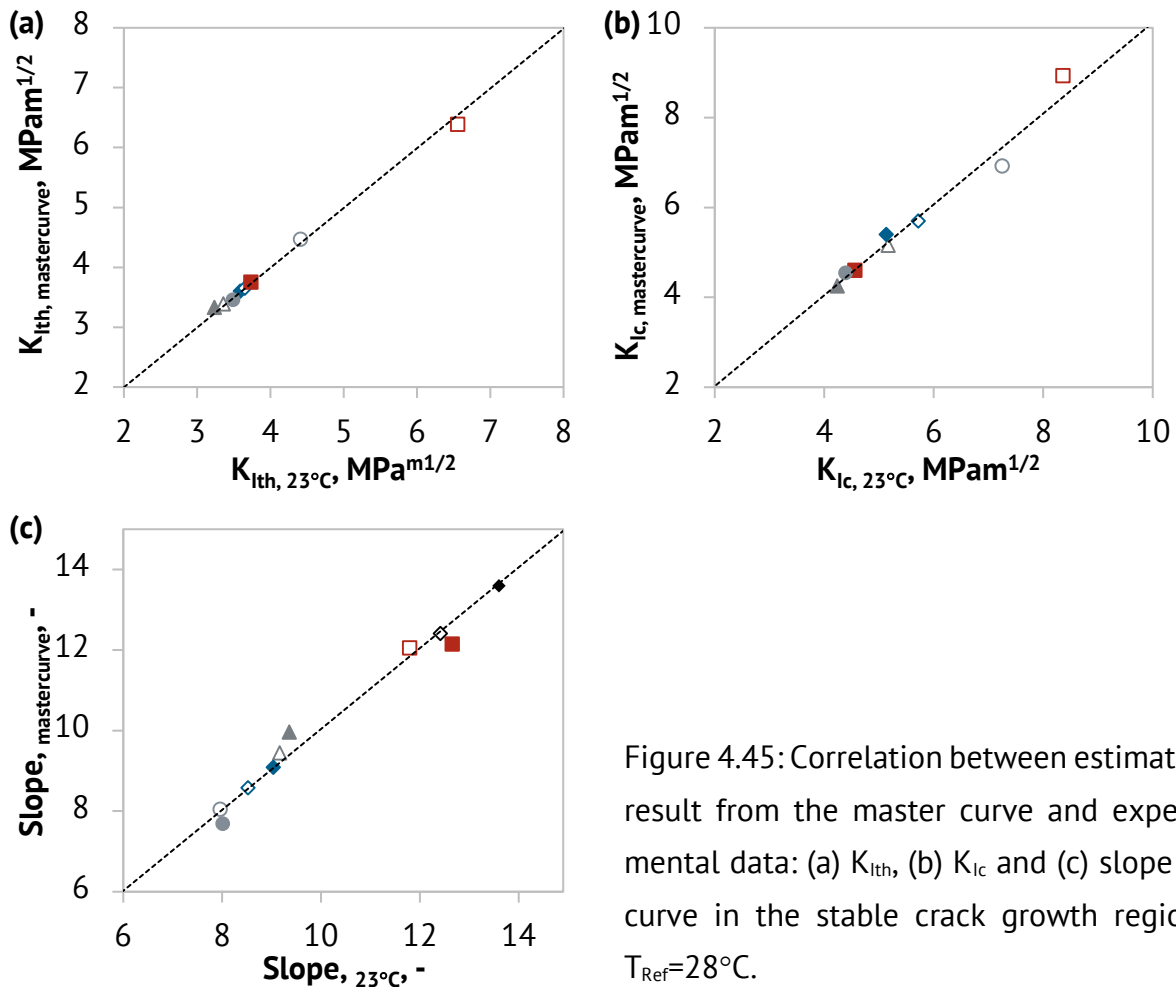
Figure 4.45: Correlation between estimated result from the master curve and experimental data: (a) K_{Ith}, (b) K_{Ic} and (c) slope of curve in the stable crack growth region; T_{Ref}=28°C.

4.1.5.10   Modeling and Simulation of Fracture Behavior

As is well-known, a numerical simulation with a complement of theory and experiment is a useful tool for understanding and predicting a failure phenomenon in materials. In this research, the modeling and simulation of fracture behavior with and without the liquid diffusion effect are performed, using commercial finite element method (FEM) software.

Modeling and Material Parameters for Simulation of Liquid Diffusion

As aforementioned, the process of macroscopic brittle crack formation in ESC failure depends on the diffusion process of the ESC agents into the polymer. Therefore, the modeling and simulation of the diffusion behavior of liquid (ESC agents) was firstly performed and compared with the liquid diffusion results discussed in section 4.1.5.1. However, liquid diffusion modeling tools are not available in most commercial FEM software. In this study, the analysis of liquid diffusion is carried out via a simulation using the analogy of a general function for thermal transfer, due to their equivalent mathematical structures [107,108]. Both of these processes are physical phenomena involving molecules equilibrating as a result of changes in temperature or liquid concentration, which can be explained as in the schematic drawing in Figure 4.46. According to Crank and Park [109,110], the fundamental concepts of the mass transfer in the diffusion process are comparable with those for heat conduction in an isotropic medium; which is described by Fick's law and Fourier's law, as shown in equations 4.6 and 4.7−4.8, respectively. Moreover, a swelling strain induced by liquid absorption can be also compared to the strain caused by thermal expansion of the material [111], as shown in Figure 4.47 and equations 4.9 and 4.10, respectively. An overview of the analogous material parameters for liquid diffusion that are equivalent to the heat transfer parameters applied in the model is given in Table 4.3. Based on the actual conditions of the experiments, the geometry of the cantilever beam and the initial pre-crack located at the middle of the specimen is modeled, as shown in Figure 4.48.

(a) Liquid diffusion
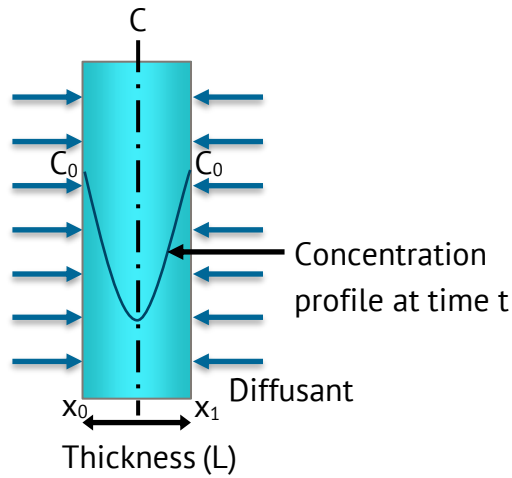
(b) Heat conduction

Fick's law of diffusion

$$J = -D\frac{\partial C}{\partial x} \qquad (4.6)$$

Fourier's law of heat conduction

$$q = -k\frac{\partial T}{\partial x} \qquad (4.7)$$

$$\alpha = \frac{k}{\rho C_p} \qquad (4.8)$$

where

J = Rate of transfer per unit area

C = Concentration of diffusing substances

x = Distance ($\sim L$, thickness)

$\dfrac{\partial C}{\partial x}$ = Gradiant of the concentration along the axis

D = Diffusion coefficient

where

q = Heat flux

k = Thermal conductivity

T = Temperature

x = Distance ($\sim L$, thickness)

$\dfrac{\partial T}{\partial x}$ = Gradiant of the temperature along the axis

α = Thermal diffusivity

ρ = Density

C_p = Specific heat capacity

Figure 4.46: Schematic explanation and its related equation of the equivalent process of (a) liquid diffusion and (b) heat conduction.

(a) Liquid diffusion expansion
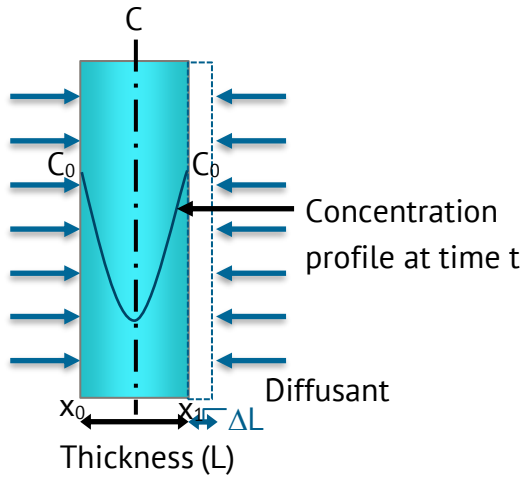
(b) Thermal expansion
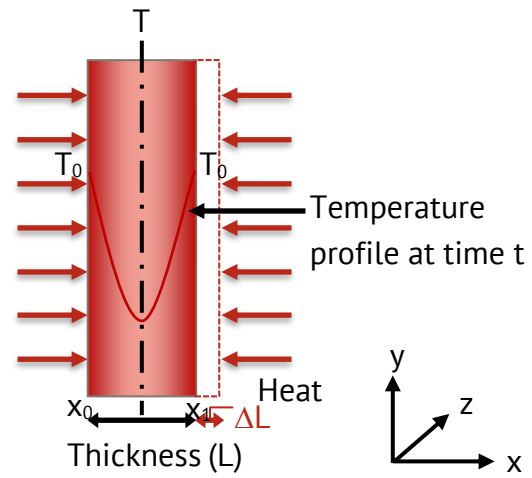
Liquid diffusion expansion

$$\frac{\Delta L}{L} = \beta \Delta C \qquad (4.9)$$

where

ΔL = Dimensional change

β = Coefficient of expansion (swelling)

ΔC = Concentration different

Thermal expansion

$$\frac{\Delta L}{L} = \alpha \Delta T \qquad (4.10)$$

where

ΔL = Dimensional change

α = Coefficient of thermal expansion

ΔT = Temperature different

Figure 4.47: Schematic explanation and its related equation of (a) liquid diffusion expansion and (b) thermal expansion.

Table 4.3 Material parameters for liquid (ESC agents) diffusion simulation using thermal transfer analogy

Parameters	DI water		Isopropanol		Methanol	
	PC-H	PC-H-S1	PC-H	PC-H-S1	PC-H	PC-H-S1
Saturated concentration ($\approx$saturated temperature), %	0.329	0.335	0.092	0.096	3.149	3.156
Diffusion coefficient ($\times 10^{-12}$) ($\approx$thermal conductivity), m^2/s	4.684	3.294	0.288	0.234	0.348	0.288
Coefficient of expansion ($\approx$Coefficient of thermal expansion), /%	0.384	0.377	0.544	0.509	0.488	0.486

Note: In this model, the specific heat capacity and density = 1; thermal diffusivity $\approx$ thermal conductivity. The coefficient of expansion due to liquid absorption is determined based on the method described in [111].
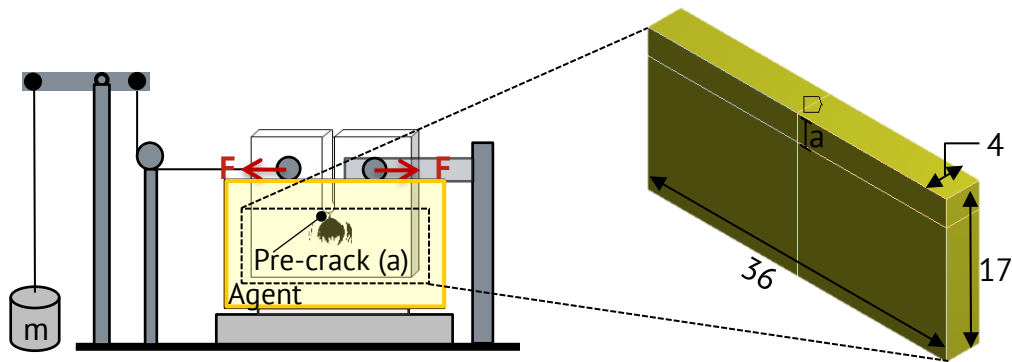
Figure 4.48: Geometry and dimension of the cantilever beam (unit: mm).

By using FEM analysis, the graphical profile of the liquid content distribution (in the middle cut plane) for various immersion times of neat PC in DI water is shown in Figure 4.49. As expected, the body of the specimen gradually absorbs the liquid from the surrounding outer surface, and this liquid content increases as a function of immersion time following Fick's law, as shown in Figure 4.50. Interestingly, the profile of the absorbed liquid content obtained from simulation agrees well with the experimental results of the absorption tests for all investigated ESC agents, ensuring accurate prediction of the developed model. As is well-known, this liquid diffusion can induce swelling in the polymeric materials and cause the development of stress, resulting premature failure. For this reason, the distribution profile of the absorbed liquid within the specimen obtained from the diffusion model is applied in the fracture analysis in the following section.
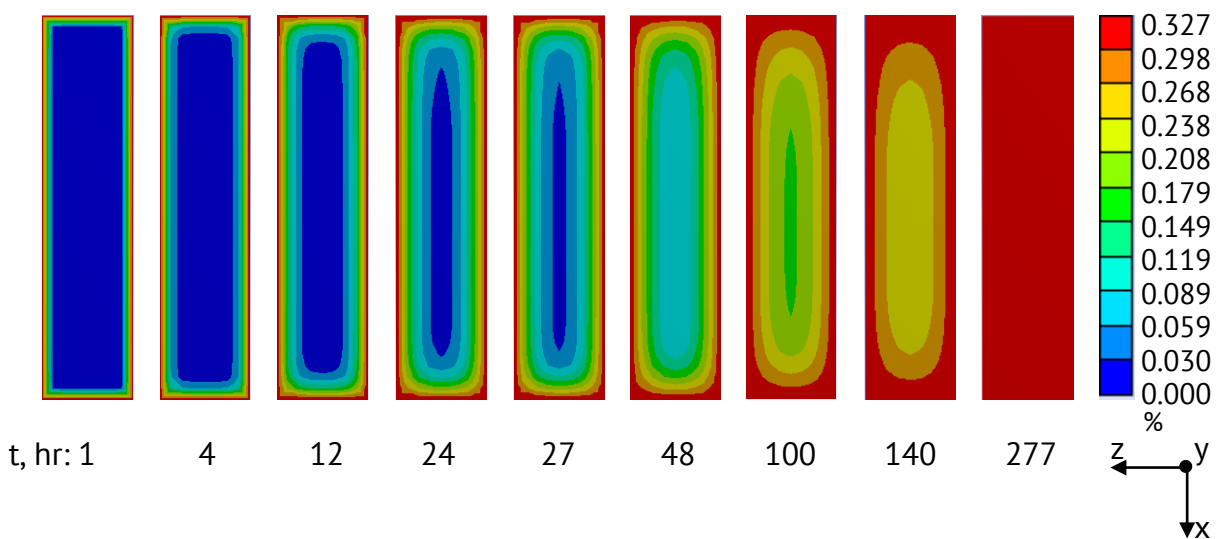
Figure 4.49: Profile of liquid content obtained from the simulation at various exposure times in DI water.
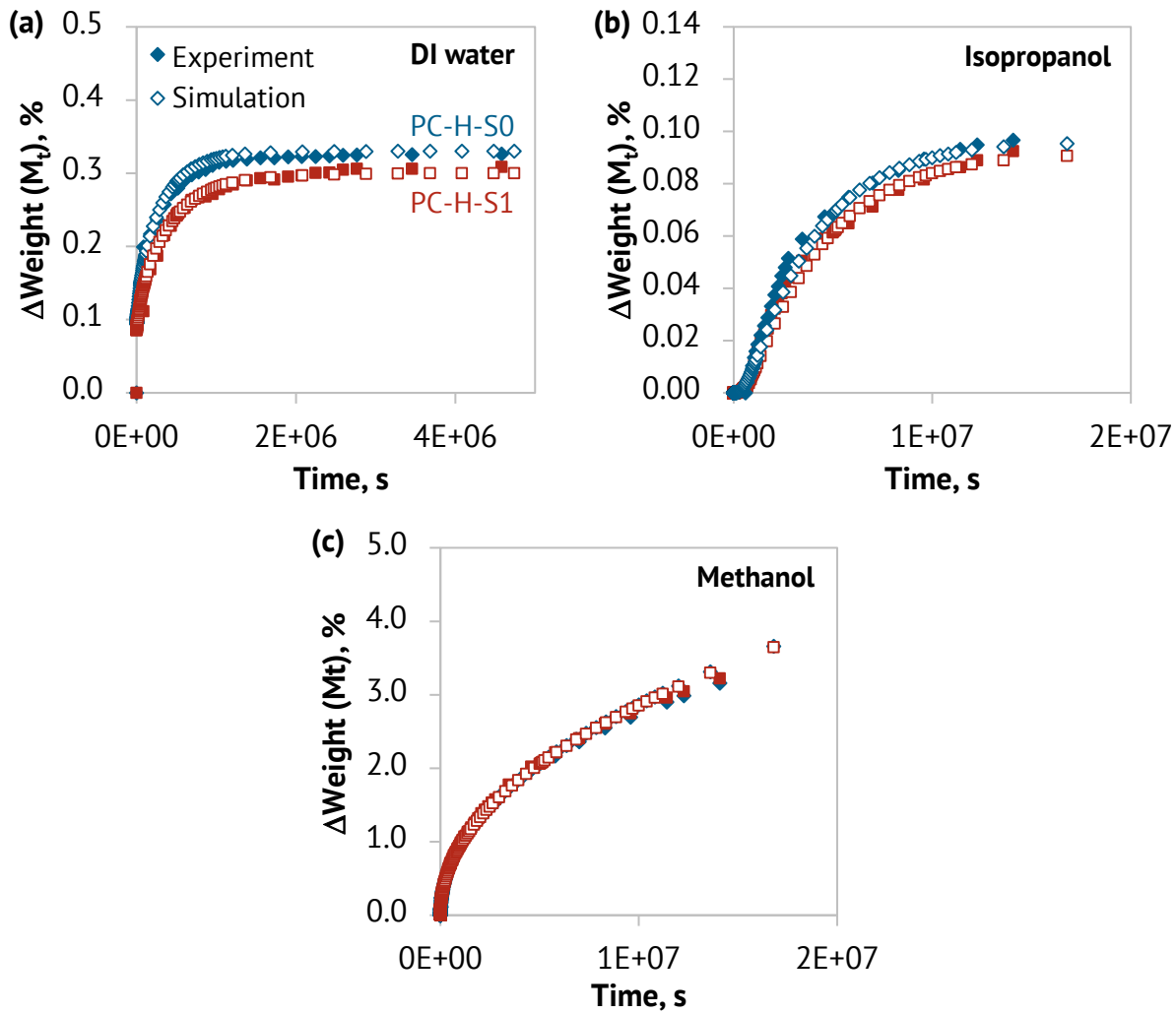
Figure 4.50: Profile of liquid content obtained from absorption experiment and simulation at various exposure times in different ESC agents: (a) DI water, (b) isopropanol and (c) methanol.

Modeling and Material Parameters for Simulation of Fracture Behavior

It should be noted that two processes are involved in the fracture simulation. Firstly, the critical strain energy release rate (G_{Ic}), which is the energy required for crack initiation at a certain crack length, is determined and used to calculate the stress intensity factor (K_I) using equation 2.19. Then, this fracture criterion is applied in the static-fracture analysis with a compact tension (CT) specimen to determine the actual crack propagation behavior and the critical stress intensity factor (K_{Ic}) of different materials.

By using a structural-mechanical function, the G_{Ic} of cantilever beams in mode tension (mode I) is determined using a virtual crack closure technique (VCCT). In this fracture model, linear-elastic material deformation is assumed and a pre-meshed crack is defined, as shown in Figure 4.51. An overview of the material parameters used in the fracture

simulation is given in Table 4.4. For the fracture analysis with liquid diffusion consideration, the distribution of the absorbed liquid content within the specimen body is first solved by the developed diffusion model, and the liquid content profile (as input data) is then substituted into the fracture analysis.
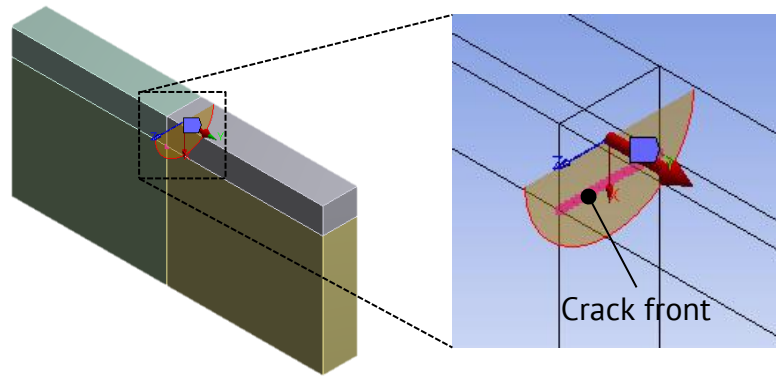
Figure 4.51: The cantilever beam with a defined pre-meshed crack in a fracture model.

Table 4.4: Material parameters for simulation

Designation	Density (ρ), kg/m^3	Modulus (E), MPa	Poisson ratio (v), -	Yield strength (σ_y) MPa
PC-H-S0	1200	2311	0.37	66
PC-H-S1	1208	2440	0.37	69

To determine the fracture behavior related to the actual experiment, a standard CT specimen is modeled with the same geometry and dimensions, as shown in section 3.6.3. Pre-meshed crack characteristics, such as a crack front and crack surfaces, are defined as shown in Figure 4.52(a). It should be noted that the numerical analysis of the mechanical fields of a cracked part is strongly influenced by the meshing quality in the vicinity of the crack tip. Therefore, a mesh refinement with a sphere of influence scoped to the crack-tip area is applied, as seen in Figure 4.52(b). The fracture model assumes Mode I (tension) for crack propagation, with static load conditions that are related to the actual experiment. As mentioned earlier, the estimated values of K_I (from the cantilever beam model) with and without liquid diffusion are applied as cracking criteria in this fracture model analysis. Then, the crack growth is computed according to the Paris' law, as described in section 2.2.5. For more accurate of crack propagation analysis, the SMART crack growth features in ANSYS Mechanical are used for the simulation, as these enable for separating, morphing, adaptive meshing and re-meshing during fracture modeling.
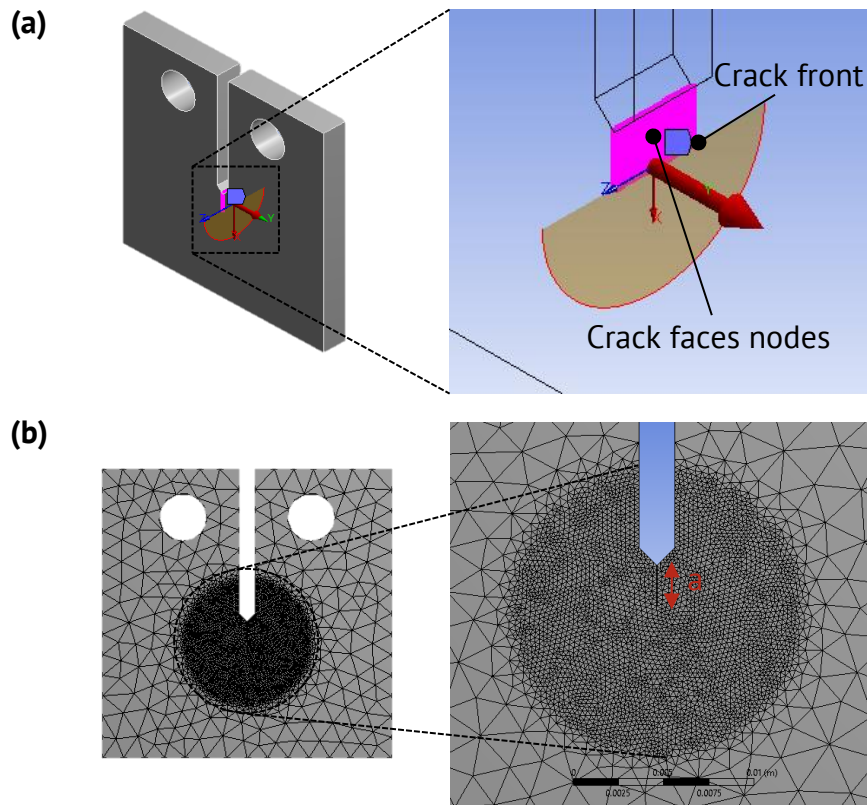
Figure 4.52: Details of fracture analysis model: (a) pre-meshed crack set-up and (b) mesh refinement.

Figure 4.53 presents the simulation results for the cantilever beam model in terms of the critical strain energy release rate (G_{Ic}) and its corresponding intensity factor (K_I) for neat PC and PC/SiO$_2$ nanocomposites. The values of G_{Ic} and K_I required for crack initiation of the PC nanocomposites are greater than those for neat PC, both with and without liquid exposure, indicating a higher fracture resistance for nanocomposite materials. Moreover, it can be seen that the exposure of materials to stress cracking agents such as methanol, isopropanol, and DI water can lower the fracture resistance of both PC and PC nanocomposites. This finding is consistent with experimental results from ESC tests. This result suggests that the modeling of the diffusion process linked with the structural fracture model is capable for solving multi-field problems.
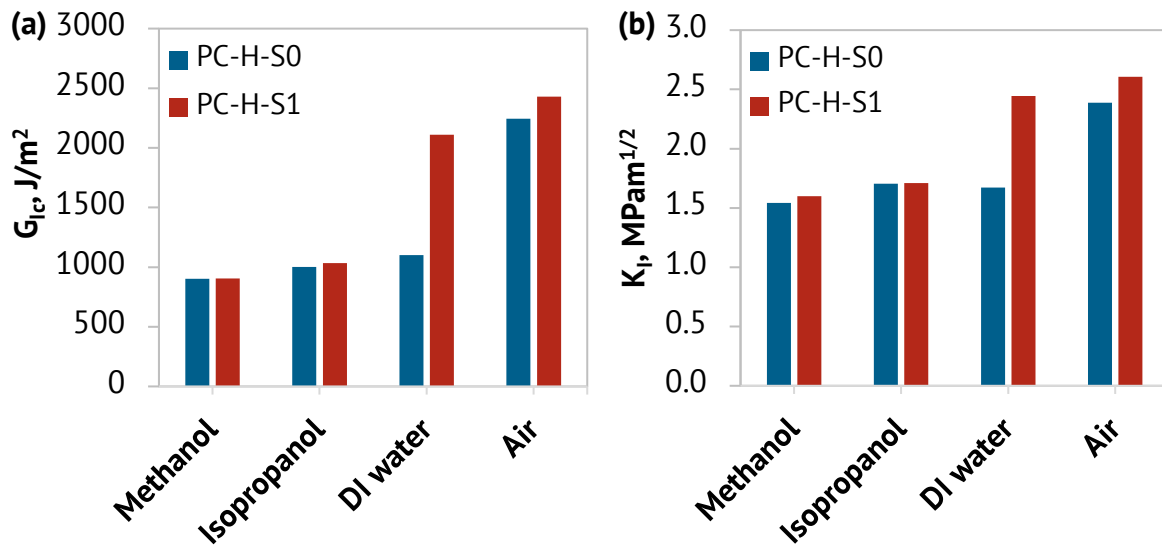
Figure 4.53: (a) G_{Ic} and (b) K_I of neat PC and PC/SiO$_2$ nanocomposite simulated with and without considering the liquid diffusion.

By using the cracking criteria from the previous model, the results of the von Mises stress distribution in the CT specimen under static loading are presented in Figure 4.54. As can be clearly seen, the maximum von Mises stress occurs in the vicinity of the crack tip (the red zone), which is in agreement with the well-known theory of fracture mechanics. A sharp crack tip acts as a stress intensifier, which results in the development of high stresses around the crack tip and locally yields the material referred as the "plastic zone." According to Irwin [64], the stress state at a crack tip can be described by a stress intensity factor. As discussed earlier, the crack starts to propagate if the applied K_I is higher than that of threshold K_{Ith}, and the unstable crack propagation begins if the applied K_I is reached the critical K_{Ic}. Then, the material fractures in a right short time.
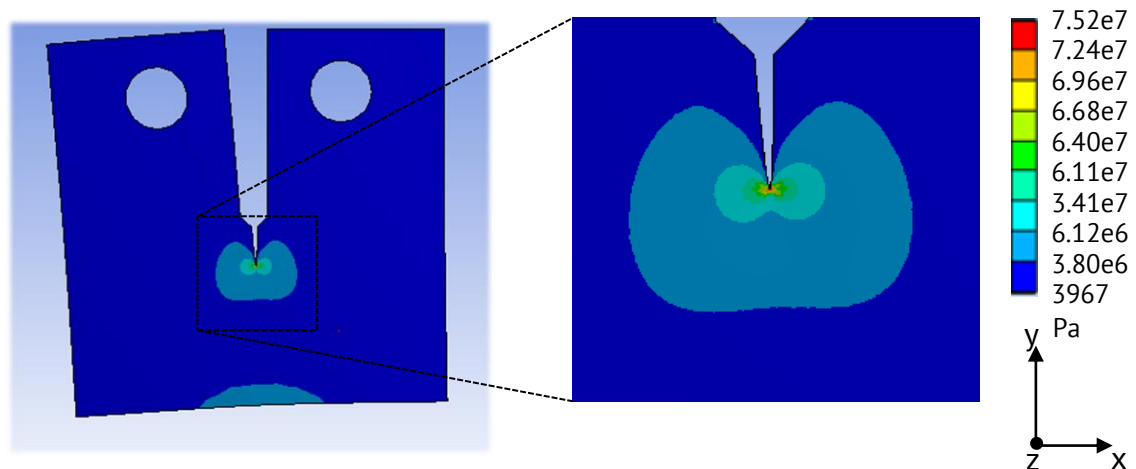
Figure 4.54: The stress fields around a crack tip of the PC-based material under static loading conditions.

Figure 4.55 shows a representative of crack length extension as a function of time in neat PC tested in air compared with experimental results. It is evident from the plots that the computed crack length extension agrees well with the experimental data. Based on this result, the crack propagation rate (da/dt) as a function of K_I factor can be used to determine the resistance of the material to crack propagation under static loading. As seen in Figure 4.55(b), the crack propagation behavior of neat PC in the stable crack growth regime (i.e., the Paris regime) constructed from FEM method agrees well with experimental results. Moreover, the estimated values of the critical stress intensity factor of different materials from the crack growth simulation are fairly consistent with experimental data for different tested agents (Figure 4.56). This finding indicates that the multi-field modeling can provide reasonable predictions for diffusion processes and their impact on fracture behavior in different stress cracking agents. This could be a great help in various application fields where the products particular risk to the ESC failure such as in medical care. The content of diffused chemical/drug along the thickness of product as a function of service time and their influence on stress cracking behavior can be simply simulated. As a result, the implemented model may be a useful tool for quick screening and mitigating the risk of ESC failures in the medical products, allowing to minimize the great expense for stress-cracking tests in medical industry.
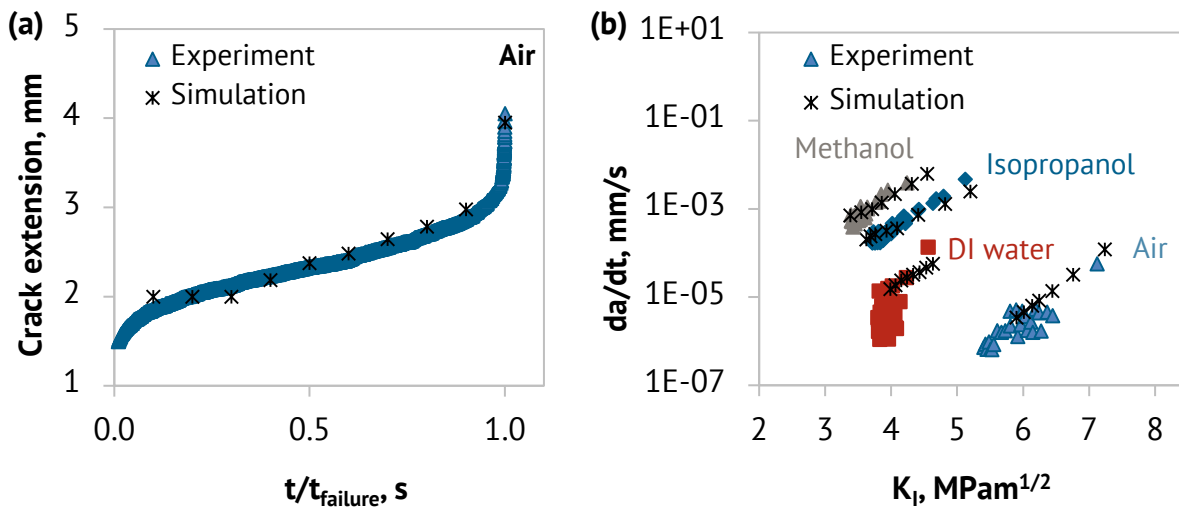
Figure 4.55: Comparison between experimental and simulation results of (a) crack extension as a function of time and (b) crack propagation as a function of K_I factor in the stable crack growth region.
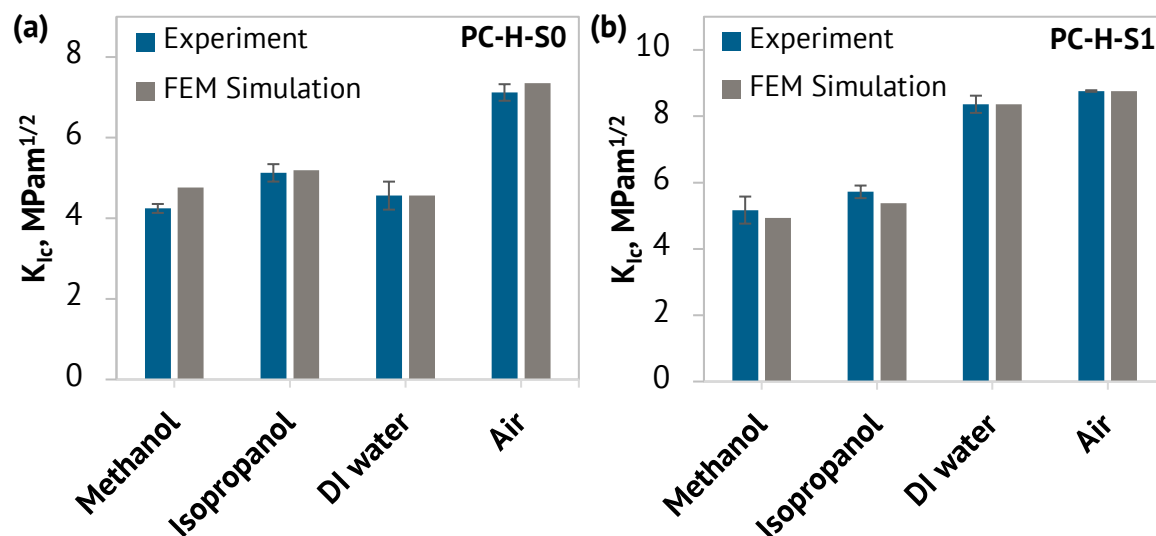
Figure 4.56: Comparison of K_{Ic} values between experimental data and simulation for (a) neat PC and (b) PC nanocomposites in different testing agents.

4.2 Polystyrene and Polymethyl Methacrylate Nanocomposites

4.2.1 Optical Properties

Representative images and quantitative evaluations of the optical properties of PS and PMMA nanocomposites containing different sizes and contents of nano-SiO_2 particles are shown in Figure 4.57 and 4.58, respectively. Similarly to PC, adding a small amount of nano-SiO_2 into PS and PMMA causes a reduction in material transparency due to light loss via reflection and scattering [83]. Increasing the content of the nano-SiO_2 results in a decrease of total light transmittance/clarity and an increase of haze of the materials.

Materials				
Neat polymer	S1 (7nm)	S1 (12nm)	S4 (7nm)	S4 (12nm)
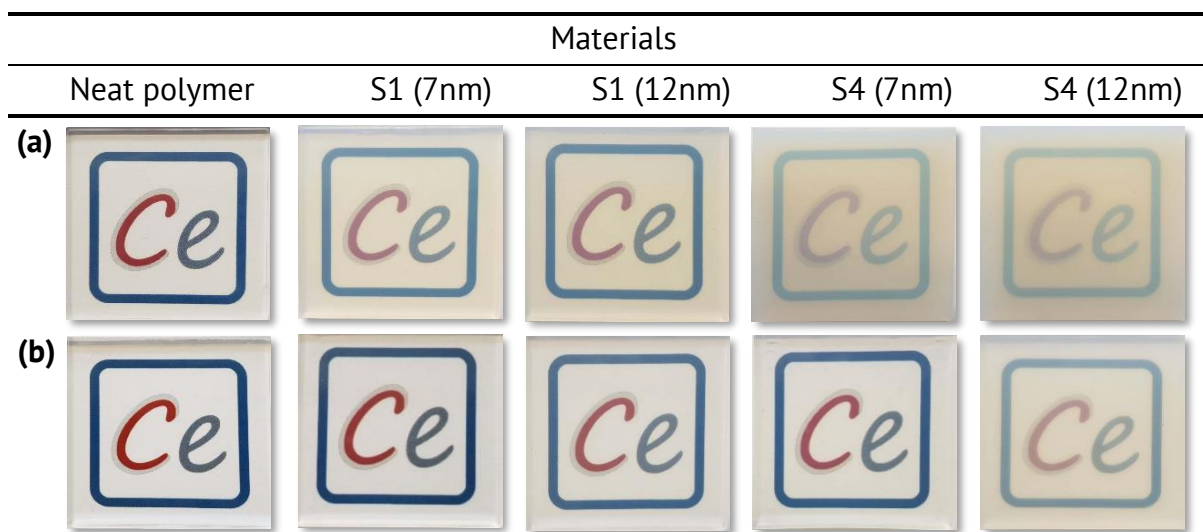
Figure 4.57: Representative images: (a) PS and (b) PMMA nanocomposites.

For a comparison of different amorphous polymer nanocomposites at a given nano-SiO_2 particle content, the transparency of the nanocomposites decreases in the following order: PMMA/SiO_2 > PS/SiO_2 > PC-L/SiO_2 > PC-H/SiO_2 (Appendix A). This is particularly relevant given the difference in the refractive indices between the polymer matrix and the particles. In this study, the differences in the refractive indices of PMMA/SiO_2, PS/SiO_2, and PC/SiO_2 are 0.04, 0.09, and 0.14 respectively. The relationship between the optical properties and the differences in the refractive indices of the nanocomposites is presented in Figure 4.58(d). It can be suggested that the difference in the refractive indices of the polymer matrix and the particles has more effect on the light transmittance and the haze of materials, while the particle size mainly influences the clarity and haze of the nanocomposites.
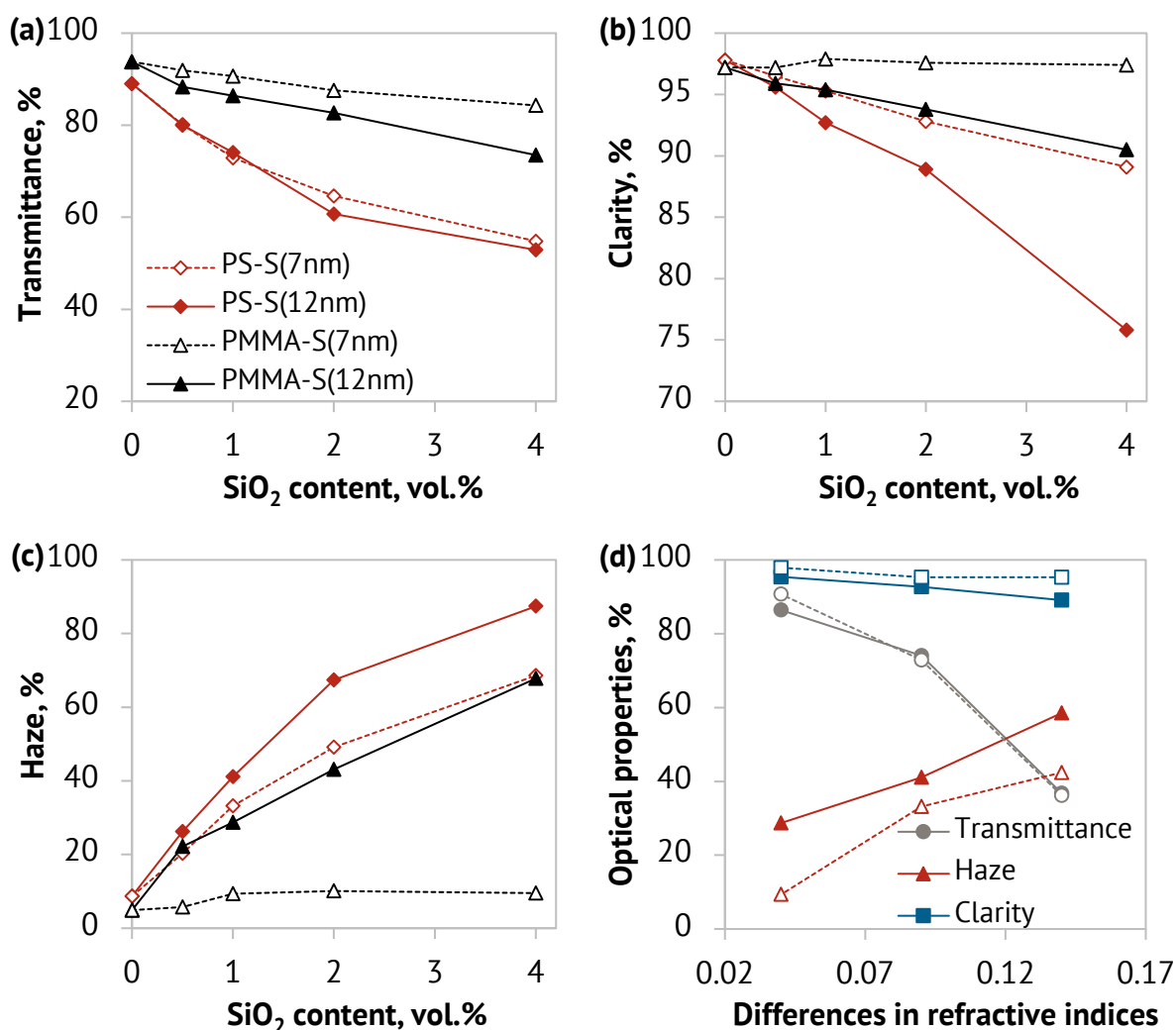
Figure 4.58: Optical properties of PS and PMMA nanocomposites filled with nano-SiO_2 of 7 nm (dash line) and 12 nm (solid line): (a) total light transmittance, (b) clarity, (c) haze as a function of particle contents and (d) optical properties of the polymer nanocomposites (1 vol.% nano-SiO_2) with respect to the difference in refractive indices.

4.2.2 Mechanical Properties

4.2.2.1 Tensile Properties

Tensile properties of the PS and PMMA nanocomposites are illustrated in Figure 4.59 (Appendix B and C). With the addition small amount of nano-SiO_2 into PS and PMMA, the elastic modulus and the tensile strength gradually increase. Obviously, the improvement in tensile strength is more pronounced with the incorporation of smaller nano-SiO_2 particles, due to the higher interfacial surface area, promoting the greater filler-matrix interactions which assure efficient stress transfer across the nanocomposite components. However, with a further increase in the nanofiller contents beyond 1 vol.%, the improvements in tensile strength are only marginal for PS nanocomposites, and even cause a decrease for PMMA nanocomposites, as seen in Figure 4.59(b). In terms of the elongation at break, PS and PMMA nanocomposites tend to be brittle materials that break at moderate and small strains. As opposed to PC nanocomposites, the elongation at break of the PS and PMMA nanocomposites is reduced with increasing nanofiller content, due to the decreased deformability of rigid interphase between the nanofiller and the matrix [112].
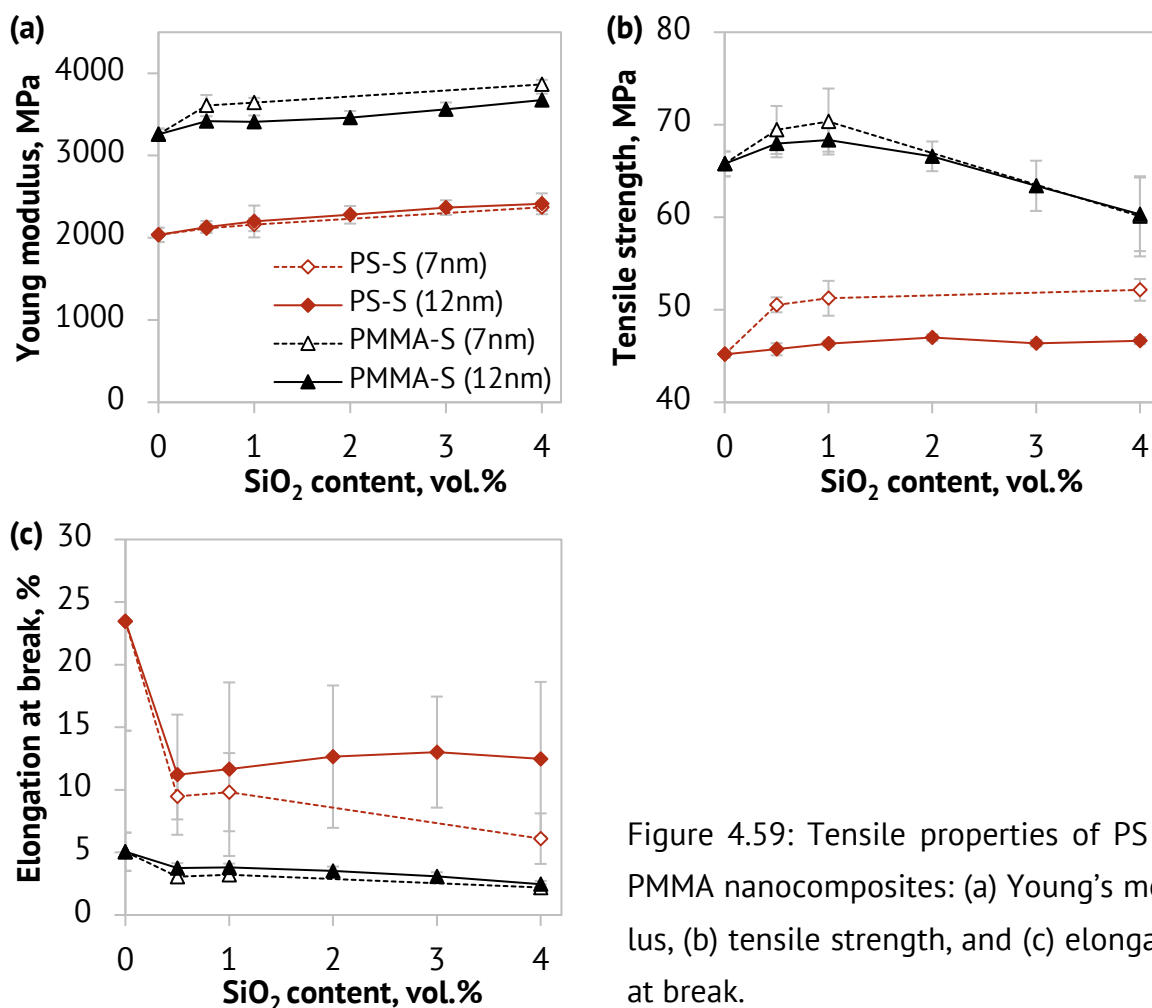
Figure 4.59: Tensile properties of PS and PMMA nanocomposites: (a) Young's modulus, (b) tensile strength, and (c) elongation at break.

4.2.2.2 Impact and Fracture Toughness Properties

The influences of nano-SiO_2 contents and sizes on the notched impact strength and the fracture toughness of PS and PMMA nanocomposites are presented in Figure 4.60(a) and (b), respectively (Appendix B and C). Unlike PC-based nanocomposites, an increase in the impact strength and fracture toughness of PS- and PMMA-based nanocomposites appears only with smaller particle size for a small amount of filler content (up to 1 vol.%). For a comparison of different amorphous polymer nanocomposites at a given nano-SiO_2 particle content, the toughness of nanocomposites increases in the following order: PMMA/SiO_2 < PS/SiO_2 < PC-L/SiO_2 < PC-H/SiO_2, which is related to the intrinsic toughness of the matrix. Moreover, the different levels of toughness improvement can possibly be explained by the differences in the thermodynamic affinity of the polymer matrix and nanoparticles. PC has a better thermodynamic affinity with hydrophobic nano-SiO_2 particles than PS and PMMA [113]. Thus, the interface of the PC matrix-filler has more favorable interactions, and these directly enhance the energy dissipation during the deformation process.
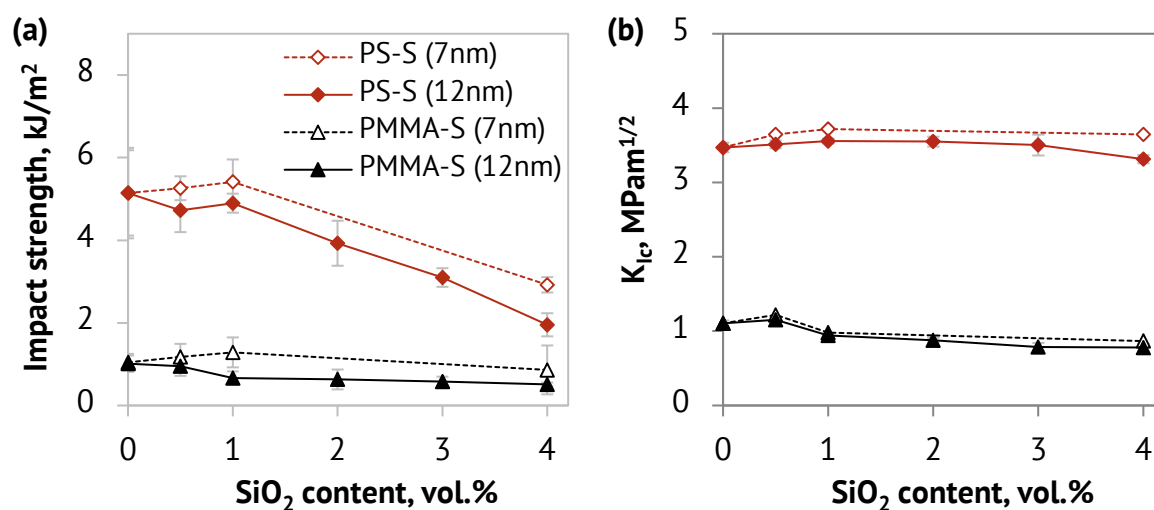
Figure 4.60: (a) Impact properties and (b) fracture toughness of PS and PMMA nanocomposites as a function of the filler contents and its particle sizes.

4.2.3   Thermal Properties

Generally, the differences in the values of glass transition temperature (T_g) of the amorphous polymer are observed due to the differences in backbone flexibility and side group bulkiness. The neat PS and PMMA which have bulky side groups exhibit a high value of T_g at about 105 and 100 °C, respectively. Figure 4.61 represents the effects of nanofiller concentrations and sizes on the T_g of PS and PMMA (Appendix D). It is seen

that the T_g of both PS and PMMA slightly increases with increasing nano-SiO_2 contents. This is attributed to the appropriate degree of filler-matrix interaction and the restriction of polymer chain movement caused by the nanoparticles. However, the size of nanofiller does not have a significant effect on the T_g of the materials.
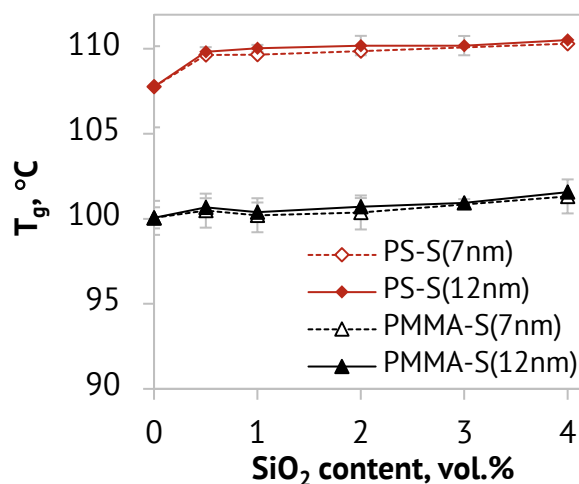
Figure 4.61: T_g of PS and PMMA nanocomposites as a function of filler contents and sizes.

4.2.4 Environmental Stress Cracking Properties

4.2.4.1 Effects of Nanofiller Content and Size

As demonstrated in section 4.1.5, the incorporation of nanofillers has been proven as an effective method to remarkably enhance ESC resistance in PC. Thus, it is of great interest to investigate whether the ESC resistance of other amorphous polymers, such as PS and PMMA, can also be positively influenced by nanoparticles. Accordingly, the ESC behavior of PS and PMMA-based nanocomposites was also investigated in different testing agents (isopropanol, methanol, and DI water) by using an identical fracture mechanic test method.

Figure 4.62 shows the material behavior, which is optically characterized by the crack growth and color (density) changes in front of the crack tip of PS and PMMA-based nano-composites in different ESC agents. The different shapes/types of areas in front of the macro-crack tip can be observed in different materials. A densely packed craze with one major direction followed by the radial craze bundle formed after sudden detachment of craze wedge is observed in PS immersed in alcohol agents. Doyle et al. [114] have suggested that under this behavior the materials exhibit a practically brittle type of fracture, which is normally found in PS. In mild agents and air, a much more voluminous damaged

zone appears in front of the crack-tip, indicating multiple deformation processes on a small scale, as previously discussed in the PC-based nanocomposites. Compared with other materials; the alcohol agents are the most severe to PMMA; the specimen is cracked immediately after exposure to alcohol. Therefore, the investigation of the ESC resistance of PMMA in alcohol agents could not be carried out in this study. One can see that almost sharp cracks are observed in the PMMA after exposed to mild agents and air, suggesting the brittle fracture mechanisms. However, the deformed pattern of both PS and PMMA is not affected by the incorporation of nanofiller.
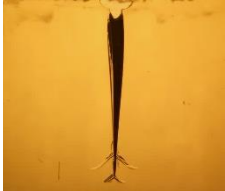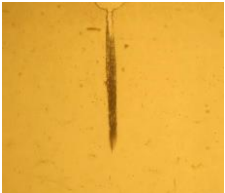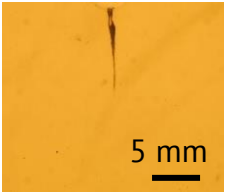
Materials	PS	PS/SiO$_2$ 1 vol.%	PMMA	PMMA/SiO$_2$ 1 vol.%
Isopropanol				
Methanol			Break immediately after exposure to alcohol agents	
DI water				
Air				5 mm

Figure 4.62: Digital images before failure of PS and PMMA nanocomposites in different ESC agents.

The influences of nano-SiO$_2$ content and size on the K_{Ith} and K_{Ic} of PS and PMMA-based nanocomposites are shown in Figures 4.63(a)-(b) and (c)-(d), respectively (Appendix K and L). Similar to PC, the incorporation of nano-SiO$_2$ into PS and PMMA is also useful in improving the ESC resistance of the materials. An enhancement of the K_{Ith} and K_{Ic} are

observed with the presence small amount of nano-SiO_2, especially for smaller size particles. This confirms the earlier result that the nanoparticles and their agglomerates promote the formation of energy dissipative structures, which can effectively dissipate energy during the fracture process, thereby increasing the ESC resistance of the nanocomposites. It should be noted that, in alcohol agents, the enhancement of ESC resistance in terms of failure time is considered more attractive than the increase of K_{Ic} value of the materials, as seen in Figure 4.64.
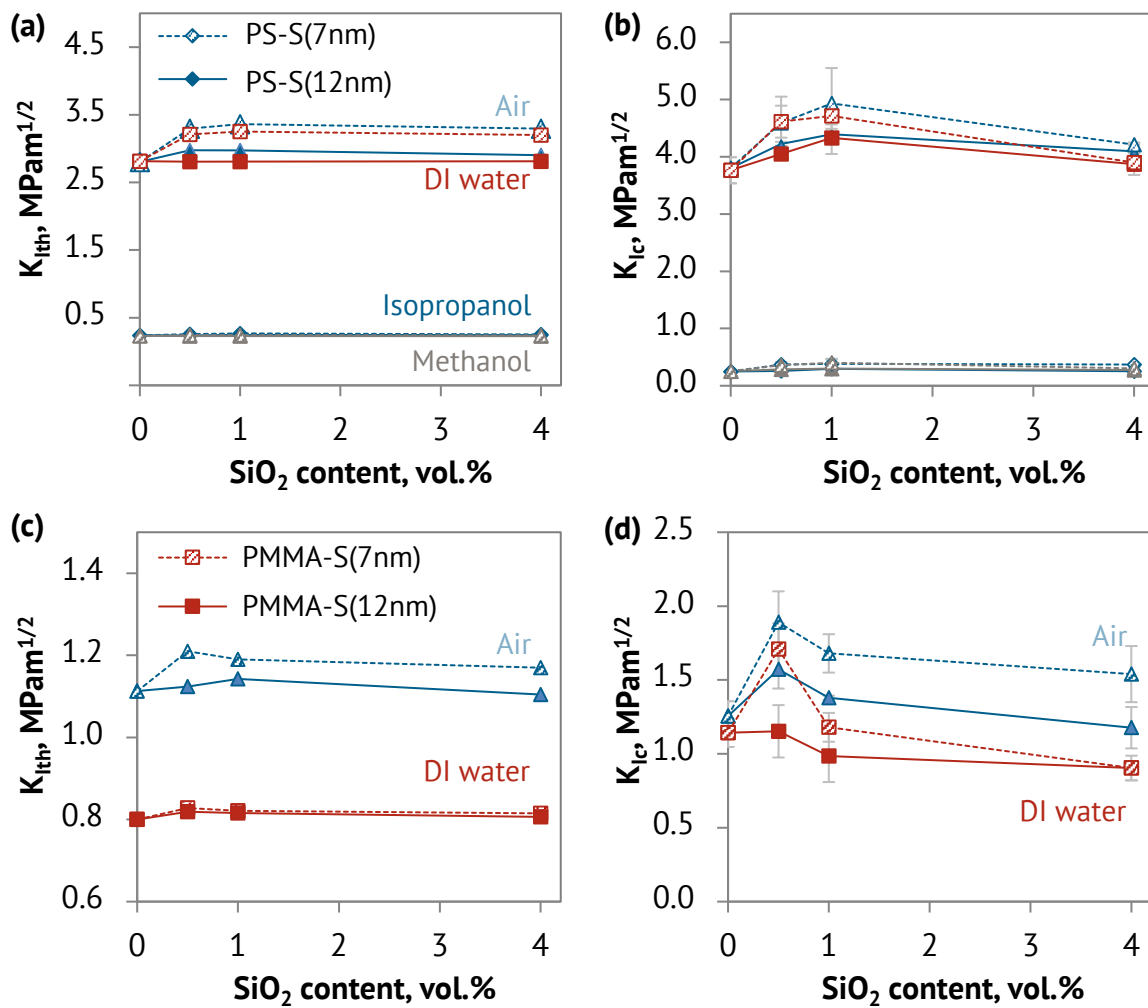
Figure 4.63: K_{Ith} and K_{Ic} of (a)-(b) PS and (c)-(d) PMMA as a function of nano-SiO_2 contents and size in different ESC agents.

(a)

(b)
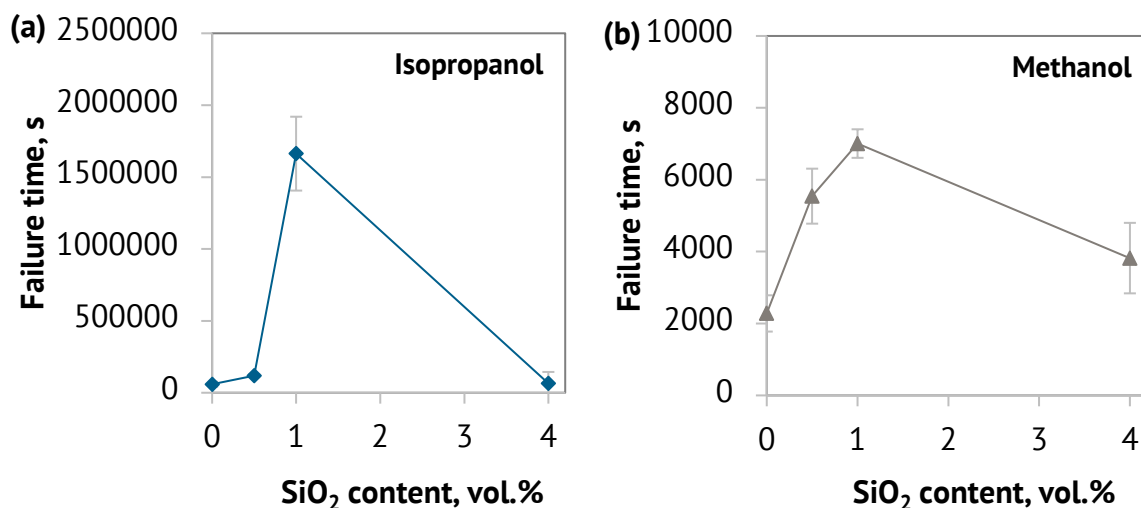
Figure 4.64: Failure time of PS nanocomposites in (a) isopropanol and (b) methanol.

4.2.4.2 Effect of Properties of ESC Agent

Considering the relationship between the ESC behavior of the materials in different liquid environments. Figures 4.65(a) and (b) show a plot of the K_{Ic} of PS and PMMA versus the solubility parameter of the stress cracking agents. As expected, the ESC resistance decreases as the solubility parameter of agent approach that of PS ($\sim$19 MPa$^{1/2}$). Alcohol agents reduce the K_{Ith} and K_{Ic} by a factor of 10 compared to DI water due to the more rapid absorption and higher chemical/structural compatibility of alcohol agent and PS. For PMMA nanocomposites, only the results in air and DI water were obtained in this study. Although Arnold [115] did report the effect of diffusion on environmental stress crack initiation in PMMA using slow strain rate tensile tests. It is observed that methanol and isopropanol, which have a closer solubility parameter relative to PMMA, act as severe ESC agents. An extreme plasticization and partial dissolution occur in the neat PMMA due to very specific combinations of chemical compatibility between these agents and PMMA. In contrast, DI water, which has a solubility parameter much higher than that of PMMA, exhibits a higher ESC resistance. This result confirms that the correlation of the mode I critical stress intensity factor with the Hansen solubility parameter shows very good agreement for different amorphous polymer-based nanocomposites. Therefore, this approach allows us to predict the risk of stress cracking in different fluids without performing extensive stress-cracking tests for the various application fields.
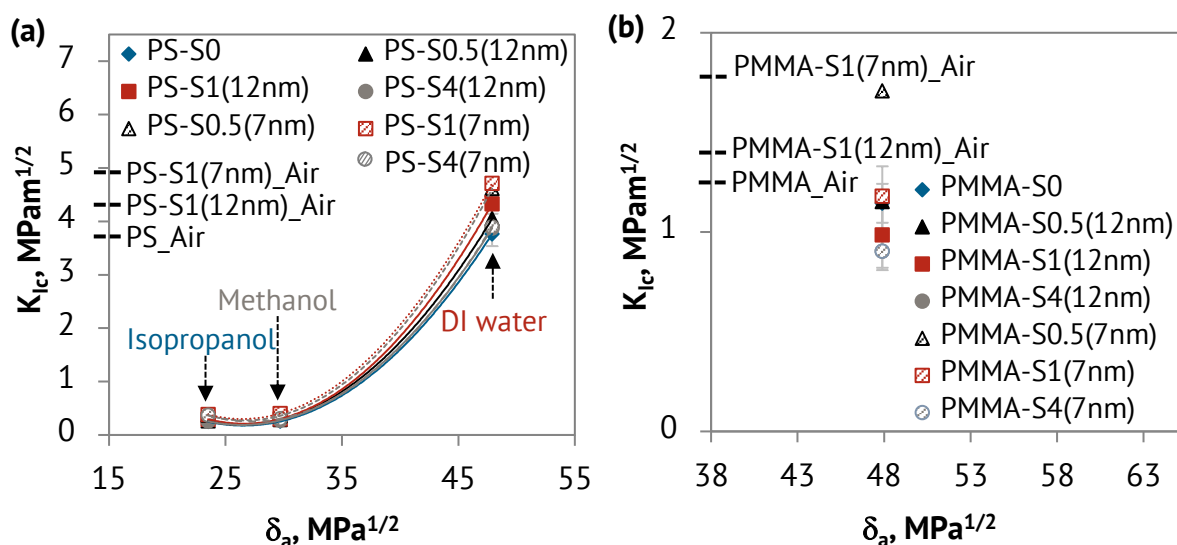
Figure 4.65: K_{Ic} of PS- and PMMA-based nanocomposites with different filler contents and sizes as a function of solubility parameter of ESC agents.

4.2.4.3 Comparison of ESC Properties for Different Amorphous Polymer Nanocomposites

Figure 4.66 illustrates the comparison of ESC resistance in term of the K_{Ic} value of the different nanocomposite materials in DI water. As expected, the dramatic differences in ESC resistance between the PC, PS, and PMMA-based nanocomposites can be clearly observed. PC has the highest ESC resistance, and PMMA is indeed observed to have the lowest ESC resistance. The greatest enhancement of ESC resistance in PC is attributed to the presence of multiple crazing deformations by triggering a kind of voluminous damaged zone that appears in front of the crack tip. This multiple crazing causes blunting at the crack tip and is responsible for the reduction of crack growth rate of PC. The similar behavior is also observed in PS nanocomposites, whereas this does not occur in PMMA nanocomposites. Thus, the ESC resistance of the materials improves in the following order: $PMMA/SiO_2 < PS/SiO_2 < PC/SiO_2$.

Additionally, a parallel correlation between the ESC resistance and absorption behavior of different materials in DI water is reasonable. As is demonstrated in Figure 4.66(b), PMMA absorbs the liquid molecules more readily than PS and PC-based nanocomposites, thus accelerating the crazing and cracking in the ESC process. This result also indicates that the sensitivity of amorphous polymers to ESC depends on their structure and chain flexibility, which is reflected by its glass transition temperature (T_g) (see Figure 4.66(c)). The PMMA, which has a lower T_g (~100 °C) than PS (~108 °C) and PC (~145 °C), has higher

chain flexibility, which can facilitate fluid permeation into the polymer. This promotes crazing, cracking or plasticization, which contributes to the lower ESC resistance. Generally, this effect is more pronounced as the service temperature approaches to the T_g values of the specific polymer.
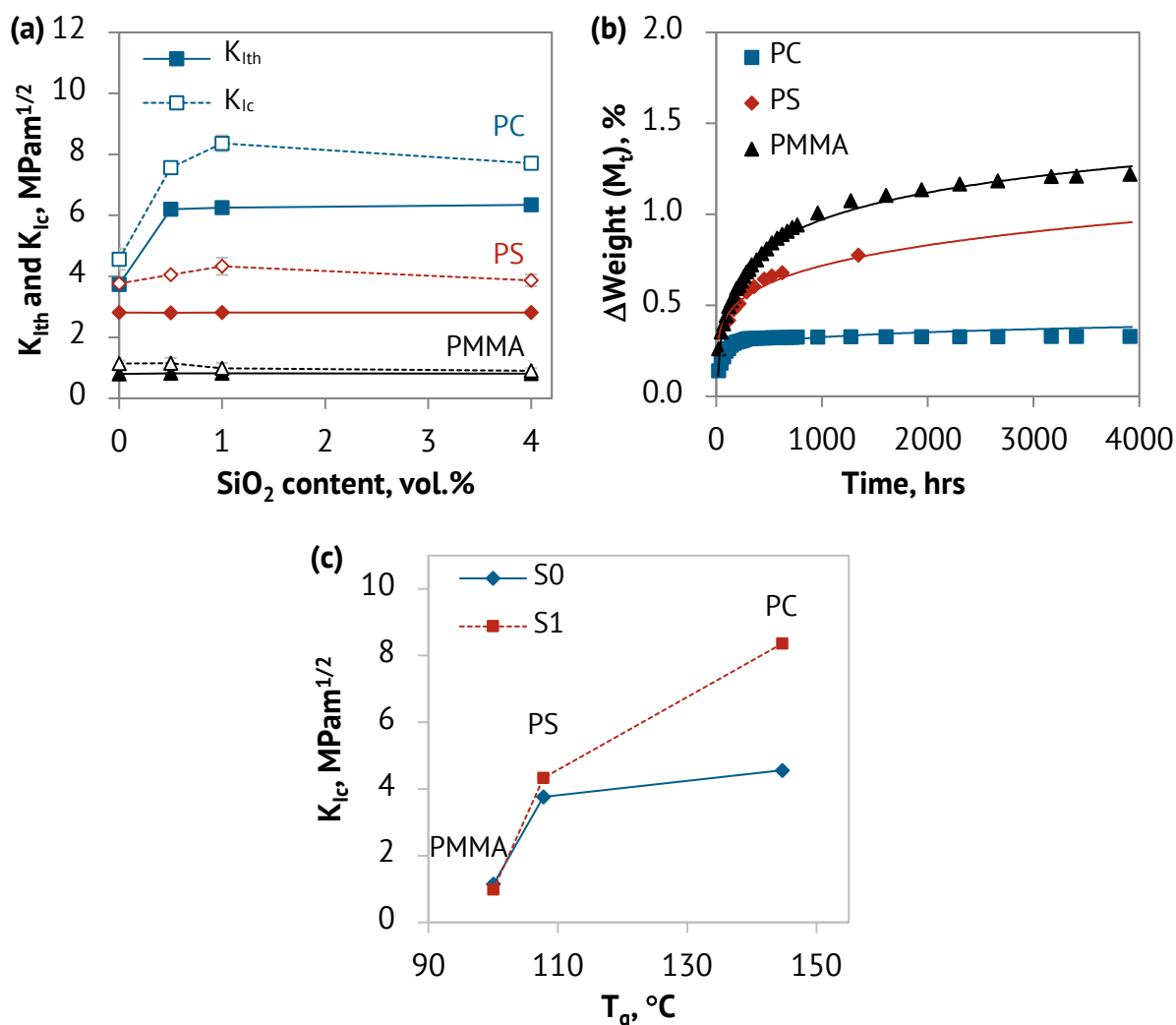
Figure 4.66: (a) K_{Ith}, K_{Ic}, and (b) absorption behavior of different materials in DI water and (c) relationship between the ESC resistance and the T_g of different specific polymers.

Morphological properties

The evidence of ESC mechanisms can be elucidated from the fractured surface appearance, as shown in Figure 4.67. Overall, the PC-based nanocomposites exhibit the greatest degree of ductility, follow by PS and PMMA as the least. The fractured surfaces of PC and PS typically show evidence of dissipative energy structures, such as localized microdeformation, cavitation, and particle debonding, which result in a larger energy absorption during the deformation process. However, there is an interesting difference

between the PMMA fractured surfaces, which shows a dimple structure induced by nano-particles (Figure 4.67(d)). Zhang [116] suggests that the formation of these dimples and sub-dimples of nanocomposites is also accompanied by a series of energy dissipative events, such as localized microdeformation of the matrix, particle debonding, and cavitations. These events might correspond to higher energy absorption during the formation and growth of the homogeneous crazes, resulting in a better ESC resistance of PMMA nanocomposites.
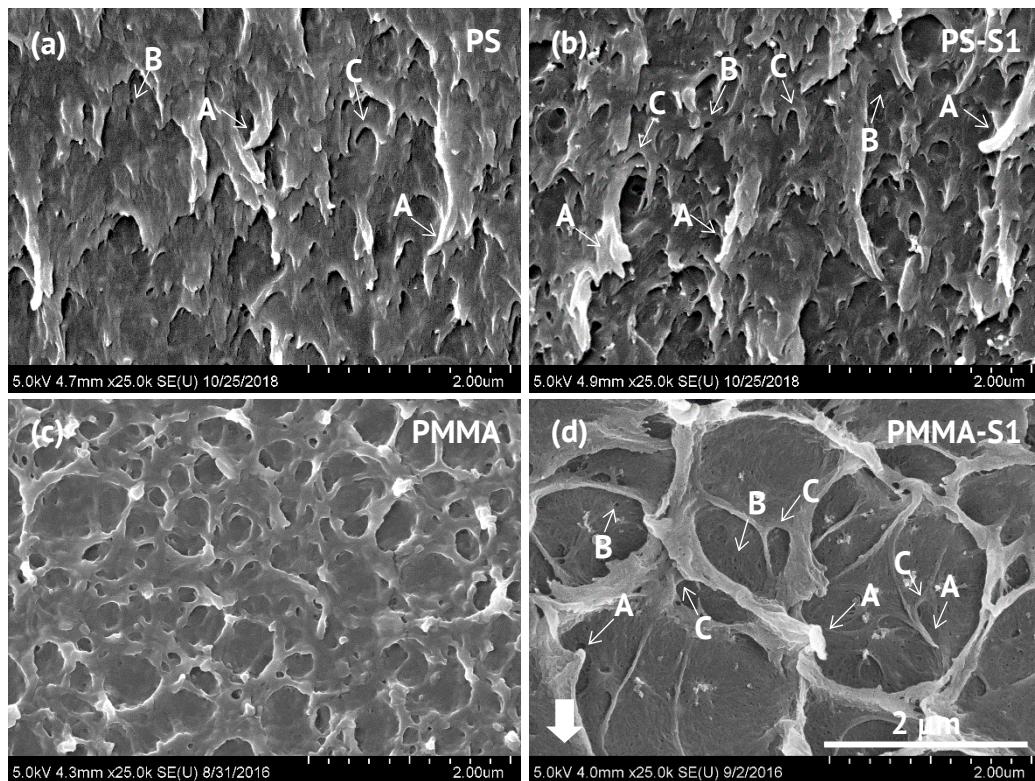
Figure 4.67: SEM images of failed CT-samples of (a) PS, (b) PS nanocomposites (1 vol.% nano-SiO_2), (c) PMMA and (d) PMMA nanocomposites (1 vol.% nano-SiO_2) in DI water. The white arrows indicate the direction of crack propagation. Features A, B, and C indicate plastic deformation, formation of cavities/nanoparticle debonding, and structures in parabolic shape, respectively.

5   Summary and Outlook

Summary

Amorphous polymer-based nanocomposites, which combine outstanding mechanical properties with exceptional transparency, constitute vital components for large-scale industrial applications. However, only a few studies have reported the behavior of reinforced polymers in terms of environmental stress cracking (ESC) resistance. Therefore, the present research work was focused not only on optical, mechanical, and thermal properties but also on the ESC behavior of amorphous-based polymers. Accordingly, the polymer nanocomposites of PC, PS, and PMMA filled with different nano-SiO_2 nanoparticle contents and sizes were prepared by melt compounding followed by injection molding.

The SEM micrographs revealed the good dispersion and uniform distribution of agglomerated nano-SiO_2 particles in the polymer matrix. Upon increasing the content of nanoparticles, slightly larger agglomerates formed. These agglomerated particles caused a reduction in material transparency due to light loss via reflection and scattering. Interestingly, the incorporation of nano-SiO_2 into the PC matrix greatly improved the tensile, impact, fracture toughness, and thermal properties of PC, which increased in conjunction with filler content (up to 4 vol.%), particularly in the case of smaller nano-SiO_2, which has a higher interfacial surface area, assuring a more effective energy dissipation at the interface. In the case of PS and PMMA nanocomposites, the highest improvements occurred with the incorporation of small amounts of smaller sized nano-SiO_2 (0.5 – 1 vol.%) and, then, tend to decrease. Based on optical, mechanical, and thermal properties, the best compromise was obtained in the PC-based nanocomposites. Thus, the effect of nanofiller on the ESC behavior was paid attention on PC-based nanocomposites.

The ESC resistance of PC exposed to different chemical agents (isopropanol, methanol, ethanol/DI water, and deionized water) was greatly enhanced by the presence of nano-SiO_2. This was particularly true in the case of small amounts and smaller sized nano-SiO_2, which significantly enhanced the ESC performance in all investigated fluids. A fractography analysis revealed dissipative energy structures in the PC nanocomposite matrices, which were responsible for improving the ESC resistance of the materials. The surface wettability and diffusion behavior of PC in different ESC agents promoted a better understanding of environmental effects on ESC failure. It was clearly indicated that the diffusion process in the polymer depended largely on the polymer structure, molecular size of the stress cracking agent and the degree of interaction between polymer and agent, which was related to the craze/crack formation in the ESC process of the polymer. ESC

resistance was reduced when the stress cracking agents had a lower molar volume and closer solubility parameters relative to those of the polymers, which accelerate the process of macroscopic brittle crack formation. In contrast, extraordinary improvements were displayed in mild agents where the solubility parameter of the agent differed significantly from the neat PC. Moreover, the enhancement of the ESC resistance can future achieve by using the high molecular weight PC due to the increased craze stability and fibril density during the ESC process. At a given nano-SiO_2 content, the ESC resistance of nanocomposites improved in the following order: PMMA/SiO_2 < PS/SiO_2 < PC-L/SiO_2 < PC-H/SiO_2. In most cases, nanocomposites with 1 vol.% nano-SiO_2 particles exhibit the highest improvement in ESC resistance. For nano-SiO_2 content more than 1 vol.%, the improvements are only marginal.

The correlation of the Mode I critical stress intensity factor with the Hansen solubility parameter and molar volume of agent shows a very good agreement for different fluids, thus allowing the determination of the stress cracking behavior of nanocomposites using only simple equations. An accelerated testing method has been developed for predicting slow crack growth behavior by applying a modified superposition approach. The good reproducibility and agreement of the construction of master curves suggested that the superposition approach could be used as a comparative method for predicting the crack growth behavior, especially for long-term ESC testing, as in mild agents. Both approaches can be useful tools for a quick prediction of ESC behavior, which allows minimizing the test time and the expense of stress-cracking tests for various applications.

Moreover, the modeling and simulation of diffusion processes linked to the structural fracture model are adequate to solve multifield problems of ESC failure. The simulated result agreed well with the results obtained from the experimental data. Thus, understanding liquid diffusion and fracture behavior by simulation became an important step for quick screening and mitigating the risk of ESC failures in plastic products.

Outlook

In the current study, fracture behavior is modeled based on linear-elastic fracture mechanics, which are suitable for brittle materials such as neat PC. However, in the case of PC nanocomposites, the remarkable improvement in toughness results in some challenges related to simulations. Due to the occurrence of large amounts of plastic deformation in tough materials, this effect cannot be ignored in the failure analysis. Accordingly, the plastically dissipated energy in the plastic zone around the crack tip should be taken into account in the simulations to ensure more accurate predictions of actual crack propagation behavior. Moreover, it is suggested to further developing the simulation

model to be able to presume the different crack types/shapes of the deformed area in front of the crack tip in different agents, which would make it possible to predict the ESC behavior in plastic products and potentially reduces the cost and time of introducing new materials in engineering applications.

6 References

[1]   Motaung, T.E.; Saladino, M.L.; Luyt, A.S.; Chillura Martino, D.F.: The effect of silica nanoparticles on the morphology, mechanical properties and thermal degradation kinetics of polycarbonate. Composites Science and Technology 73(1), 34–39, 2012.

[2]   Chau, J.L.H.; Hsu, S.L.C.; Chen, Y.M.; Yang, C.C.; Hsu, P.C.F.: A simple route towards polycarbonate-silica nanocomposite. Advanced Powder Technology 21(3), 341–343, 2010.

[3]   Müller, K.; Bugnicourt, E.; Latorre, M.; et al.: Review on the processing and properties of polymer nanocomposites and nanocoatings and their applications in the packaging, automotive and solar energy fields. Nanomaterials 7(4), 74, 2017.

[4]   Michler, G.H., Baltá-Calleja, F.J.: Nano- and micromechanics of polymers – structure modification and improvement of properties. Carl-Hanser Verlag, 2012.

[5]   Altstädt, V.: The influence of molecular variables on fatigue resistance in stress cracking environments. Advances in Polymer Science 188, 105–152, 2005.

[6]   Lin, L.; Schlarb, A.K.: A study on environmental stress cracking in nano-SiO_2-filled polycarbonate. Journal of Materials Science 47(18), 6614–6620, 2012.

[7]   Schlarb, A.K.: Determining Resistance to environmental stress cracking in luer fittings. Medical Device Technology, 2002.

[8]   Nomai, J.; Schlarb, A.K.: Environmental stress cracking (ESC) resistance of polycarbonate/SiO_2 nanocomposites in different media. Journal of Applied Polymer Science 134(43), 45451, 2017.

[9]   Pons, N.; Bergeret, A.; Benezet, J.C.; Ferry, L.; Fesquet, F.: An environmental stress cracking (ESC) test to study the ageing of biopolymers and biocomposites. Polymer Testing 30(3), 310–317, 2011.

[10]   Saharudin, M.S.; Wei, J.; Shyha, I.; Inam, F.: Environmental stress cracking resistance of halloysite nanoclay-polyester nanocomposites. World Journal of Engineering and Technology 05(03), 389–403, 2017.

[11]   Rull, N.; Ollier, R.P.; Francucci, G.; Rodriguez, E.S.; Alvarez, V.A.: Effect of the addition of nanoclays on the water absorption and mechanical properties of glass fiber/up resin composites. Journal of Composite Materials 49(13), 1629–1637, 2015. DOI: 10.1177/0021998314538869.

[12]   Bonnia, N.N.; Ahmad, S.H.; Surip, S.N.; Nurul, S.S.; Azlina, H.N.; Anuar, H.:

Mechanical properties and environmental stress cracking resistance of rubber toughened polyester/clay composite. Advanced Materials Research 576, 318–321, 2012.

[13]   Zhou, R.J.; Burkhart, T.: Influence of nanoparticle loading on craze formation and crack propagation of polycarbonate in different environments. Journal of Thermoplastic Composite Materials 23(5), 607–621, 2010.

[14]   Crosby, A.J.; Lee, J.Y.: Polymer nanocomposites: The "nano" effect on mechanical properties. Polymer Reviews 47(2), 217–229, 2007.

[15]   Paul, D.R.; Robeson, L.M.: Polymer nanotechnology: Nanocomposites. Polymer 49(15), 3187–3204, 2008.

[16]   Pradhan, S.; Lach, R.; Le, H.H.; Grellmann, W.; Radusch, H.-J.; Adhikari, R.: Effect of filler dimensionality on mechanical properties of nanofiller reinforced polyolefin elastomers. ISRN Polymer Science 2013, 1–9, 2013.

[17]   Zhou, T.H.; Ruan, W.H.; Yang, J.L.; Rong, M.Z.; Zhang, M.Q.; Zhang, Z.: A novel route for improving creep resistance of polymers using nanoparticles. Composites Science and Technology 67(11), 2297–2302, 2007.

[18]   Imai, Y.: Inorganic nano-fillers for polymers BT - Encyclopedia of polymeric nanomaterials. In Kobayashi, S.; Müllen, K. (eds): Springer Berlin Heidelberg, Berlin, Heidelberg, 2021.

[19]   Bhattacharya, M.: Polymer nanocomposites-A comparison between carbon nanotubes, graphene, and clay as nanofillers. Materials 9(4), 1–35, 2016.

[20]   Al-Harthi, M.A.; Bahuleyan, B.K.: Mechanical Properties of polyethylene-carbon nanotube composites synthesized by in situ polymerization using metallocene catalysts. Advances in Materials Science and Engineering 2018, 2018.

[21]   Trujillo, M.; Arnal, M.L.; Müller, A.J.; et al.: Thermal and morphological characterization of nanocomposites prepared by in-situ polymerization of high-density polyethylene on carbon nanotubes. Macromolecules 40(17), 6268–6276, 2007.

[22]   Kwon, S.-M.; Kim, H.-S.; Myung, SJ.; Jin, H.-J.: Poly(methyl methacrylate)/multiwalled carbon nanotube microspheres fabricated via in-situ dispersion polymerization. Journal of Polymer Science Part B: Polymer Physics 46(2), 182–189, 2008.

[23]   Chowdhury, S.R.; Chen, Y.; Wang, Y.; Mitra, S.: Microwave-induced rapid nanocomposite synthesis using dispersed single-wall carbon nanotubes as the nuclei. Journal of Materials Science 44(5), 1245–1250, 2009.

[24]   Zeng, C.; Lee, L.J.: Poly(methyl methacrylate) and polystyrene/clay nanocomposites prepared by in-situ polymerization. Macromolecules 34(12),

4098–4103, 2001.

[25]   Ma, X.; Zare, Y.; Rhee, K.Y.: A two-step methodology to study the influence of aggregation/agglomeration of nanoparticles on young's modulus of polymer nanocomposites. Nanoscale Research Letters 12, 0–6, Nanoscale Research Letters, 2017.

[26]   Lin, L.Y., Suksut, B., Schlarb, A.K.: Process-structure-property relationships in semicrystalline polymer-based nanocomposites. In Mittal, V. (ed): In: Manufacturing of Nanocomposites with Engineering Plastics, Cambridge, Sawston, 2015.

[27]   Coiai, S.; Passaglia, E.; Pucci, A.; Ruggeri, G.: Nanocomposites based on thermoplastic polymers and functional nanofiller for sensor applications. Materials 8(6), 3377–3427, 2015.

[28]   Greco, A.; Timo, A.; Maffezzoli, A.: Development and characterization of amorphous thermoplastic matrix graphene nanocomposites. Materials 5(10), 1972–1985, 2012.

[29]   Kalfus, J.; Jancar, J.: Reinforcing mechanisms in amorphous polymer nanocomposites. Composites Science and Technology 68(15–16), 3444–3447, 2008.

[30]   Yadav, R.; Naebe, M.; Wang, X.; Kandasubramanian, B.: Structural and thermal stability of polycarbonate decorated fumed silica nanocomposite via thermomechanical analysis and in-situ temperature assisted SAXS. Scientific Reports 7(1), 1–11, Springer US, 2017.

[31]   Stojanović, D.B.; Brajović, L.; Orlović, A.; et al.: Transparent PMMA/silica nanocomposites containing silica nanoparticles coating under supercritical conditions. Progress in Organic Coatings 76(4), 626–631, 2013.

[32]   Eungkee Lee, R.; Afsari Ghazi, A.; Azdast, T.; Hasanzadeh, R.; Mamaghani Shishavan, S.: Tensile and hardness properties of polycarbonate nanocomposites in the presence of styrene maleic anhydride as compatibilizer. Advances in Polymer Technology 37(6), 1737–1743, 2018.

[33]   Jing, H.; Higaki, Y.; Ma, W.; et al.: Preparation and characterization of polycarbonate nanocomposites based on surface-modified halloysite nanotubes. Polymer Journal 46(5), 307–312, 2014.

[34]   Vahabi, H.; Eterradossi, O.; Ferry, L.; Longuet, C.; Sonnier, R.; Lopez-Cuesta, J.M.: Polycarbonate nanocomposite with improved fire behavior, physical and psychophysical transparency. European Polymer Journal 49(2), 319–327, 2013.

[35]   Siengchin, S.; Karger-Kocsis, J.; Thomann, R.: Alumina-filled polystyrene micro- and nanocomposites prepared by melt mixing with and without latex precompounding: Structure and properties. Journal of Applied Polymer Science

105(5), 2963–2972, 2007.

[36]   Jang, J.Y.; Kim, M.S.; Jeong, H.M.; Shin, C.M.: Graphite oxide/poly(methyl methacrylate) nanocomposites prepared by a novel method utilizing macroazoinitiator. Composites Science and Technology 69(2), 186–191, 2009.

[37]   Brostow, W.; Dutta, M.; de Souza, J.R.; Rusek, P.; de Medeiros, A.M.; Ito, E.N.: Nanocomposites of poly(methyl methacrylate) (PMMA) and montmorillonite (MMT) Brazilian clay: A tribological study. Express Polymer Letters 4(9), 570–575, 2010.

[38]   Hasan, S.A. Ben; Dimitrijević, M.M.; Kojović, A.; et al.: The effect of the size and shape of alumina nanofillers on the mechanical behavior of PMMA matrix composites. Journal of the Serbian Chemical Society 79(10), 1295–1307, 2014.

[39]   Eslami, R.; Bagheri, R.; Hashemzadeh, Y.; Salehi, M.: Optical and mechanical properties of transparent acrylic based polyurethane nano Silica composite coatings. Progress in Organic Coatings 77(7), 1184–1190, Elsevier B.V., 2014.

[40]   Tanahashi, M.: Development of fabrication methods of filler/polymer nanocomposites: With focus on simple melt-compounding-based approach without surface modification of nanofillers. Materials 3(3), 1593–1619, 2010.

[41]   Luyt, A.S.; Messori, M.; Fabbri, P.; et al.: Polycarbonate reinforced with silica nanoparticles. Polymer Bulletin 66(7), 991–1004, 2011.

[42]   Zhou, R.J.; Burkhart, T.: Mechanical and optical properties of nanosilica-filled polycarbonate composites. Journal of Thermoplastic Composite Materials 23(4), 487–500, 2010.

[43]   Perez-Guerrero, A.; Lisperguer, J.; Orellana, F.: Influence of silica nanoparticles on the thermomechanical properties of recycled polystyrene. Journal of the Chilean Chemical Society 56(4), 907–910, 2011.

[44]   Bansal, A.; Yang, H.; Li, C.; et al.: Quantitative equivalence between polymer nanocomposites and thin polymer films. Nature Materials 4(9), 693–698, 2005.

[45]   Serenko, O.A.; Roldughin, V.I.; Askadskii, A.D.; Serkova, E.S.; Strashnov, P. V.; Shifrina, Z.B.: The effect of size and concentration of nanoparticles on the glass transition temperature of polymer nanocomposites. RSC Advances 7(79), 50113–50120, 2017.

[46]   Sanches, N. de B.; Dias, M.L.; Pacheco, E.B.A. V: Environmental stress cracking behavior of bottle and fiber grade poly(ethylene terephthalate) in contact with aqueous amine solutions. Polymer Engineering & Science 48(10), 1953–1962, 2008.

[47]   Wright, D.C.: Environmental Stress Cracking of Plastics. iSmithers Rapra

Publishing, 1996.

[48] Alperstein, D.; Knani, D.; Borchmann, N.; Spekowius, M.; Hopmann, C.: Prediction of environmental stress cracking in polycarbonate by molecular modeling. Polymers for Advanced Technologies 25(12), 1433–1438, 2014.

[49] Cheng, J.J.; Polak, M.A.; Penlidis, A.: Influence of micromolecular structure on environmental stress cracking resistance of high density polyethylene. Tunnelling and Underground Space Technology 26(4), 582–593, 2011.

[50] Hongxia, Z.; A., L.E.; A., J.S.: Effects of microcrystallinity and morphology on physical aging and its associated effects on tensile mechanical and environmental stress cracking properties of poly(ethylene terephthalate). Journal of Applied Polymer Science 112(5), 2906–2917.

[51] Ramsteiner F: Bewertung der Spannungsrissbeständigkeit. In: Grellmann W (ed) Prüfung von Verbundwerkstoffen. Carl Hanser, Munich, 2005.

[52] Han, X.; Hu, Y.; Tang, M.; Fang, H.; Wu, Q.; Wang, Z.: Preparation and characterization of long chain branched polycarbonates with significantly enhanced environmental stress cracking behavior through gamma radiation with addition of difunctional monomer. Polymer Chemistry 7(21), 3551–3561, 2016.

[53] Yeh, J.T.; Chen, J. -H; Hong, H. -S: Environmental stress cracking behavior of short-chain branch polyethylenes in Igepal solution under a constant load. Journal of Applied Polymer Science 54(13), 2171–2186, 1994.

[54] Nomai, J.; Schlarb, A.K.: Improving environmental stress cracking resistance of glassy polymers by the incorporation of nanofillers. In Young Researchers Symposium, Kaiserslautern, 2016.

[55] Chen, Y.; Lei, Y.; Zou, H.; Liang, M.; Cao, Y.: Structural and rheological property relationship of bimodal polyethylene with improved environment stress cracking resistance. Polymer Science Series A 56(5), 671–680, 2014.

[56] Cazenave, J.; B. Sixou; Seguela, R.: Structural approaches of polyethylene environmental stress-crack resistance. Oil & Gas Science and Technology – Rev. IFP 61(6), 735–742, 2006.

[57] Cheng, J.J.; Polak, M.A.; Penlidis, A.: Phase interconnectivity and environmental stress cracking resistance of polyethylene: A crystalline phase investigation. Journal of Macromolecular Science, Part A 46(6), 572–583, 2009.

[58] Miller-Chou, B.A.; Koenig, J.L.: A review of polymer dissolution. Progress in Polymer Science (Oxford) 28(8), 1223–1270, 2003.

[59] Karimi, M.: Diffusion in polymer solids and solutions. Mass Transfer in Chemical Engineering Processes 2011. DOI: 10.5772/23436.

[60]   Hansen, C.M.; Just, L.: Prediction of environmental stress cracking in plastics with Hansen solubility parameters. Industrial and Engineering Chemistry Research 40(1), 21–25, 2001.

[61]   Hansen C.M.: The three dimensional solubility parameter and solvent diffusion coefficient. Danish Technical Press, Copenhagen, 1967.

[62]   Hansen, C.M.: On predicting environmental stress cracking in polymers. Polymer Degradation and Stability 77(1), 43–53, 2002.

[63]   Kambour, R.P.; Gruner, C.L.; Romagosa, E.E.: Biphenol-A polycarbonate immersed in organic media. swelling and response to stress. Macromolecules 7(2), 248–253, 1974.

[64]   Riande, E.; Ricardo Diaz-Calleja, M.P.; Masegosa, R.; Salom, C.: Polymer viscoelasticity: stress and strain in practice. Marcel Dekker, Inc, New York, 1999.

[65]   Robeson, L.M.: Environmental stress cracking: A review. Polymer Engineering & Science 53(3), 453–467, 2013.

[66]   Kjellander, C.K.; Nielsen, T.B.; Ghanbari-Siahkali, A.; Kingshott, P.; Hansen, C.M.; Almdal, K.: ESC resistance of commercial grade polycarbonates during exposure to butter and related chemicals. Polymer Degradation and Stability 93(8), 1486–1495, 2008.

[67]   Lustiger, A.: Understanding Environmental stress cracking in polyethylene. In Medical Plastics: Degradation Resistance and Failure Analysis, Cambridge University Press, 2008.

[68]   Soni, P.L.; Geil, P.H.: Environmental stress cracking of polyethylene: Temperature effect. Journal of Applied Polymer Science 23(4), 1167–1179, 1979.

[69]   Alamri, H.; Low, I.M.: Effect of water absorption on the mechanical properties of nano-filler reinforced epoxy nanocomposites. Materials and Design 42, 214–222, 2012.

[70]   ASTM D 1693-01: Environmental stress-cracking of ethylene plastics, american society for testing of materials,. Phil., USA, 2001.

[71]   Saeda, S.; Suzaka, Y.: The environmental stress cracking of linear ethylene copolymers. Polymers for Advanced Technologies 6(9), 593–601, 1995.

[72]   INEOS Olefins & Polymers USA: Environmental stress crack resistance of polyethylene. 1–4, 2008.

[73]   Rachellowe: Bell telephone test (stress crack resistance). https://www.impact-solutions.co.uk/bell-telephone-test/, 2014, accessed 2.1.2019.

[74]   Nomai, J.; Schlarb, A.K.: Spannungsrissbeständigkeit effizient beurteilen.

Jahresmagazin Ingenieurwissenschaften/Kunststofftechnik 110–113.

[75] Andena, L.; Castellani, L.; Castiglioni, A.; Mendogni, A.; Rink, M.; Sacchetti, F.: Determination of environmental stress cracking resistance of polymers: Effects of loading history and testing configuration. Engineering Fracture Mechanics 101, 33–46, 2013.

[76] Kamaludin, M.A.; Patel, Y.; Blackman, B.R.K.; Williams, J.G.: Fracture mechanics testing for environmental stress cracking in thermoplastics. Procedia Structural Integrity 2, 227–234, 2016.

[77] Wikipedia: Fracture mechanics. https://en.wikipedia.org/wiki/Fracture_mechanics, accessed 1.1.2016.

[78] Seitz, J.T.; Balazs, C.F.: Application of time-temperature superposition principle to long term engineering properties of plastic materials. Polymer Engineering & Science 8(2), 151–160, 1968.

[79] Matsumoto, D.S.: Time-temperature superposition and physical aging in amorphous polymers. Polymer Engineering & Science 28(20), 1313–1317, 1988.

[80] Pedrazzoli, D.; Pegoretti, A.: Long-term creep behavior of polypropylene/fumed silica nanocomposites estimated by time-temperature and time-strain superposition approaches. Polymer Bulletin 71(9), 2247–2268, 2014.

[81] Tajvidi, M.; Falk, R.H.; Hermanson, J.C.: Time-temperature superposition principle applied to a kenaf-fiber/high- density polyethylene composite. Journal of Applied Polymer Science 97(5), 1995–2004, 2005.

[82] Gupta, M.; Deshpande, A.P.: Time-temperature superposition. https://slideplayer.com/slide/10038177/, accessed 5.1.2019.

[83] Zhou, R.-J.; Burkhart, T.: Optical properties of particle-filled polycarbonate, polystyrene, and poly(methyl methacrylate) composites. Journal of Applied Polymer Science 115(3), 1866–1872, 2009.

[84] Girifalco, L.A.; Good, R.J.: A theory for the estimation of surface and interfacial energies. I. Derivation and application to interfacial tension. Journal of Physical Chemistry 61(7), 904–909, 1957.

[85] Carvalho, S.P.; Lucas, E.F.; González, G.; Spinelli, L.S.: Determining hildebrand solubility parameter by ultraviolet spectroscopy and microcalorimetry. Journal of the Brazilian Chemical Society 24(12), 1998–2007, 2013.

[86] Bouaziz, A.; Jaziri, M.; Dalmas, F.; Massardier, V.: Nanocomposites of silica reinforced polypropylene: Correlation between morphology and properties. Polymer Engineering & Science 54(9), 2187–2196, 2013.

[87] Bhawal, P.; Das, T.K.; Ganguly, S.: Fabrication of light weight mechanically robust

short carbon fiber / ethylene methyl acrylate polymeric nanocomposite for effective electromagnetic interference shielding. Journal of Polymer Science & Applications 1–13, 2017.

[88]   Marini, J. and Bretas, R.E.S.: Optical properties of blown films of PA6/MMT nanocomposites. Materials Research 1, 2017. DOI: 10.1590/1980-5373-MR-2017-0280.

[89]   Li, S.; Meng Lin, M.; Toprak, M.S.; Kim, D.K.; Muhammed, M.: Nanocomposites of polymer and inorganic nanoparticles for optical and magnetic applications. Nano Reviews 1(1), 5214, 2010.

[90]   Kierkels, J.: Tailoring the mechanical properties of amorphous polymers., 2006. DOI: 10.6100/IR613293.

[91]   Lin, L.; Schlarb, A.K.: Investigation on morphology and properties of melt compounded polyoxymethylene/carbon nanotube composites. Journal of Applied Polymer Science 132(40), 1–9, 2015.

[92]   Jeon, I.Y.; Baek, J.B.: Nanocomposites derived from polymers and inorganic nanoparticles. Materials 3(6), 3654–3674, 2010.

[93]   Schindler, H.J.; J. Morf: On estimation of fracture toughness from instrumented and standard chrapy V-notched tests. In: Proceedings of the 10th Congress on Material Testing, Budapest, Hungary 2, 172–177, 1991.

[94]   W. Grellmann: Deformation and fracture behaviour of polymers. Springer-Heidelberg, 2001.

[95]   Vogiatzis, G.G.; Theodorou, D.N.: multiscale molecular simulations of polymer-matrix nanocomposites: or what molecular simulations have taught us about the fascinating nanoworld. Springer Netherlands, 2017.

[96]   Peng, R.; Li, D.: Fabrication of nanochannels on polystyrene surface. Biomicrofluidics 9(2), 1–14, 2015.

[97]   Choudalakis, G.; Gotsis, A.D.: Free volume and mass transport in polymer nanocomposites. Current Opinion in Colloid and Interface Science 17(3), 132–140, 2012.

[98]   Zhu, A.; Cai, A.; Zhang, J.; Jia, H.; Wang, J.: PMMA-grafted-silica/PVC nanocomposites: Mechanical performance and barrier properties. Journal of Applied Polymer Science 108(4), 2189–2196, 2008.

[99]   Matteucci, S.; Kusuma, V.A.; Swinnea, S.; Freeman, B.D.: Gas permeability, solubility and diffusivity in 1,2-polybutadiene containing brookite nanoparticles. Polymer 49(3), 757–773, 2008.

[100]   Nielsen, T.B.; Hansen, C.M.: Surface wetting and the prediction of environmental

stress cracking (ESC) in polymers. Polymer Degradation and Stability 89(3), 513–516, 2005.

[101] Saharudin, M.S.; Atif, R.; Shyha, I.; Inam, F.: The degradation of mechanical properties in polymer nano-composites exposed to liquid media - A review. RSC Advances 6(2), 1076–1089, Royal Society of Chemistry, 2016.

[102] Ashraf, M.A.; Peng, W.; Zare, Y.; Rhee, K.Y.: Effects of size and aggregation/agglomeration of nanoparticles on the interfacial/interphase properties and tensile strength of polymer nanocomposites. Nanoscale Research Letters 13, 2018. DOI: 10.1186/s11671-018-2624-0.

[103] Chudnovsky, A.; Moet, A.: On the law of fatigue crack layer propagation in polymers. Polymer Engineering & Science 22(15), 922–927, 1982.

[104] Sehanobish, K.; Baer, E.; Chudnovsky, A.; Moet, A.: Crack propagation in polystyrene under fixed elongation. Journal of Materials Science 20(6), 1934–1944, 1985.

[105] Quaresimin, M.; Salviato, M.; Zappalorto, M.: A multi-scale and multi-mechanism approach for the fracture toughness assessment of polymer nanocomposites. Composites Science and Technology 91, 16–21, 2014.

[106] Arencón, D.; Velasco, J.I.: Fracture toughness of polypropylene-based particulate composites. Materials 2(4), 2046–2094, 2009.

[107] Huang, M.; Thompson, V.P.; Rekow, E.D.; Soboyejo, W.O.: Modeling of water absorption induced cracks in resin-based composite supported ceramic layer structures. Journal of Biomedical Materials Research Part B: Applied Biomaterials 84B(1), 124–130, 2008.

[108] H. Baaser: Ageing of polymer materials—testing, modelling and simulation considering diffusion. In W. Grellmann; B. Langer (eds): Deformation and fracture behaviour of polymer materials, Springer Nature, 2017.

[109] Crank, J.; Park, G.S.: Diffusion in polymer. Academic Press, USA, 1968.

[110] Crank, J.: The mathematics of diffusion. Claredon Press, England, 1975.

[111] Lin, Y.C.: Investigation of the moisture-desorption characteristics of epoxy resin. Journal of Polymer Research 13(5), 369–374, 2006.

[112] Ming-Zhu, P.; Chang-Tong, M.; Xu-Bing, Z.; Yun-Lei, P.: Effects of rice straw fiber morphology and content on the mechanical and thermal properties of rice straw fiber-high density polyethylene composites. Journal of Applied Polymer Science 121(5), 2900–2907, 2011.

[113] Li, W.: Effect of silica nanoparticles on the morphology of polymer blends. Technische Universiteit Eindhoven, 2011. DOI: 10.6100/IR719366.

[114]   Doyle, M.J.; Maranci, A.; Orowan, E.; Stork, S.T.: The fracture of glassy polymers. Proceedings of the Royal Society of London. Series A, Mathematical and Physical Sciences. 329(1577), 137–151, 1972.

[115]   Arnold, J.C.: The effects of diffusion on environmental stress crack initiation in PMMA. Journal of Materials Science 33(21), 5193–5204, 1998.

[116]   Zhang, H.; Zhang, Z.; Yang, J.; Friedrich, K.: Temperature dependence of crack initiation fracture toughness of various nanoparticles filled polyamide 66. 47, 679–689, 2006.

List of Publications

Publication in Peer-Reviewed Journals:

1. Nomai, J.; Schlarb, A.K.: Effects of nanoparticle size and concentration on optical, toughness, and thermal properties of polycarbonate. Journal of Applied Polymer Science 136 (2019), DOI: 10.1002/APP.47634.
2. Nomai, J.; Schlarb, A.K.: Environmental stress cracking (ESC) resistance of polycarbonate/SiO_2 nanocomposites in different media. Journal of Applied Polymer Science 134 (2017), DOI: 10.1002/APP.45451.
3. Nomai, J.; Suksut, B.; Schlarb, A.K.: Crystallization behavior of poly(lactic acid)/titanium dioxide nanocomposites, KMUTNB: International Journal of Applied Science and Technology, 8 (2015), pp. 251-258, dx.doi.org/10.14416/j.ijast.2015.10.003.

Conference Distribution/Other Publications:

1. Nomai, J.; Schlarb, A.K.: Efficient analysis and determination of environmental stress cracking of polymers in different environment. Polymer Testing & Analysis, Pittsburgh, USA, 11-12 September 2018.
2. Nomai, J.; Schlarb, A.K.: Enhancement of environmental stress cracking resistance of luer-connectors. Beutel, Schläuche, Folien in der Medizintechnik, Heidelberg, Germany, 26-27 April 2017.
3. Nomai, J.; Schlarb, A.K.: Spannungsrissbeständigkeit effizient beurteilen. Jahresmagazin Ingenieurwissenschaften/Kunststofftechnik 10 (2016), pp. 110-113.
4. Nomai, J.; Schlarb, A.K.: Challenges for polymer nanocomposites in modern medical applications. Young Polymer Scientist Forum 2016, Aachen, Germany, 6 July 2016.
5. Nomai, J.; Schlarb, A.K.: Improving environmental stress cracking resistance of glassy polymers by the incorporation of nanofillers. Young Researchers Symposium 2016, Kaiserslautern, Germany, 14-15 April 2016.

Directed Thesis

1. Yao, H.: The influence of nano-SiO$_2$ on the environmental stress cracking (ESC) resistance of polystyrene (PS). Bachelor thesis 2019.

2. Quintus, R.: A study on environmental stress cracking in nano-SiO$_2$-filled polystyrene (PS). Bachelor thesis 2019.

3. Mannnherz, D.: Environmental stress cracking (ESC) behaviors of polystyrene (PS)/SiO$_2$ nanocomposites. Student project 2018.

4. Shi, S.: A study on environmental stress cracking in nano-SiO$_2$-filled polycarbonate (PC). Bachelor thesis 2017.

5. Txopitea, Ioritz.: Improving the environmental stress cracking resistance of poly(methyl methacrylate) (PMMA) by the incorporation of nanofillers. Master thesis 2016.

6. Coyen, Y.: Konstruktion, Aufbau und Inbetriebnahme einer Versuchseinrichtung zur On-line-Charakterisierung des Spannungsrissverhaltens von Biegeproben aus polymeren Nanokompositen. Student project 2015.

Appendix

A   Optical properties of PC, PS and PMMA nanocomposites

Designation	With particle size of 7nm			With particle size of 12nm		
	Transmittance	Clarity	Haze	Transmittance	Clarity	Haze
	%			%		
PC-L-S0	90.8	3.82	95.4	90.8	3.82	95.4
PC-L-S0.5	76.2	12.5	95.6	71.3	30.0	91.1
PC-L-S1	66.1	24.0	95.5	61.5	51.1	90.1
PC-L-S2	52.7	51.5	95.4	47.7	80.9	87.6
PC-L-S4	43.8	78.4	95.0	29.8	97.1	80.0
PC-H-S0	73.7	4.93	95.2	73.7	4.93	95.2
PC-H-S0.5	45.6	27.3	95.3	46.9	38.6	90.7
PC-H-S1	36.2	42.4	95.3	36.8	58.5	89.1
PC-H-S2	25.2	67.0	94.9	25.1	82.8	85.6
PC-H-S4	19.2	81.4	94.7	16.2	97.1	78.7
PS-S0	89.0	8.69	97.8	89.0	8.69	97.8
PS-S0.5	80.1	20.3	96.5	80.0	26.2	95.6
PS-S1	72.9	33.2	95.3	74.1	41.1	92.7
PS-S2	64.6	49.1	92.8	60.7	67.4	88.9
PS-S4	54.8	68.6	89.1	52.9	87.4	75.8
PMMA-S0	93.8	4.90	97.2	93.8	4.9	97.2
PMMA-S0.5	91.9	5.70	97.2	88.3	22.2	95.9
PMMA-S1	90.7	9.34	97.9	86.4	28.7	95.4
PMMA-S2	87.6	10.1	97.6	82.7	43.1	93.8
PMMA-S4	84.3	9.49	97.4	73.5	67.8	90.5

B   Mechanical properties of PC, PS and PMMA nanocomposites filled with SiO_2 (7 nm)

Designation	Tensile properties			Toughness properties	
	Young's modulus	Tensile strength	Elongation at break	Notched impact strength	Fracture toughness
	MPa		%	kJ/m^2	MPam$^{1/2}$
PC-L-S0	2315±96	63.37±1.48	28.20±11.95	13.14±0.78	3.43±0.10
PC-L-S0.5	2475±51	71.39±1.59	65.13±11.84	20.46±2.05	5.29±0.12
PC-L-S1	2486±61	71.26±1.48	63.13±16.44	21.90±4.26	5.74±0.05
PC-L-S4	2650±85	72.57±1.94	48.98±15.66	34.25±3.99	5.92±0.22
PC-H-S0	2311±79	67.89±2.18	49.90±24.83	15.62±0.39	5.00±0.23
PC-H-S0.5	2383±127	71.13±3.37	61.41±13.77	47.53±9.37	6.03±0.11
PC-H-S1	2450±86	71.18±1.18	71.66±5.60	49.05±5.43	6.08±0.11
PC-H-S4	2604±115	69.29±1.53	57.37±17.24	53.99±10.35	6.35±0.07
PS-S0	2035±87	45.18±0.35	23.47±8.75	5.15±1.03	3.47±0.06
PS-S0.5	2115±49	50.54±0.84	9.49±1.85	5.26±0.29	3.65±0.04
PS-S1	2161±80	51.24±1.89	9.81±3.12	5.41±0.51	3.72±0.06
PS-S4	2371±43	52.15±1.17	6.10±2.02	2.92±0.19	3.64±0.08
PMMA-S0	3258±71	65.77±1.34	5.06±1.53	1.04±0.21	1.11±0.04
PMMA-S0.5	3609±128	69.43±2.60	3.06±0.21	1.18±0.31	1.22±0.14
PMMA-S1	3643±59	70.35±3.57	3.23±0.36	1.29±0.36	0.98±0.09
PMMA-S4	3865±56	60.10±4.33	2.20±0.25	0.86±0.59	0.87±0.08

C Mechanical properties of PC, PS and PMMA nanocomposites filled with SiO_2 (12 nm)

Designation	Tensile properties			Toughness properties	
	Young's modulus	Tensile strength	Elongation at break	Notched impact strength	Fracture toughness
	MPa		%	kJ/m^2	MPam$^{1/2}$
PC-L-S0	2315±96	63.37±1.48	28.20±11.95	13.14±0.78	3.43±0.10
PC-L-S0.5	2388±59	64.84±0.89	35.76±14.11	3.50±0.96	4.97±0.21
PC-L-S1	2385±38	64.77±1.05	44.94±21.64	7.24±4.63	5.41±0.06
PC-L-S2	2471±145	65.48±0.84	50.09±21.83	12.17±9.38	5.60±0.00
PC-L-S3	2553±66	66.90±0.78	52.62±13.32	13.81±8.04	5.68±0.07
PC-L-S4	2565±55	66.42±0.91	56.23±13.96	29.86±7.60	5.67±0.09
PC-H-S0	2311±79	67.89±0.90	49.90±24.83	15.62±0.39	5.00±0.23
PC-H-S0.5	2416±79	67.37±0.91	57.24±12.65	17.62±5.40	5.53±0.10
PC-H-S1	2441±58	68.47±3.15	55.27±27.00	24.55±5.08	5.67±0.06
PC-H-S2	2473±42	66.67±0.53	64.29±7.75	42.84±4.21	5.75±0.08
PC-H-S3	2557±31	67.12±0.31	56.54±7.88	47.56±4.90	5.78±0.08
PC-H-S4	2623±77	66.93±1.00	41.65±11.63	40.97±4.48	5.79±0.16
PS-S0	2035±87	45.18±0.35	23.47±8.75	5.14±1.10	3.47±0.06
PS-S0.5	2131±72	45.73±0.66	11.21±4.80	4.73±0.53	3.51±0.05
PS-S1	2199±194	46.35±0.30	11.65±6.93	4.90±0.23	3.56±0.03
PS-S2	2280±107	47.00±0.36	12.65±5.69	3.93±0.54	3.55±0.07
PS-S3	2367±89	46.39±0.35	13.01±4.44	3.10±0.23	3.50±0.14
PS-S4	2414±127	46.66±0.38	12.46±6.16	1.95±0.28	3.31±0.06
PMMA-S0	3258±71	65.77±1.34	5.06±1.53	1.01±0.20	1.11±0.04
PMMA-S0.5	3420±58	67.96±1.48	3.76±0.39	0.95±0.23	1.15±0.04
PMMA-S1	3409±79	68.35±1.26	3.81±0.30	0.66±0.16	0.94±0.03
PMMA-S2	3461±81	66.59±1.60	3.51±0.36	0.63±0.24	0.88±0.03
PMMA-S3	3563±83	63.40±2.72	3.10±0.32	0.58±0.12	0.79±0.05
PMMA-S4	3675±78	60.32±3.98	2.46±0.26	0.51±0.04	0.78±0.05

D   Thermal properties of PC, PS and PMMA nanocomposites

Designation	With particle size of 7nm	With particle size of 12nm
	Glass transition temperature	Glass transition temperature
	°C	°C
PC-L-S0	145.32±0.38	145.32±0.38
PC-L-S0.5	145.95±0.80	146.11±0.25
PC-L-S1	146.20±0.54	146.36±0.19
PC-L-S2	146.69±0.05	146.69±0.36
PC-L-S4	147.22±0.17	147.51±0.21
PC-H-S0	144.71±0.41	144.71±0.41
PC-H-S0.5	144.98±0.18	145.76±0.33
PC-H-S1	145.69±0.26	146.30±0.48
PC-H-S2	146.63±0.62	147.01±0.56
PC-H-S4	148.09±0.11	147.88±0.06
PS-S0	107.76±2.39	107.76±2.39
PS-S0.5	109.63±0.60	109.83±0.27
PS-S1	109.64±0.98	110.02±0.20
PS-S2	109.85±0.53	110.19±0.57
PS-S4	110.30±0.65	110.51±0.57
PMMA-S0	100.06±0.62	100.06±0.62
PMMA-S0.5	100.48±0.48	100.66±0.55
PMMA-S1	100.21±0.49	100.38±0.58
PMMA-S2	100.37±0.58	100.71±0.51
PMMA-S4	101.32±0.85	101.57±0.23

E Contact angle (θ) and interfacial tension at the liquid-solid interface (γ_{sl}) of PC, PS and PMMA nanocomposites filled with SiO_2 (7 nm) in different ESC agents

Designation	DI water		Isopropanol		Methanol	
	θ	γ_{sl}	θ	γ_{sl}	θ	γ_{sl}
	degree	µN/m	degree	µN/m	degree	µN/m
PC-L-S0	81.9±5.6	23.7	17.4±4.2	1.55	12.2±4.1	4.16
PC-L-S0.5	80.0±0.8	23.3	15.4±4.1	1.56	8.6±1.0	4.21
PC-L-S1	79.5±0.8	23.2	13.9±4.7	1.57	8.0±1.0	4.22
PC-L-S4	77.8±0.9	22.9	14.0±3.7	1.57	4.4±0.9	4.24
PC-H-S0	83.7±3.0	24.1	27.3±3.7	1.50	14.6±2.4	4.13
PC-H-S0.5	84.5±1.9	24.3	23.4±2.4	1.52	14.4±4.2	4.13
PC-H-S1	81.1±0.9	23.5	20.4±8.6	1.53	14.2±3.1	4.13
PC-H-S4	78.5±2.1	23.0	19.9±1.2	1.54	12.4±1.7	4.16
PS-S0	65.7±2.8	24.7	20.3±3.2	2.04	17.4±2.8	4.98
PS-S0.5	65.5±5.0	24.7	16.6±3.1	2.07	13.9±3.1	5.06
PS-S1	58.7±5.9	25.5	15.0±1.5	2.09	12.9±3.3	5.08
PS-S4	58.9±2.7	25.5	13.8±1.6	2.10	9.9±2.9	5.13
PMMA-S0	65.4±4.4	11.2	14.0±1.2	0.017	9.7±3.5	0.660
PMMA-S0.5	65.4±1.7	11.2	12.2±2.9	0.015	8.2±2.5	0.663
PMMA-S1	62.8±1.2	10.7	9.9±3.0	0.014	7.7±2.3	0.663
PMMA-S4	62.5±1.3	10.6	7.4±1.2	0.013	5.8±0.6	0.666

F   Contact angle (θ) and interfacial tension at the liquid-solid interface (γ_{sl}) of PC, PS and PMMA nanocomposites filled with SiO_2 (12 nm) in different ESC agents

Designation	ESC agent					
	DI water		Isopropanol		Methanol	
	θ	γ_{sl}	θ	γ_{sl}	θ	γ_{sl}
	degree	$\mu N/m$	degree	$\mu N/m$	degree	$\mu N/m$
PC-L-S0	81.9±5.6	23.7	17.4±4.2	1.55	12.2±4.1	4.16
PC-L-S0.5	81.9±0.9	23.7	16.8±3.6	1.55	9.9±3.9	4.19
PC-L-S1	80.2±2.0	23.3	15.9±4.0	1.56	9.5±4.3	4.20
PC-L-S4	78.0±1.2	22.9	14.5±2.1	1.57	8.8±1.2	4.21
PC-H-S0	86.7±2.9	24.9	29.4±1.5	1.50	15.6±1.9	4.11
PC-H-S0.5	87.5±1.1	25.2	25.4±1.6	1.51	14.7±3.7	4.12
PC-H-S1	84.0±1.7	24.2	21.8±2.5	1.52	14.4±3.3	4.13
PC-H-S4	81.0±0.8	23.5	20.8±3.9	1.53	12.5±1.7	4.16
PS-S0	65.7±2.8	24.7	20.3±3.2	2.04	17.4±2.8	4.98
PS-S0.5	66.0±1.0	24.6	17.2±1.5	2.07	14.5±5.4	5.05
PS-S1	60.6±5.3	25.2	16.0±3.9	2.08	13.9±3.3	5.06
PS-S4	58.1±4.2	25.6	14.5±3.4	2.09	10.5±4.0	5.12
PMMA-S0	65.4±4.4	11.2	14.0±1.2	0.017	9.7±3.5	0.660
PMMA-S0.5	64.6±0.4	11.0	13.0±1.5	0.016	10.1±1.5	0.660
PMMA-S1	64.7±3.7	11.1	10.7±2.4	0.014	7.9±3.7	0.663
PMMA-S4	65.3±6.6	11.2	8.2±2.0	0.013	7.7±1.9	0.663

G   ESC properties of PC-H nanocomposites at room temperature in different ESC agents

Agent	Designation	With particle size of 7nm		With particle size of 12nm	
		K_{Ith}	K_{Ic}	K_{Ith}	K_{Ic}
		$MPam^{1/2}$		$MPam^{1/2}$	
Isopropanol	PC-H-S0	3.59	5.13±0.22	3.59	5.13±0.22
	PC-H-S0.5	3.71	6.08±0.02	3.62	5.69±0.12
	PC-H-S1	3.78	6.39±0.18	3.62	5.72±0.19
	PC-H-S4	3.65	6.34±0.09	3.63	5.61±0.19
Methanol	PC-H-S0	3.24	4.24±0.11	3.24	4.24±0.11
	PC-H-S0.5	3.41	5.03±0.25	3.27	4.90±0.22
	PC-H-S1	3.42	5.32±0.13	3.36	5.17±0.41
	PC-H-S4	3.39	5.16±0.17	3.35	4.65±0.18
Ethanol solution	PC-H-S0	3.49	4.32±0.05	3.49	4.32±0.05
	PC-H-S0.5	4.42	5.92±0.24	4.39	5.42±0.34
	PC-H-S1	4.51	6.06±0.13	4.41	5.84±0.47
	PC-H-S4	4.52	6.00±0.29	4.38	5.78±0.25
Urea solution	PC-H-S0	–	–	3.66	4.39±0.18
	PC-H-S0.5	–	–	4.80	6.81±0.66
	PC-H-S1	–	–	5.91	7.25±0.61
	PC-H-S4	–	–	5.82	6.65±0.26
DI water	PC-H-S0	3.74	4.56±0.35	3.74	4.56±0.35
	PC-H-S0.5	6.41	9.25±0.34	6.20	7.57±0.18
	PC-H-S1	6.50	10.16±0.29	6.26	8.36±0.26
	PC-H-S4	6.76	8.93±0.16	6.34	7.70±0.16
Air	PC-H-S0	5.77	7.12±0.21	5.77	7.12±0.21
	PC-H-S0.5	6.70	8.84±0.38	6.50	8.68±0.47
	PC-H-S1	6.92	9.95±0.12	6.55	8.76±0.02
	PC-H-S4	6.82	8.47±0.29	6.66	8.06±0.45

H ESC properties of PC-L nanocomposites at room temperature in different ESC agents

Agent	Designation	With particle size of 7nm		With particle size of 12nm	
		K_{Ith}	K_{Ic}	K_{Ith}	K_{Ic}
		MPam$^{1/2}$		MPam$^{1/2}$	
Isopropanol	PC-L-S0	3.30	4.19±0.05	3.30	4.19±0.05
	PC-L-S0.5	3.33	4.78±0.17	3.29	4.46±0.15
	PC-L-S1	3.36	4.95±0.11	3.35	4.60±0.08
	PC-L-S4	3.36	4.75±0.28	3.31	4.58±0.15
Methanol	PC-L-S0	2.38	2.49±0.01	2.38	2.49±0.01
	PC-L-S0.5	2.45	2.59±0.04	2.41	2.51±0.03
	PC-L-S1	2.46	2.68±0.12	2.43	2.52±0.03
	PC-L-S4	2.44	2.55±0.02	2.39	2.49±0.02
Ethanol solution	PC-L-S0	2.55	2.67±0.08	2.55	2.67±0.08
	PC-L-S0.5	3.63	3.88±0.02	3.35	3.45±0.01
	PC-L-S1	3.71	3.93±0.05	3.68	3.87±0.02
	PC-L-S4	3.65	3.93±0.08	3.68	3.80±0.02
DI water	PC-L-S0	3.03	3.19±0.04	3.03	3.19±0.04
	PC-L-S0.5	3.69	4.31±0.27	3.64	3.87±0.12
	PC-L-S1	6.14	7.67±0.57	5.40	7.00±0.45
	PC-L-S4	5.95	7.63±0.35	5.42	7.47±0.36
Air	PC-L-S0	4.90	5.25±0.21	4.90	5.25±0.21
	PC-L-S0.5	5.40	6.48±0.23	5.37	6.33±0.23
	PC-L-S1	6.31	8.26±0.32	5.61	7.64±0.35
	PC-L-S4	6.02	7.77±0.40	5.57	7.59±0.42

I ESC properties of PC-H nanocomposites filled with SiO_2 (12 nm) at elevated temperature in different ESC agents

Agent	Designation	Temperature					
		28°C		38°C		48°C	
		K_{Ith}	K_{Ic}	K_{Ith}	K_{Ic}	K_{Ith}	K_{Ic}
		$MPam^{1/2}$		$MPam^{1/2}$		$MPam^{1/2}$	
Isopropanol	PC-H-S0	3.58	5.04±0.01	3.57	4.74±0.10	3.57	4.61±0.08
	PC-H-S0.5	3.62	5.44±0.11	3.61	5.12±0.11	3.60	4.88±0.09
	PC-H-S1	3.64	5.51±0.18	3.62	5.19±0.12	3.61	4.94±0.13
	PC-H-S4	3.60	5.38±0.16	3.59	5.03±0.10	3.58	4.83±0.12
Methanol	PC-H-S0	3.23	4.09±0.07	3.23	3.73±0.08	3.23	3.44±0.10
	PC-H-S0.5	3.26	4.50±0.21	3.25	4.00±0.19	3.25	3.75±0.15
	PC-H-S1	3.36	4.82±0.13	3.35	4.43±0.13	3.35	3.98±0.12
	PC-H-S4	3.34	4.27±0.18	3.34	3.86±0.12	3.34	3.61±0.12
Ethanol solution	PC-H-S0	3.36	4.29±0.20	3.30	4.20±0.11	3.39	4.05±0.29
	PC-H-S0.5	4.38	5.25±0.22	4.30	5.05±0.21	4.26	4.76±0.19
	PC-H-S1	4.40	5.70±0.39	4.32	5.41±0.06	4.28	5.21±0.18
	PC-H-S4	4.36	5.46±0.29	4.30	5.17±0.15	4.25	5.00±0.23
DI water	PC-H-S0	3.53	4.35±0.12	3.21	3.96±0.11	3.31	3.72±0.15
	PC-H-S0.5	6.00	7.44±0.19	5.89	7.24±0.16	5.63	7.03±0.16
	PC-H-S1	6.01	7.82±0.12	5.93	7.54±0.13	5.71	7.34±0.19
	PC-H-S4	6.04	7.54±0.23	5.91	7.36±0.21	5.69	7.11±0.19

J   ESC properties of PC-L nanocomposites filled with SiO_2 (12 nm) at elevated temperature in different ESC agents

Agent	Designation	Temperature					
		28°C		38°C		48°C	
		K_{Ith}	K_{Ic}	K_{Ith}	K_{Ic}	K_{Ith}	K_{Ic}
		$MPam^{1/2}$		$MPam^{1/2}$		$MPam^{1/2}$	
Isopropanol	PC-L-S0	3.29	4.01±0.16	3.28	3.80±0.11	3.27	3.64±0.17
	PC-L-S0.5	3.29	4.35±0.12	3.29	4.15±0.16	3.28	3.94±0.15
	PC-L-S1	3.35	4.47±0.21	3.35	4.21±0.14	3.34	4.02±0.20
	PC-L-S4	3.30	4.40±0.18	3.29	4.19±0.10	3.29	3.97±0.22
Methanol	PC-L-S0	2.21	2.32±0.02	1.84	1.96±0.02	1.49	1.60±0.02
	PC-L-S0.5	2.26	2.36±0.02	2.04	2.14±0.02	1.77	1.88±0.01
	PC-L-S1	2.30	2.38±0.02	2.07	2.16±0.03	1.81	1.90±0.02
	PC-L-S4	2.25	2.35±0.01	2.05	2.15±0.04	1.78	1.88±0.02
Ethanol solution	PC-L-S0	2.49	2.61±0.03	2.43	2.54±0.04	2.31	2.43±0.04
	PC-L-S0.5	3.25	3.35±0.04	3.15	3.24±0.04	3.04	3.14±0.04
	PC-L-S1	3.62	3.78±0.02	3.51	3.68±0.03	3.35	3.51±0.04
	PC-L-S4	3.59	3.71±0.04	3.45	3.57±0.06	3.29	3.42±0.05
DI water	PC-L-S0	2.89	3.02±0.05	2.72	2.86±0.06	2.49	2.66±0.11
	PC-L-S0.5	3.51	3.75±0.08	3.42	3.65±0.05	3.22	3.48±0.05
	PC-L-S1	5.21	6.75±0.12	5.01	6.12±0.14	4.80	5.35±0.15
	PC-L-S4	5.26	7.12±0.68	5.10	6.57±0.40	4.87	5.59±0.29

K ESC properties of PS nanocomposites at room temperature in different ESC agents

Agent	Designation	With particle size of 7nm		With particle size of 12nm	
		K_{Ith}	K_{Ic}	K_{Ith}	K_{Ic}
		MPam$^{1/2}$		MPam$^{1/2}$	
Isopropanol	PS-S0	0.24	0.25±0.00	0.24	0.25±0.0
	PS-S0.5	0.26	0.37±0.05	0.24	0.26±0.01
	PS-S1	0.27	0.38±0.07	0.25	0.30±0.06
	PS-S4	0.25	0.37±0.02	0.24	0.26±0.02
Methanol	PS-S0	0.23	0.25±0.00	0.23	0.25±0.00
	PS-S0.5	0.24	0.36±0.05	0.23	0.29±0.05
	PS-S1	0.24	0.40±0.07	0.23	0.30±0.01
	PS-S4	0.24	0.30±0.01	0.23	0.27±0.01
DI water	PS-S0	2.81	3.76±0.23	2.81	3.76±0.23
	PS-S0.5	3.21	4.61±0.28	2.81	4.05±0.23
	PS-S1	3.25	4.71±0.15	2.81	4.33±0.28
	PS-S4	3.20	3.90±0.25	2.81	3.87±0.19
Air	PS-S0	2.83	3.79±0.04	2.83	3.79±0.04
	PS-S0.5	3.30	4.59±0.46	2.91	4.25±0.03
	PS-S1	3.36	4.93±0.62	3.04	4.40±0.07
	PS-S4	3.29	4.21±0.37	2.92	4.20±0.05

L ESC properties of PMMA nanocomposites at room temperature in different ESC agents

Agent	Designation	With particle size of 7nm		With particle size of 12nm	
		K_{Ith}	K_{Ic}	K_{Ith}	K_{Ic}
		MPam$^{1/2}$		MPam$^{1/2}$	
DI water	PMMA-S0	0.80	1.14±0.10	0.80	1.14±0.10
	PMMA-S0.5	0.83	1.71±0.18	0.82	1.15±0.18
	PMMA-S1	0.82	1.18±0.10	0.82	0.99±0.18
	PMMA-S4	0.82	0.90±0.08	0.81	0.90±0.08
Air	PMMA-S0	1.11	1.26±0.10	1.11	1.26±0.10
	PMMA-S0.5	1.21	1.89±0.21	1.12	1.57±0.13
	PMMA-S1	1.19	1.68±0.13	1.14	1.38±0.01
	PMMA-S4	1.17	1.54±0.19	1.10	1.18±0.14

Curriculum Vitae

Personal Data

Family Name: Nomai
Name: Jiraporn
Nationality: Thai
Date/Place of Birth: January 19, 1989/Nakhon Ratchasima, Thailand

Education

2001 – 2007   Sura Nari Witthaya School, Nakhon Ratchasima, Thailand

Academic Studies

2007 – 2011   Bachelor of Engineering (B.Eng.), Polymer Engineering, Suranaree University of Technology, Nakhon Ratchasima, Thailand (First Class Honors)

2011 – 2013   Master of Engineering (M.Eng.), Polymer Engineering, Suranaree University of Technology, Nakhon Ratchasima, Thailand

2014 – 2016   PhD student, Material Science at the Chair of Composite Engineering, Technische Universität Kaiserslautern, Kaiserslautern, Germany

Professional Experience

2016 – Present   Scientific research assistant at the Chair of Composite Engineering, Technische Universität Kaiserslautern, Kaiserslautern, Germany

Promotion

2019   Title: On the Effect of Nanofillers on the Environmental Stress Cracking Resistance of Glassy Polymers